

LEVEL II

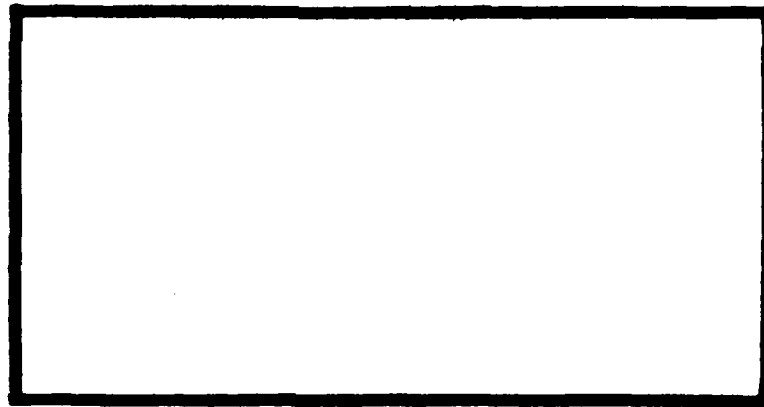


AD A111099



SECRET
FEB 13 1982
E

DUPLICATE COPY



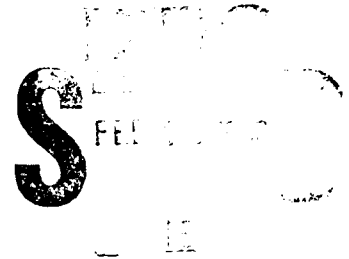
DEPARTMENT OF THE AIR FORCE
AIR UNIVERSITY (ATC)
AIR FORCE INSTITUTE OF TECHNOLOGY

Wright-Patterson Air Force Base, Ohio

This document has been approved
for public release and sale; its
distribution is unlimited.

82 02 18 052

AFIT/GAE/AA/81D-25



A COMPUTERIZED DATA ACQUISITION
INTERFACE TO MEASURE TURBULENT
SHEAR FLOW VELOCITY PROFILES
BEHIND A GRID OF PARALLEL RODS

THESIS

AFIT/GAE/AA/81D-25 S.A. Robinson Jr.
Capt. USAF

Approved for public release; distribution unlimited.

AFIT/GAE/AA/81D-25

A COMPUTERIZED DATA ACQUISITION INTERFACE TO
MEASURE TURBULENT SHEAR FLOW VELOCITY
PROFILES BEHIND A GRID OF PARALLEL RODS

THESIS

Presented to the Faculty of the School of Engineering
of the Air Force Institute of Technology

Air Training Command

in Partial Fulfillment of the
Requirements for the Degree of
Master of Science

Accession For	
NTIS GRA&I	<input checked="" type="checkbox"/>
DTIC TAB	<input type="checkbox"/>
Unannounced	<input type="checkbox"/>
Justification	
By _____	
Distribution/	
Availability Codes	
Dist	Avail. and/or Spec.
A	

by

Samuel A. Robinson Jr., B. Eng., M.B.A.

Captain USAF

Graduate Aeronautical Engineering

December 1981

Approved for public release; distribution unlimited.

Acknowledgements

I owe a strong debt of gratitude to Professor Harold E. Wright, my thesis advisor, for patiently supporting me throughout this project. His encouraging, affable mien guided me in bringing this project to fruition.

To Dr. K. S. Nagaraja of the Air Force Flight Dynamics Laboratory, which sponsored this project, and his fellow workers there, I express to them my appreciation for their assistance in this project.

There are people who made the mechanics of this project work; I now want to remember them for the help that they gave me in this effort: Messrs. William W. Baker and H. Leroy Cannon for their assistance in the laboratory; Messrs. Carl Shortt, Russ Murry, and John Brokas (all of the Air Force Institute of Technology (AFIT) shop) for their support in fabricating several project components; and Mr. Greg Tibbs of the Air Force Aero-Propulsion Laboratory for his contribution in breadboarding the project circuitry.

Using the data acquisition system was a new experience; and much of my learning to use the system grew from the cooperation and encouragement of three fellow AFIT officers: Major John Vonada, Captain Michael J. Kirchner, and Captain David L. Neyland. To them I wish to express my thanks.

To my typist (sin qua non a thesis would not exist), Miss Laura Wainwright, my sincere appreciation.

Contents

	<u>Page</u>
Acknowledgements	iii
List of Acronyms and Symbols	v
List of Figures	vi
List of Tables	x
Abstract	xi
I. Introduction	1
Background	1
Problem and Scope	5
Approach and Presentation	5
II. Equipment Description	7
Apparatus	7
Instrumentation	11
Automatic Data Acquisition System	14
III. The Stepper Motor	17
Description	18
Stepper Motor Control	18
Mechanical Design	22
IV. The Interface	24
Interface Card	24
Interface Box Circuitry	25
Software	27
V. Results and Discussion	32
Measurement Technique	32
Performance of the System	35
Test Runs	36
Evaluation	67
VI. Conclusions and Recommendations	76
Bibliography	79
Appendix A: Stepper Motor Manufacturer's Data	82
Appendix B: Probe Calibration	89
Appendix C: Raw Data	97
Vita	111

List of Acronyms and Symbols

a_i	Constant of Proportionality (volts/(ft./sec.))
ADAS	Automatic Data Acquisition System
AFIT	Air Force Institute of Technology
e	Root-Mean-Square Voltage (volts)
E	Average Voltage (volts)
H	Tunnel Height (= 9 inches)
U	Streamwise Velocity (ft./sec.)
U_{mean}, \bar{U}	Mean Streamwise Velocity (ft./sec.)
U_{max}	Maximum Streamwise Velocity (ft./sec.)
u'	Streamwise Fluctuating Velocity (ft./sec.)
$\frac{u'}{\bar{U}_{\text{mean}}}$	Turbulence Intensity
X	Streamwise Direction (inches)
Y	Vertical Transverse Direction (inches)

List of Figures

<u>Figure</u>	<u>Page</u>
1. One-seventh Power Law Velocity Profile	3
2. One-fourth Power Law Velocity Profile	4
3. AFIT Low Speed Wind Tunnel	8
4. Test Cabin Flowfield	9
5. Grid Templates and Rods	10
6. Grid Installation	11
7. Hot Wire Instrumentation	13
8. Hot Wire Instrumentation Block Diagram	13
9. Sensor and Sensor Attachments	14
10. Automatic Data Acquisition System	15
11. Automatic Data Acquisition System Block Diagram	16
12. Stepper Motor Schematic	19
13. Stepper Motor Control System	21
14. Traversing Mechanism	22
15. Interface Card	25
16. Standard Interface	26
17. Interface Cable	27
18. Unipolar Drive Circuit	28
19. Bipolar Drive Circuit	29
20. Bipolar Drive Circuit (continued)	30
21. Velocity Profile, Grid A1, X = 4 inches	38
22. Velocity Profile, Grid A1, X = 14 inches	39
23. Velocity Profile, Grid A1, X = 29 inches	40
24. Nondimensional Velocity Profile, No Grid, X/H = .44	41

List of Figures (continued)

<u>Figure</u>	<u>Page</u>
25. Nondimensional Velocity Profile, No Grid, X/H = 1.56	42
26. Nondimensional Velocity Profile, No Grid, X/H = 3.22	43
27. Turbulence Intensity Profile, No Grid, X/H = .44	44
28. Turbulence Intensity Profile, No Grid, X/H = 1.56	45
29. Turbulence Intensity Profile, No Grid, X/H = 3.22	46
30. Nondimensional Velocity Profile, Grid A1, X/H = .44	48
31. Nondimensional Velocity Profile, Grid A1, X/H = 1.56	49
32. Nondimensional Velocity Profile, Grid A1, X/H = 3.22	50
33. Turbulence Intensity Profile, Grid A1, X/H = .44	51
34. Turbulence Intensity Profile, Grid A1, X/H = 1.56	52
35. Turbulence Intensity Profile, Grid A1, X/H = 3.22	53
36. Nondimensional Velocity Profile, Grid A3, X/H = .44	54
37. Nondimensional Velocity Profile, Grid A3, X/H = 1.56	55
38. Nondimensional Velocity Profile, Grid A3, X/H = 3.22	56
39. Turbulence Intensity Profile, Grid A3, X/H = .44	57
40. Turbulence Intensity Profile, Grid A3, X/H = 1.56	58

List of Figures (continued)

<u>Figure</u>	<u>Page</u>
41. Turbulence Intensity Profile, Grid A3, X/H = 3.22	59
42. Nondimensional Velocity Profile, Grid B1, X/H = .44	61
43. Nondimensional Velocity Profile, Grid B1, X/H = 1.56	62
44. Nondimensional Velocity Profile, Grid B1, X/H = 3.22	63
45. Turbulence Intensity Profile, Grid B1, X/H = .44	64
46. Turbulence Intensity Profile, Grid B1, X/H = 1.56	65
47. Turbulence Intensity Profile, Grid B1, X/H = 3.22	66
48. Nondimensional Velocity Profile, Cylinder, X/H = .44	68
49. Nondimensional Velocity Profile, Cylinder, X/H = 1.56	69
50. Nondimensional Velocity Profile, Cylinder, X/H = 3.22	70
51. Turbulence Intensity Profile, Cylinder, X/H = .44	71
52. Turbulence Intensity Profile, Cylinder X/H = 1.56	72
53. Turbulence Intensity Profile, Cylinder, X/H = 3.22	73
54. Stepper Motor Description	83
55. Stepper Motor Description (continued)	84
56. Stepper Motor Description	85
57. Stepper Motor Driver Description (continued)	86
58. Stepper Motor Driver Description (continued)	87

List of Figures (continued)

<u>Figure</u>	<u>Page</u>
59. Stepper Motor Driver Description (continued)	88
60. Fourth Order Calibration Curve	93
61. Third Order Calibration Curve	94
62. "Best Fit" King's Law Calibration Curve	95
63. Velocity Profile, No Grid, X = 4 inches	98
64. Velocity Profile, No Grid, X = 14 inches	99
65. Velocity Profile, No Grid, X = 29 inches	100
66. Velocity Profile, Grid A3, X = 4 inches	101
67. Velocity Profile, Grid A3, X = 14 inches	102
68. Velocity Profile, Grid A3, X = 29 inches	103
69. Velocity Profile, Grid B1, X = 4 inches	104
70. Velocity Profile, Grid B1, X = 14 inches	105
71. Velocity Profile, Grid B1, X = 29 inches	106
72. Velocity Profile, Cylinder, X = 4 inches	107
73. Velocity Profile, Cylinder, X = 14 inches	108
74. Velocity Profile, Cylinder, X = 29 inches	109

List of Tables

<u>Table</u>		<u>Page</u>
I	Hot Wire Calibration Data	96
II	Maximum Run Velocities	110

Abstract

A design study was conducted to develop a computerized, electromechanical data acquisition system interface to instrumentation/apparatus measuring turbulent shear flow velocity profiles behind a grid of parallel rods. Data on profiles generated behind two such grids was acquired via a digital controller and a user-built interface to the data acquisition system. Conclusions were drawn that the digital controller did provide a superior means in collecting/reducing data than existed before, that the interface did provide an enhanced capability in documenting fluid flow phenomena under such test conditions, and that the experience did indicate future work in automating instrumentation/apparatus electromechanical components.

A COMPUTERIZED DATA ACQUISITION INTERFACE
TO MEASURE TURBULENT SHEAR FLOW VELOCITY
PROFILES BEHIND A GRID OF PARALLEL RODS

I. Introduction

Microcomputer data acquisition systems will soon become standard in most laboratory environments -- due in large part to the inherent flexibility and inexpensive cost of these systems. Providing distinct advantages over conventional means of data acquisition, these systems will allow more complete documentation in areas of scientific inquiry.

To investigate one such area of interest -- the turbulent boundary layer formed by a wake type flow field -- the Air Force Institute of Technology (AFIT), under the auspices of the Aero-Propulsion Laboratory and the Air Force Office of Scientific Research, acquired a Hewlett-Packard (HP) 3052A Automatic Data Acquisition System (ADAS). The existence of this ADAS allowed a follow-up to a recommendation of McKnight (ref. 15): in generating turbulent shear flow velocity profiles behind a grid of parallel rods, data acquisition and processing should "be automated in order to make possible the collection of larger amounts of data in a given period of time" and to enhance the data processing.

Background

McKnight's concerns were in evaluating the effect of grid geometry in creating these profiles. To investigate the effect of grid geometry, McKnight constructed several grids which

created the velocity profiles that he sought by varying rod spacing in the grid. One profile was that of a one-seventh power law distribution, illustrated in Figure 1; and another was that of a one-fourth power law distribution, illustrated in Figure 2.

According to Cockrell and Lee (ref. 5), "the production of required velocity profiles in a duct or wind tunnel is a necessary part of much research aimed at understanding fluid behavior. Perhaps the most obvious application is the simulation of wind gradients for the study of wind effects on structures, but equally important is the study of diffuser and duct behaviour when subjected to a variety of known and convenient velocity profiles. Furthermore, the effects of the variation in turbulent characteristics within a range of identical velocity profiles produced by different methods are not clearly understood."

One way to get a better understanding of such a variation in turbulence characteristics is to obtain more data. With proper interfacing, an ADAS gets the researcher more data -- facilitating study of the effects of the variation in turbulence characteristics within a range of identical velocity profiles produced by different grid generation schemes (what McKnight did manually).

Using McKnight's work then as the basis, selected experimental methods used in his research became candidates for automation through interfacing with the ADAS. These candidates included the low speed wind tunnel controls, the hot wire anemometer system, and auxiliary electromechanical components.

VELOCITY PROFILE

1/7th Power Law

$$(Y/H)^{1/7} = U/U_{max}$$

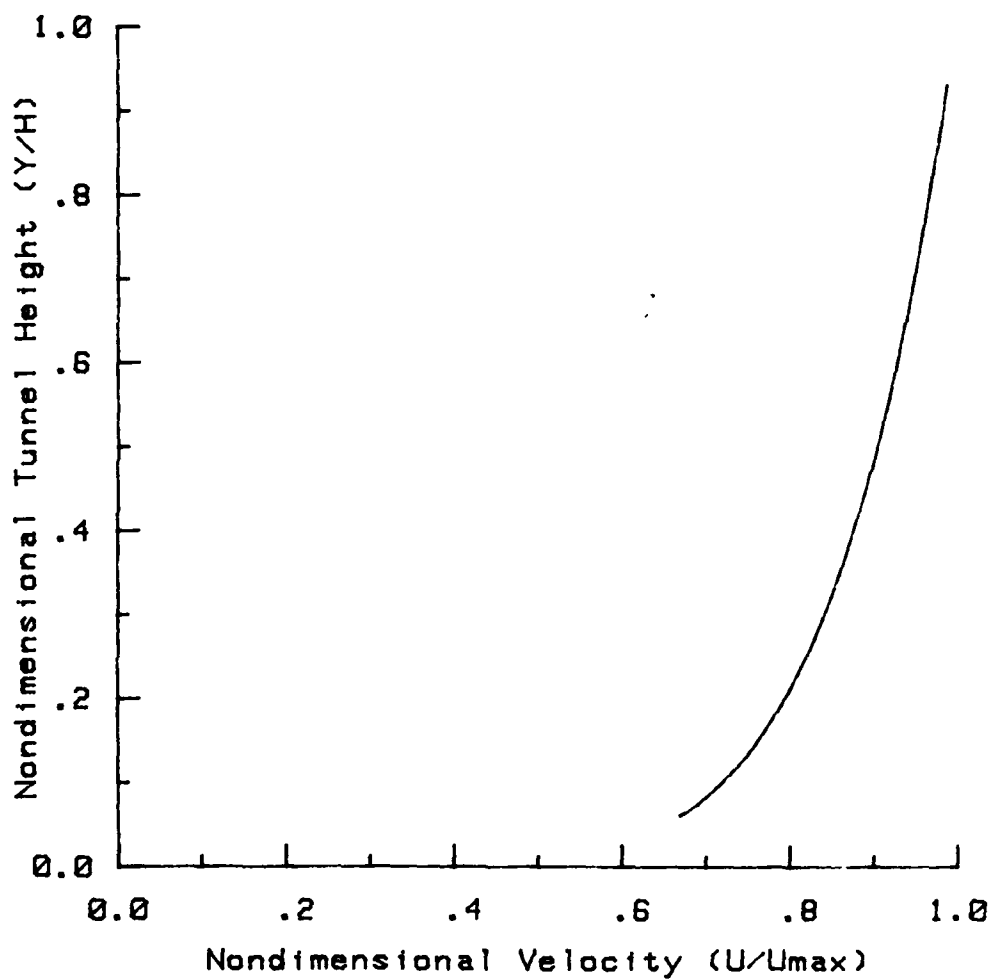


Figure 1. One-seventh Power Law Velocity Profile

VELOCITY PROFILE

1/4th Power Law

$$(Y/H)^{1/4} = U/U_{max}$$

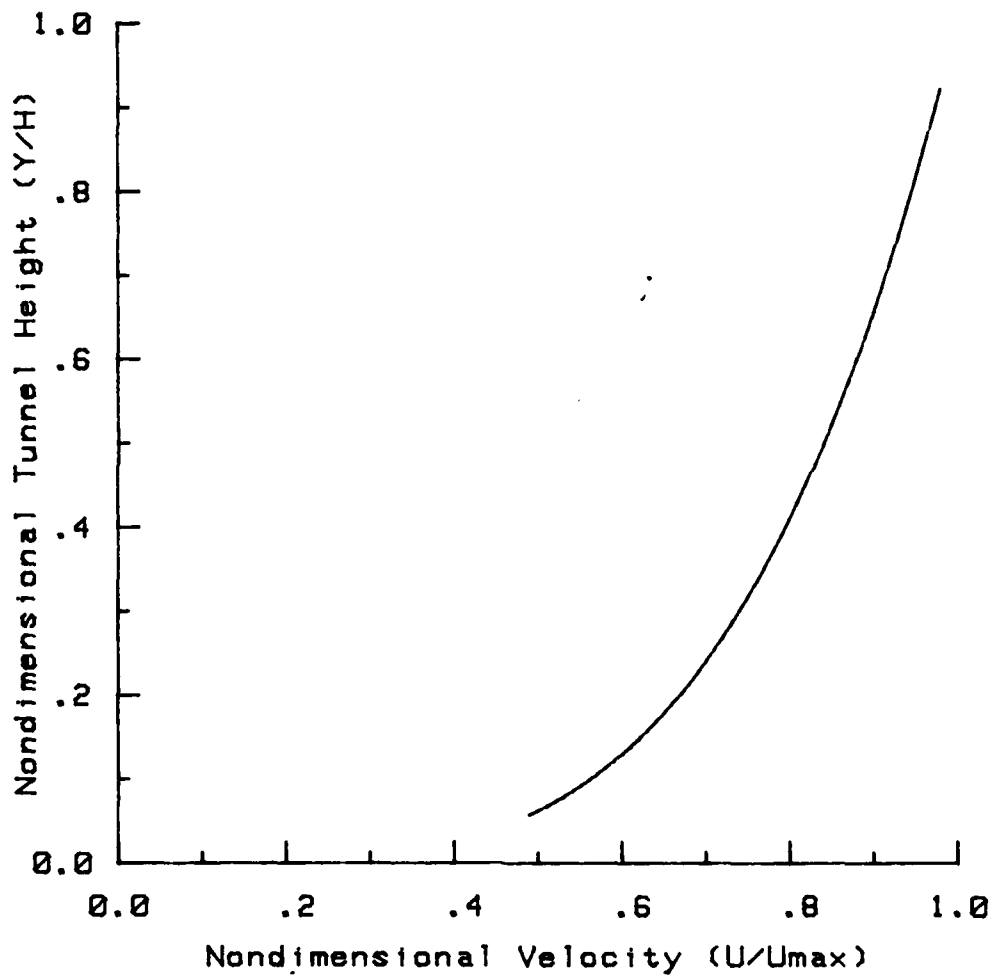


Figure 2. One-fourth Power Law Velocity Profile

Problem and Scope

Because the hot wire anemometer system and the ADAS are the main features of the wind tunnel, the interface between them receives the highest priority in automation. Accordingly, this thesis study centers on three areas: i) building the interface between existing wind tunnel instrumentation and the ADAS; ii) comparing experimental results obtained through the ADAS with similar experimental results obtained by McKnight; and iii) supporting future investigative work using the wind tunnel instrumentation/ADAS.

The most important part -- the scope -- of this research is an in-depth comparison with McKnight's work (item ii above). However also important to this research, integrating the ADAS (which requires a separate hardware effort) is a corollary task synthesizing four areas: i) the AFIT low speed wind tunnel, ii) the single element hot wire (film) anemometer instrumentation, iii) the ADAS, and iv) the anemometer sensor support traversing mechanism.

Approach and Presentation

As the traversing mechanism/anemometer interface was given the highest priority during the integration portion, the content of this writing will emphasize that aspect, as well as, run times and data storage requirements. (Neyland (ref. 20) and Kirchner (ref. 14) discuss results of work on another similar interface and another diagnostic tool, both of which can be used with this wind tunnel.) Following hardware/software development chapters, this report will compare results obtained with this system to results obtained by McKnight.

This report will give background information on the ADAS, on the test apparatus, and on the instrumentation in Chapter II and Appendix B. Completing the system description, Chapter III and Appendix A will describe the stepper motor -- an electromechanical solution to moving the sensor support. Chapter IV will discuss the hardware/software interface between the stepper motor and the ADAS. Chapter V will present the measurement techniques, results, and an evaluation of those results. Finally, Chapter VI will summarize by providing conclusions of this investigation.

II. Equipment Description

An equipment précis (ref. 9) serves to set the stage in describing the equipment used in this investigation: The test unit -- the low speed wind tunnel -- contains a 9 X 9 X 36 inch test cabin with a very low turbulence level. An open return system with a maximum speed of 80 feet per second, this unit gives a measured turbulence intensity level of 0.5 percent in a clean test cabin. A multi-channel hot wire anemometer and a two color photon correlation laser velocimeter are the major diagnostic tools to be used with the tunnel.

This chapter augments that description of the equipment -- apparatus, instrumentation, and automatic data acquisition system (ADAS).

Apparatus

Figure 3 pictures the AFIT nine inch, low speed, open circuit wind tunnel which provided the controlled flow for this study. Located in Room 142, Building 640, AFIT School of Engineering, this tunnel receives power via a 27 volt D.C., 1½ HP, 6500 rpm motor. The fine and vernier potentiometers on the motor control the velocity in the test cabin to within one foot per second. With a contraction ratio of 25, the tunnel provides a measured turbulence intensity level (u'/U_{mean}) of .5 percent in a clean test cabin. This level is within the electronic noise level of most electronic equipment used for this type of research. The boundary layer in the test cabin measures one inch at the design velocity of 30 feet per second.



Figure 3. AFIT Low Speed Wind Tunnel

During experimental runs, the flowfield provided by the apparatus consists of an approximately turbulence free uniform flow upstream of the test grid and a turbulent shear flow power law velocity profile downstream of the test grid -- illustrated in Figure 4. The velocity was held constant at about 30 feet per second for all wind tunnel runs; the uniform stream corresponds to a Reynolds number, based on rod diameter, of 2000. This Reynolds number is in the range where the boundary layer separation of the circular rods is laminar although the wake is turbulent (Corrsin, et. al.: ref. 15). The pre-placement of wood plugs in the test cabin ceiling dictates that the traversing mechanism be placed at set intervals along the test cabin center line.

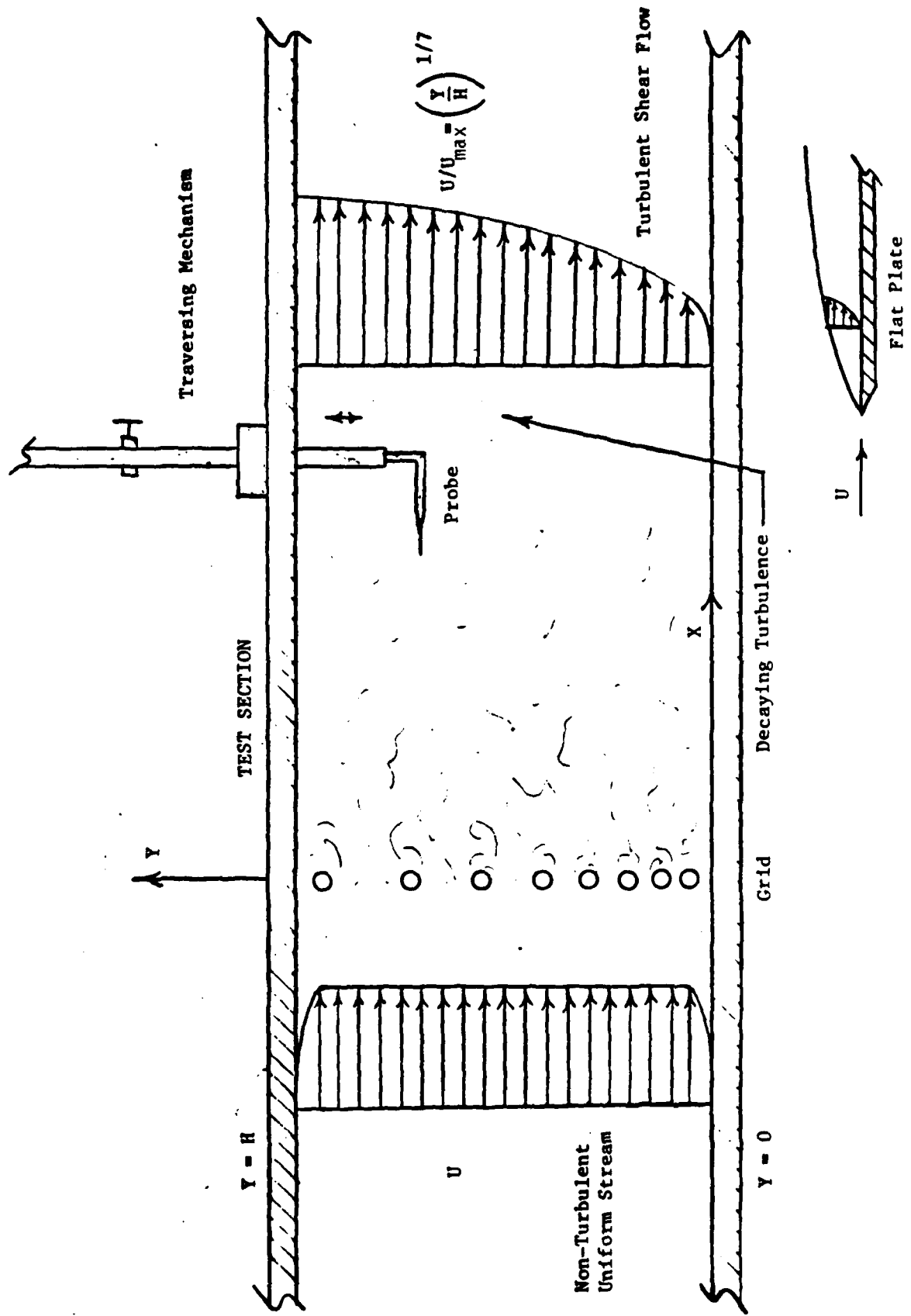


Figure 4. Test Cabin Flowfield, Adapted from Reference 15

The grid design facilitates the installation and removal of several different rod arrangements by using removable templates with one-eighth inch holes drilled to receive the rods. The need for minimum disturbance to the flowfield and minimum structural deformation dictates the size and shape, including streamlining, of the brass templates and supports. The templates are nine inches long by one inch wide and one-sixteenth inch thick. The circular aluminum rods are one-eighth inch in diameter. In place of a grid of rods, one series of runs uses a one-half inch cylinder. Figure 5 shows examples of the test grids and rods.

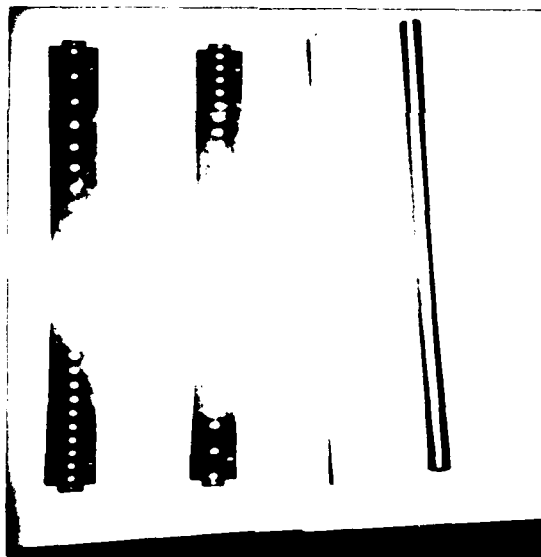


Figure 5. Grid Templates and Rods

To install a given grid, the templates were screwed into the supports. Then the rods were inserted from one side and were held in place by the plexiglass windows of the tunnel, as illustrated in Figure 6. During all runs, no vibration of the rods was observed.



Figure 6. Grid Installation

Instrumentation

Thermo-Systems, Incorporated (TSI) manufactures the primary instrumentation for this investigation. Used in several studies on turbulent flow (ref. 14 and 15), this instrumentation includes a constant temperature hot film anemometer system together with its associated electronic equipment and sensors. Figure 7 shows a photo of the instrumentation; Figure 8 presents a schematic of the instrumentation.

To process the signals from the hot wire sensor during the calibration and wind tunnel runs, a TSI Model 1050 anemometer works in the constant temperature mode with the bridge circuit optimized for maximum frequency/response (ref. 25). The output from the anemometer may be separated into a mean voltage and a fluctuating voltage, which correspond, respectively, to the mean and fluctuating velocities. The calibration procedure given in Appendix A presents the procedure to convert voltages to velocities.

The sensor used for this experimental data collection -- the model 1214-20 hot film sensor -- consists of a single wire (.0020 inches in diameter) aligned perpendicular to the mean flow direction, that is, along the Z-axis. A probe elbow, probe, and probe support (inserted in the traversing mechanism) complete the list of sensor attachments, pictured in Figure 9. A TSI Model 1125 calibrator (in conjunction with a Merriam water micromanometer, pressure transducers, and Textronix, Inc. Type 53A oscilloscope) was used to obtain the hot film sensor calibration curve (See Appendix A).

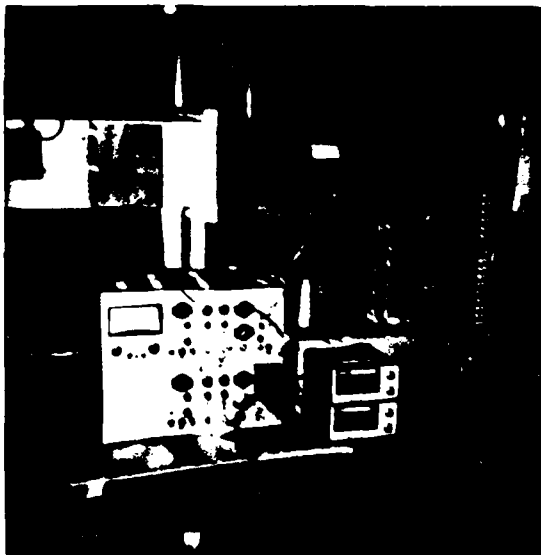


Figure 7. Hot Wire Instrumentation

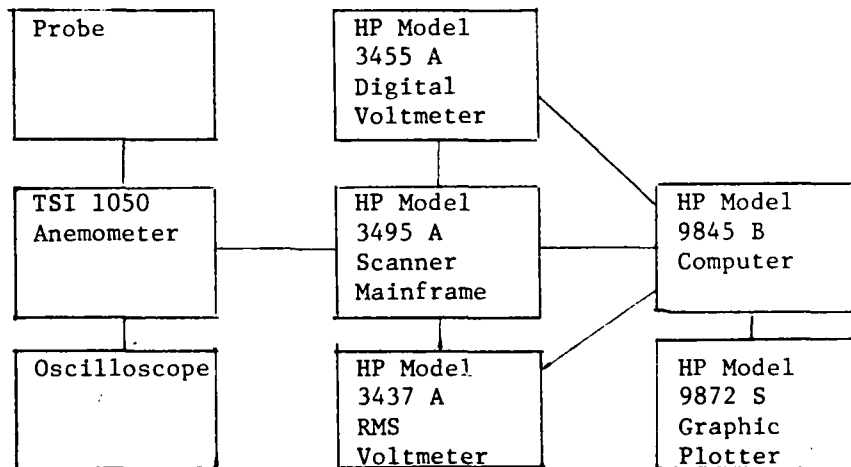


Figure 8. Hot Wire Instrumentation Schematic

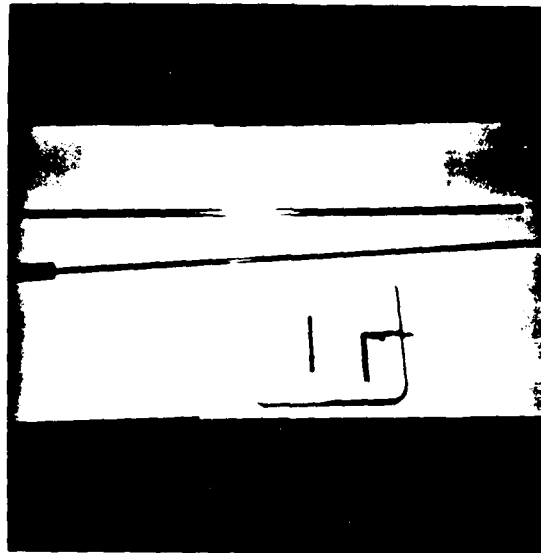


Figure 9. Sensor and Sensor Attachments

To measure the wind tunnel test cabin velocity, a Merriam four inch inclined manometer, attached to the wind tunnel just behind the test cabin, measured down to one-hundredth of an inch of water. Adjusted tunnel speed kept this manometer reading .3 inches of water, the test cabin static pressure.

Automatic Data Acquisition System (ADAS)

Figure 10 pictures the ADAS -- a computer system based around a Hewlett-Packard (HP) 9845B computer with a built-in cathode ray tube (CRT) display, thermal printer, two tape drives, an extended keyboard, two flexible disk drives, two digital voltmeters, a scanner, and a plotter. Each tape can hold 217K bytes of information; each disk 500K bytes. Figure 11 block diagrams the ADAS.

Additional features include a HP Model 9845T controller with 318K bytes total read-write memory, input/output read only memory, mass storage read only memory, input/output expander, graphic utilities, a terminal emulator, a 20 channel low thermal assembly, a 19 channel reference assembly, and several data interface cards. Also, specific equipment designations unique to this ADAS are a HP Model 3455 A digital voltmeter, 3437 A rms voltmeter, 98035 A Real Time Clock, 3495 A Scanner Mainframe, Model 9872 S Graphic Plotter with paper advance, and system software and documentation (ref. 10). The ADAS is stored in a 56 inch rack cabinet.

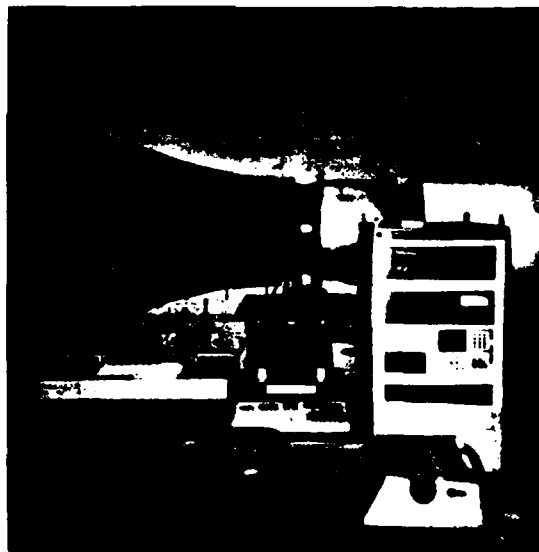


Figure 10. Automatic Data Acquisition System

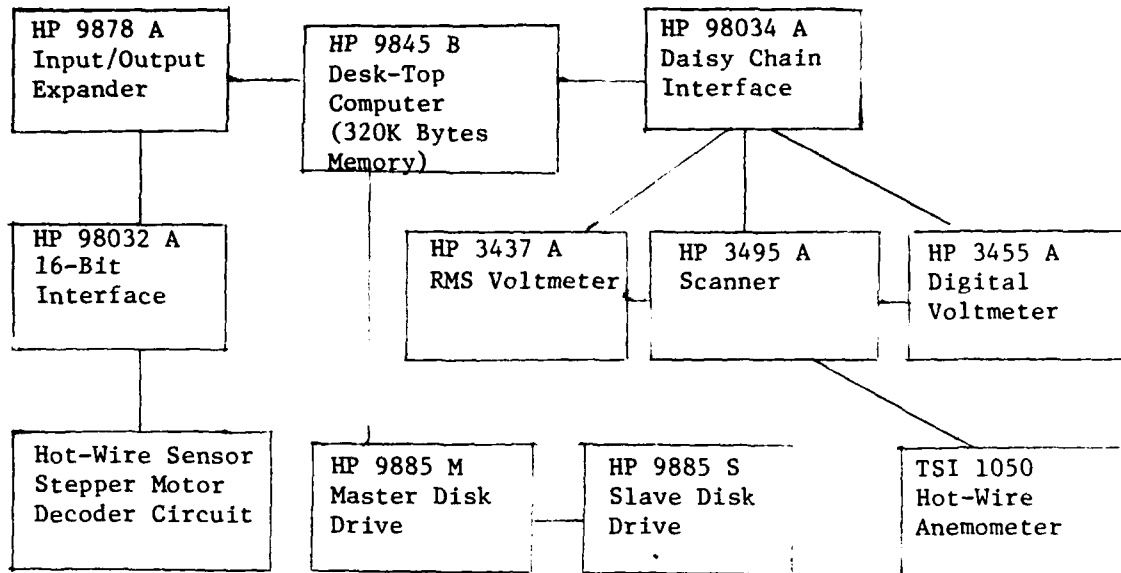


Figure 11. Automatic Data Acquisition System Block Diagram

III. The Stepper Motor: An Electromechanical Solution

In the study of turbulent fluid flow, hot wire anemometry historically results in tedious, time consuming processing of large quantities of data. An ADAS greatly streamlines the more routine tasks of electronic and electromechanical equipment control, data transfer and recording, and computations. Integrating these tasks through an ADAS provides the user with a greatly increased capability to conduct real-time turbulence studies using a hot wire anemometer.

As hot wire anemometry physically inserts a probe into the flow field, manual positioning of the sensor is a task that must always be done. Because stepper motors can provide fast, accurate positioning, they are instrumental participants in the automation of manual mechanical systems. Many of these kinds of manual mechanical systems are still in use in university engineering laboratories. A case in point is AFIT's laboratory housing the low speed wind tunnel.

Past research work in this tunnel has relied to a large extent on the operator placing the hot wire (film) anemometer sensor at desired locations, monitoring experimental controls (indicating temperature or pressure or voltage), and intervening in the event of aberrations in test conditions. To greatly improve low speed wind tunnel experiments, McKnight proposed automating the data collection. While the conventional anemometer system, which provides raw data as voltages, facilitated direct ADAS connection, the manual positioning

of the anemometer sensor at each data point did not. Consequently, in automating this total "system," applying a stepper motor to the anemometer sensor support complimented an anemometer sensor/ADAS coupling.

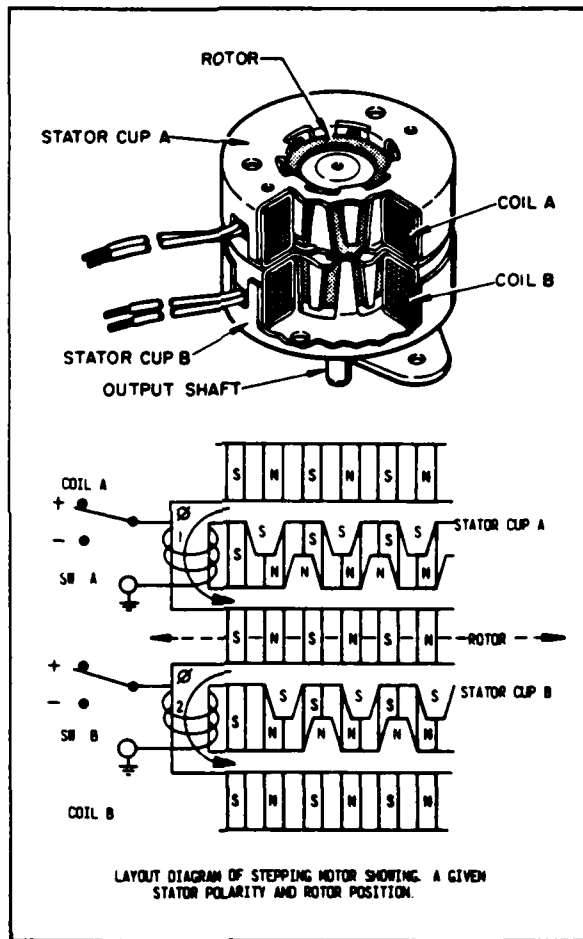
Description

Motiwalla (ref. 18) defines a stepper motor as "an electromagnetic incremental actuator which converts digital pulse inputs to discrete motion steps." In generating these steps, Motiwalla states that "the key to stepping motor performance lies in the design of a rotor and stator combination that has regularly spaced equilibrium positions created by alternating magnetic poles. (Figure 12 outlines the principle parts of a stepper motor.) In its most common form, the rotor is constructed of a ceramic permanent magnet that has a fixed pattern of alternating north and south poles and a stator made from two sets of toothed soft-iron cups energized by separate windings. The teeth on the cups are folded so that when energized they form alternating poles that interact with the rotor fields, producing either movement or a holding torque. The pole patterns created by the two windings are 90° out of phase. Therefore, by selectively switching the windings the motor will either step forward or in reverse."

Stepper Motor Control

When running stepper motors, two problems generally occur because of motor inertia and load. These problems are that the stepper motor will slip or oscillate at the end of each step.

To correct the first of these problems, operating the motor within its torque/step rate envelop (illustrated in



Cutaway 2 of Permanent Magnet Stepper Motor.

Figure 12. Stepper Motor Schematic
Adapted from Reference 23

Appendix A) prevents slippage. Then, motors may be run "open loop," in which (according to Motiwalla) "you can tell where its shaft is (relative to some initial position) merely by keeping track of the number of steps sent to the motor." Figure 13 illustrates the stepper motor control system. In this figure adding feedback through an encoder or displacement transducer results in "closed loop" control.

To correct the second of these problems, coupling the motor with a driver (also detailed in Appendix A) prevents oscillatory tendencies. By pulsing the motor a preset number of times, the driver effectively cancels overcompensation with equal amounts of undercompensation. Thus, the driver sequencing logic provides the necessary compensation so that errors over a certain range are non-cumulative. For example, the motors used in this project move in 7.5° increments with oscillations at the end of each step. Through a driver (actually an integrated circuit), four sequenced pulses to the motor result in a 30° turn with all inherent oscillations equally compensated: a motor attached to this driver turns exactly 30° . Contained within the driver along with the sequencing logic comes some circuitry to control the power supplied to the motor windings. The user builds the remaining circuitry. Together the driver and the user-built circuitry make up what is called an interface box, constructed in a familiar "bud" box.

Besides the interface box and stepper motor, another physical component unique to this system had to be added: this component was the traversing mechanism.

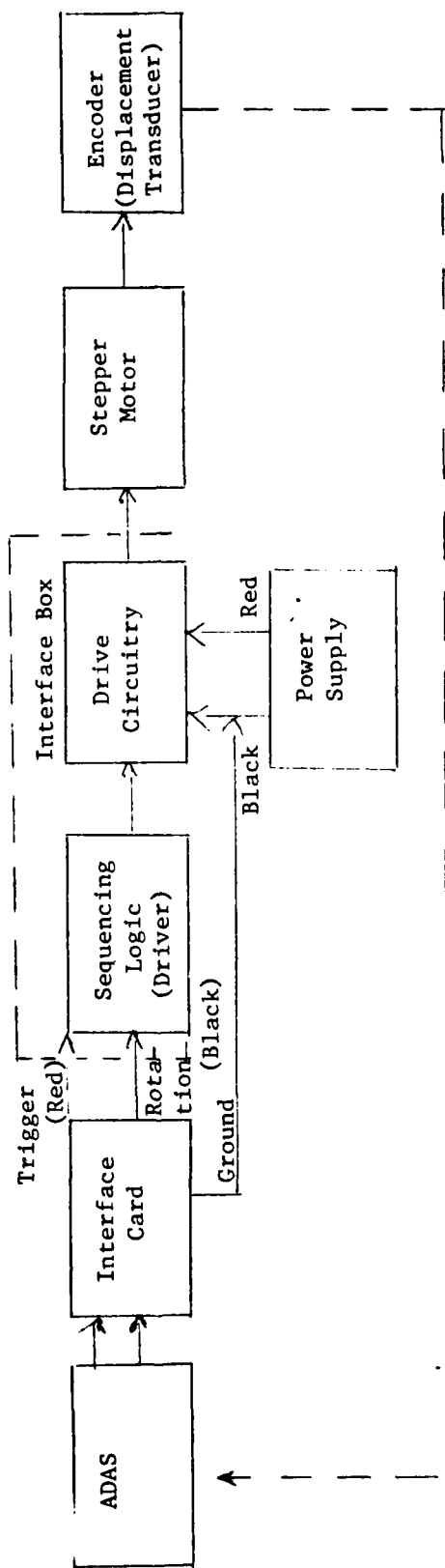


Figure 13. Stepper Motor Control System

Mechanical Design

To make the nine inch vertical traverse in the low speed wind tunnel, the traversing mechanism design calls for inserting a fourteen inch sensor support in a brass tube whose inner diameter is just slightly larger than the outer diameter of the sensor support. Threaded on the outside, the tube moves vertically -- with no rotation -- through the action of a double threaded bronze worm gear and steel worm that is coupled to the stepper motor. Figure 14 pictures the complete traversing mechanism, displacement transducer, stepper motor, and interface box. When triggered by the ADAS, a step of the

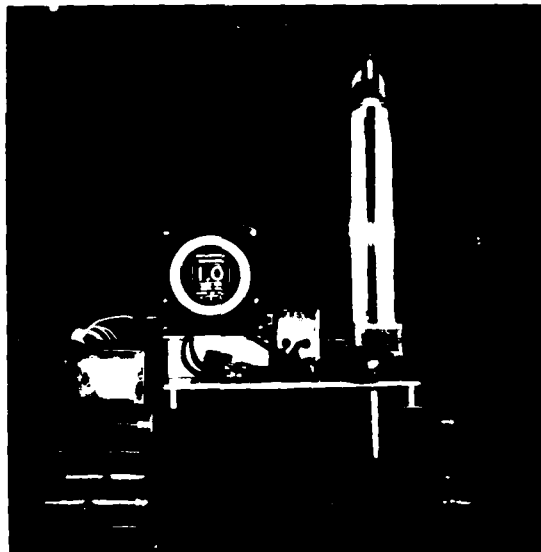


Figure 14. Traversing Mechanism

stepper motor (a 30⁰ turn) moves the sensor support 0.00005 inches -- a calibrated value used in open loop operation. The traversing mechanism can be operated closed loop by using the displacement transducer, which provides the ADAS feedback on position. Two additional items to the basic traversing mechanism include limit switches, which can be wired into the stepper motor circuit as failsafes, and a four threaded bronze worm gear and steel worm, which will double the speed.

Appendix A provides manufacturer's specifications on the driver and two different motors used in this project. The Stepper Motor Handbook (ref. 23) contains further information on the stepper motors used in this project. Also, the Robot Users Manual (ref. 8) and the Proceedings of the Symposia on Incremental Motion and Control Systems and Devices (see, for example, ref. 6, 24) provide experimental and theoretical studies of stepper motors.

IV. The Interface

The interface box converts the electronic pulses of the computer to electromagnetic signals, which eventually produce mechanical energy (shaft power) in the stepper motor. Before describing the interface box, one additional physical component needs mentioning -- the interface card. The HP 98032A Input/Output Interface (the interface card) is a general purpose interface providing two-way, 16-bit data exchange between the ADAS and peripherals, such as the stepper motor.

Interface Card

A fifteen foot cable coupled to a plug (card), the interface cord connects the ADAS to the interface box. Although the plug end is essentially fixed in configuration (except for setting the interface select code), the cable's open end configures to suit the design of the particular interface. Pictured in Figure 15, represented schematically in Figure 16, the interface card used in this project was modified for this project by attaching wires PCTL to PFLG (19 to 19) and isolating; by attaching wires GND, GND (1,1), GND, DRAIN (18,18), GND, GND (24,24), and DRAIN (25) all together and routing to the common ground of the interface box; and by attaching wires D00 (17) and D01 (16) to separate plugs. These plugs insert in the interface box housing containing the stepper motor drive and drive circuitry. Enabling D00 triggers the stepper motor (T in Figures 18, 19; physically the red plug); enabling D01 changes the rotation (R in Figures 18, 19; physically the

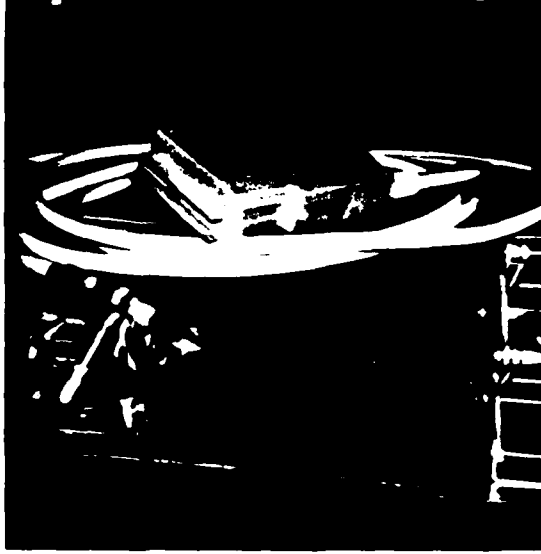


Figure 15. Interface Card

black plug). Figure 17 illustrates the cable.

Interface Box Circuitry

Because the motor, motor driver, and interface card operate with completely different electrical configurations, auxiliary circuitry provides the necessary coupling to convert the transistor-to-transistor logic (TTL) of the ADAS to the motor drive requirements. Since this project looked at two types of stepper motors (unipolar and bipolar), Figures 18, 19, and 20 show the two different circuits breadboarded in this project. The unipolar circuit has positive pull-up connections with low gain open collectors driving each motor winding; the bipolar circuit, in addition, has zener diodes in tandem with optoisolators and a bipolar power supply. The bipolar motor yields

Standard Interface Cable

WIRE COLOR	SIGNAL	A B		SIGNAL	WIRE COLOR
WH-BK-GN	GND	1	1	GND	WH-BK-BU
WH-YL-GY	DO15	2	2	DI15	WH-RD-BU
WH-YL-VIO	DO14	3	3	DI14	WH-RD-GN
WH-YL-BU	DO13	4	4	DI13	WH-RD-YL
WH-YL-GN	DO12	5	5	DI12	WH-RD-OR
WH-OR-VIO	DO11	6	6	DI11	WH-BN-GN
WH-OR-BU	DO10	7	7	DI10	WH-BN-YL
WH-OR-GN	DO9	8	8	DI9	WH-BN-OR
WH-OR-YL	DO8	9	9	DI8	WH-BN-RD
WH-VIO	DO7	10	10	DI7	VIO
WH-BU	DO6	11	11	DI6	BLU
WH-GN	DO5	12	12	DI5	GRN
WH-YL	DO4	13	13	DI4	YEL
WH-OR	DO3	14	14	DI3	ORG
WH-RD	DO2	15	15	DI2	RED
WH-BN	DO1	16	16	DI1	BRN
WH-BK	DO0	17	17	DI0	BLK
WHT	GND	18	18	DRAIN	(INNER BARE WIRE)
WH-GY	PCTL	19	19	PFLG	GRY
WH-BK-BN	I/O	20	20	PSTS	WH-BK-GY
WH-BK-RD	PRESET	21	21	EIR	WH-BN-GY
WH-RD-VIO	CTL0	22	22	STI0	WH-BN-BU
WH-RD-GY	CTL1	23	23	STI1	WH-BN-VIO
WH-BK-OR	GND	24	24	GND	WH-BK-YL
(OUTER BARE WIRE)	DRAIN	25	25	NC	

Figure 16. Standard Interface
Adapted from Reference 10

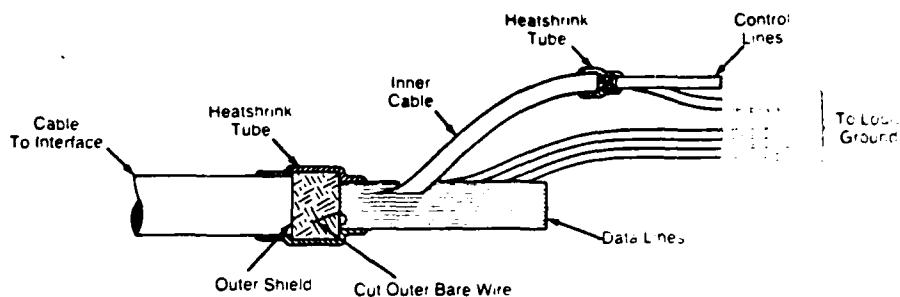


Figure 17. Interface Cable
Adapted from Reference 10

a higher torque (See Appendix A) but requires considerably more circuitry.

Software

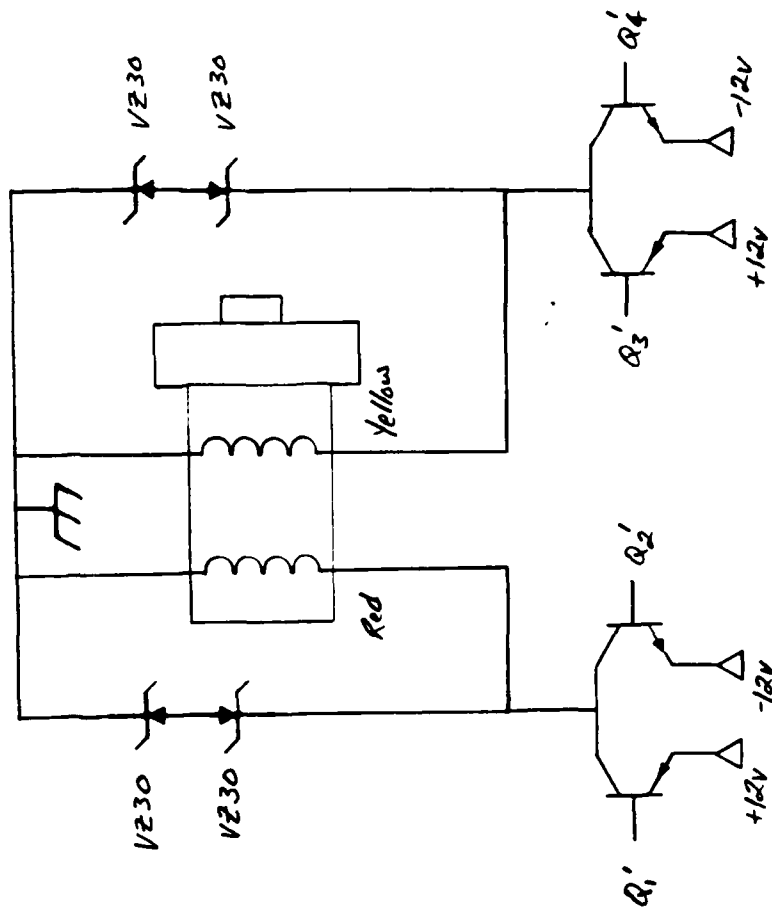
The ADAS uses BASIC as the source language for the software. The following commands trigger and rotate the motor (clockwise rotation equates through gearing to an up traverser movement):

```

FOR I = 1 TO 765
  RESET 4
  WRITE BIN 4;Ud2
  RESET 4
  WRITE BIN 4;Ud1
NEXT I

```

During this loop (after 765 times), the traversing mechanism moves 0.04 inches -- a figure based on a counted calibration run. RESET 4 resets the interface card. (Select code number 4 is the interface card configured to run the traversing mechanism via the stepper motor.) WRITE BIN 4;Ud2 sends a 16-bit binary number to interface card (select code number) 4,



NOTE: Q1', Q3' ARE 2N1131
 Q2', Q4' ARE 2N4921

NOTE: Q1' AND Q3' MUST BE 1 WATT
 80V SILICON PNP TRANSISTORS
 WITH LOW GAIN. DO NOT USE
 A TRANSISTOR WITH A GAIN
 HIGHER THAN 50 (15-50 RECOMMENDED).

Figure 20. Bipolar Drive Circuit (continued)

which, in turn, sends the binary number through the card cable to the interface box. Ud1, Ud2 are decimal values of the binary numbers to be sent. If the traverse is down, Ud1=0; up, Ud1=2. Then Ud2=Ud1+1. So that two combinations of two binary numbers could be sent--

<u>Traverse</u>	<u>Decimal Number</u>	<u>Converted to Binary:</u>
down	Ud1=0	0000000000000000
	Ud2=1	0000000000000001
up	Ud1=2	0000000000000010
	Ud2=3	0000000000000011
		AB

The rotation or direction bit (column A) corresponds to wire D01 on the interface card; the trigger bit (column B) corresponds to wire D00 on the interface card. When triggering the motor to move, the sequence of commands listed in the loop works best albeit redundant in resetting bits.

V. Results and Discussion

Parameters commonly used to characterize a one-dimensional turbulent fluid flow field with the aid of a hot wire (film) anemometer system include U , U_{mean} , U_{max} , u' , x , y , and their nondimensionalized values. To facilitate comparison between data obtained here and data obtained by McKnight (who presented his data in nondimensional form), this chapter presents data in nondimensional form and not in raw data form -- although either form is acceptable. Appendix C contains the raw data. This chapter discusses the experiments conducted (to obtain those parameters) with the complete system described thus far.

Measurement Technique

Prior to each test run, the traversing mechanism and 90° elbow were inserted at the proper x -location test station. The sensor was then attached to the elbow and was aligned according to centerline markings. During the actual experiments, all traverses were run between 8.5 and 0.5 inches from the tunnel bottom -- to protect the sensor during installation and removal. Calibrated at 0.0000523 inches/motor step, the traversing mechanism was placed at $X/H = .44$, 1.56, and 3.22 tunnel heights downstream of the grid. (Results in both x and y were nondimensionalized by the tunnel height H (= 9 inches).) Data was obtained at intervals equivalent to 25 points/inch or to 200 points/8 inch traverse.

Direct readouts of the voltages from the digital voltmeter and the rms meter provided the mean and fluctuating voltages,

which could then be converted to the respective velocities. The mean velocity conversion directly used the calibration curve (See Appendix A). The fluctuating velocity conversion used the procedure of Zakanwycz (ref. 27), who computed u' from measured true rms values (e') through the equation:

$$e' = a_i u'$$

From calibration data, the conversion factor a_i represented the slope at discrete points on the calibration curve. Differentiating the calibration curve yielded the slope $dE/d\bar{U}$. Evaluating this for each test data point i (of voltage value E_i) provided a_i . The experimental value of e' , together with the newly calculated a_i , resulted in u' . In practice $d\bar{U}/dE$ ($= 1/a_i$) came from Figure 61.

To compare data with McKnight, U_{max} nondimensionalized the local mean velocity and U_{mean} nondimensionalized the fluctuating velocity. Obtaining data every 0.04 inches, the ADAS reduced and recorded the data in the graphs presented in this chapter and in Appendix C.

The data logging cycle consisted of advancing the stepper motor a certain number of steps, then holding the traverser position fixed while accumulating voltage data from the anemometer system. The following software commands obtained the data:

```
1      RESET 7
2      OUTPUT 709;"C21"
3      OUTPUT 722;"R7,F1,T1,M3,A1,H0"
4      TRIGGER 722
5      ENTER 722;Vt
6      OUTPUT 722;"R7,F2,T1,M3,A1,H0"
```

```

7          TRIGGER 722
8          WAIT 5000
9          V=0
10         FOR I=1 TO 5
11         TRIGGER 722
12         ENTER 722;Vrms
13         V=V+Vrms
14         NEXT I
15         V=V/5

```

The logic behind this sequence was:

- 1 Reset the scanner interface.
- 2 Obtain a reading on unit #709 (the scanner); read channel 21 on the scanner.
- 3 Route the information to Unit #722 (the voltmeter); obtain the direct current (DC) voltage, function F1.
- 4 Trigger #722 to send the information.
- 5 ADAS to enter #722's information; store in a variable called Vt.
- 6 Same sequence as 3 except now obtain the root-mean-square (rms) voltage, function F2.
- 7 Same as Step 4.
- 8 Instead of entering the reading, wait 5 seconds. Experience found that the first rms readings invariably were twice as high as any other -- due probably to the auto-calibration (autoscale) function within the rms meter.
- 9 Set rms voltage to zero.
- 10-14 Sum up five rms readings.
- 15 Obtain an average rms reading.

The DC voltage (Vt) was converted directly to velocity using

the third order calibration curve listed in Appendix B. By differentiating the third order calibration curve equation, evaluating that equation at the DC voltage (V_t) to obtain the slope $1/a_i$, and finally multiplying by the average rms reading, the fluctuating velocity (u') resulted.

Performance of the System

Typical eight inch experimental traverses (powered by the stepper motor) ran on the order of an hour and 45 minutes; the ADAS took 25 readings per inch, about 10 seconds per reading. Traversing used about one-half hour; reading voltmeters took approximately one hour -- mostly to obtain an average root-mean-square (rms) voltage reading. The traverse speed can be doubled by changing the gearing; the voltmeter reading speed perhaps can be increased. This is because the voltmeter employs an automatic calibration (AUTO CAL) feature (which automatically corrects for possible gain and offset errors in the analog circuitry to provide maximum accuracy). Consequently, in DC mode the voltmeter has a maximum reading rate of 24 readings per second whereas in AC mode the reading rate is 1.3 readings per second. The AC rate is thus fairly slow, and even slower when compiling an ensemble average (as was done here). Sacrificing the averaging procedure may sacrifice the confidence of the statistics.

Two minor problems cropped up with regard to the stepper motor circuit:

- i) Because the pull-up capacitor was not quite matched to the driver, the capacitor would discharge once every 10 seconds or so resulting in a slight hesitation or skip in the

motor. The resulting loss of one pulse to the motor did not affect accuracy in the traverse, as the motor calibration over an 8.375 inch traverse accounted for this effect. Replacing the pull-up capacitor will correct this problem.

ii) Manufacturer's data sheets on the stepper motors (Appendix A) have an error which affects the pulsing of the motor windings and, consequently, affects the design of the circuitry. The manufacturer's recommended pulse sequence, that is Q (a transistor): on, off, on, etc. was found to be in error. To correct this problem: relable the Q₄ column to Q₃, relable the Q₃ column to Q₄. This fixes the problem. The circuits presented in this report include this correction.

Tests Run

To test the automation of the anemometer sensor support, five sets of runs were made in the low speed wind tunnel. Data was collected with a single hot film sensor mounted on the traversing mechanism, which in turn was mounted on the center line of the test section. Vertical traverses were made with the sensor located at $X/H = .44, 1.56, \text{ and } 3.22$ (4, 14, and 29 inches, respectively, downstream from the grid) tunnel heights downstream from a turbulence generating device placed in the wind tunnel.

The turbulence generating devices were based on the work of McKnight in which he investigated turbulent shear flow velocity profiles behind a grid of parallel rods of variable spacing: "Grid A represented the one-seventh power-law design,

modeling the turbulent boundary layer velocity profile over a flat plate, while Grid B represented the one-fourth power-law profile to show the applicability of the method to other shear flows. For Grids A and B, Case 1 represents those grids designed . . . using Cockrell and Lee's Method . . . For Grid A, a third case was run using the same number of rods as in Case 1, but with the rod-spacing obtained by {a} modified method." Grid A had 25 rods; Grid B had 26 rods. Typical raw data results are in Figures 21-23, which show the velocity profiles for Grid A, Case 1.

To the three runs based on the above devices (designated Grids A1, A3, B1), two more sets of runs were added. One was with a $\frac{1}{2}$ inch diameter cylinder installed in lieu of a grid of rods (to see the effect of a change in diameter); the other was with no grid installed to establish a baseline case.

No Grid.

To establish a basis for comparison, test section velocity profiles (Figures 24-26) and turbulence intensity profiles (Figures 27-29) were obtained with no grid installed. Runs were accomplished with the centerline velocity at 31 feet per second. Based on the velocity profiles throughout the test cabin, the boundary layer thickness was located at one inch. However, when examining turbulence intensity, smooth flow consistently was maintained in the region just slightly inside: $.2 < Y/H < .8$ (1.8 inches $< Y < 7.2$ inches). According to Schlichting (ref. 22), the flat plate boundary layer thickness is 0.8 inches.

VELOCITY PROFILE

Grid A1

Sensor located 3.96 inches downstream from grid.

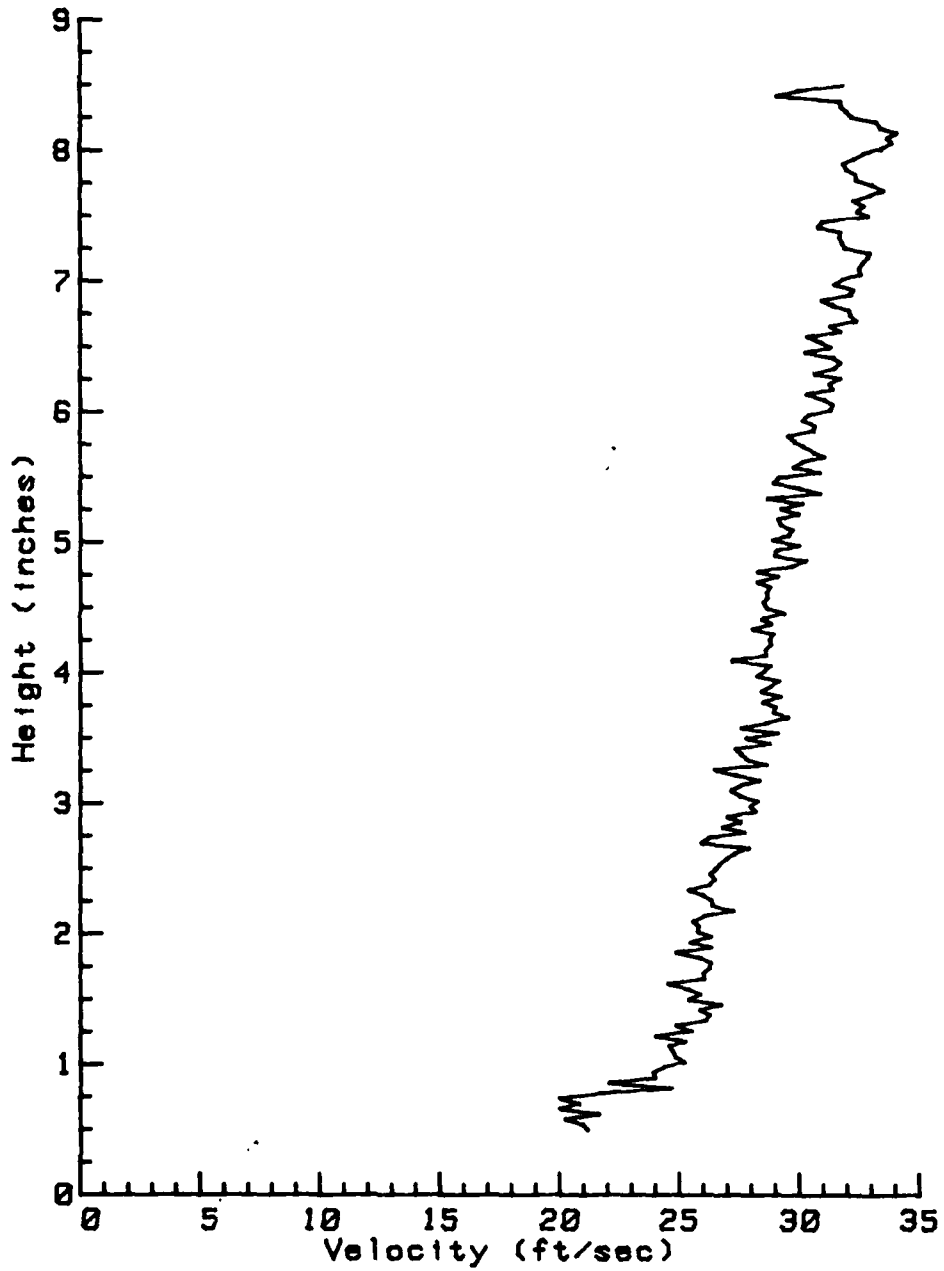


Figure 21. Velocity Profile, Grid A1, X = 4 inches

VELOCITY PROFILE

Grid A1

Sensor located 14.04 inches downstream from grid.

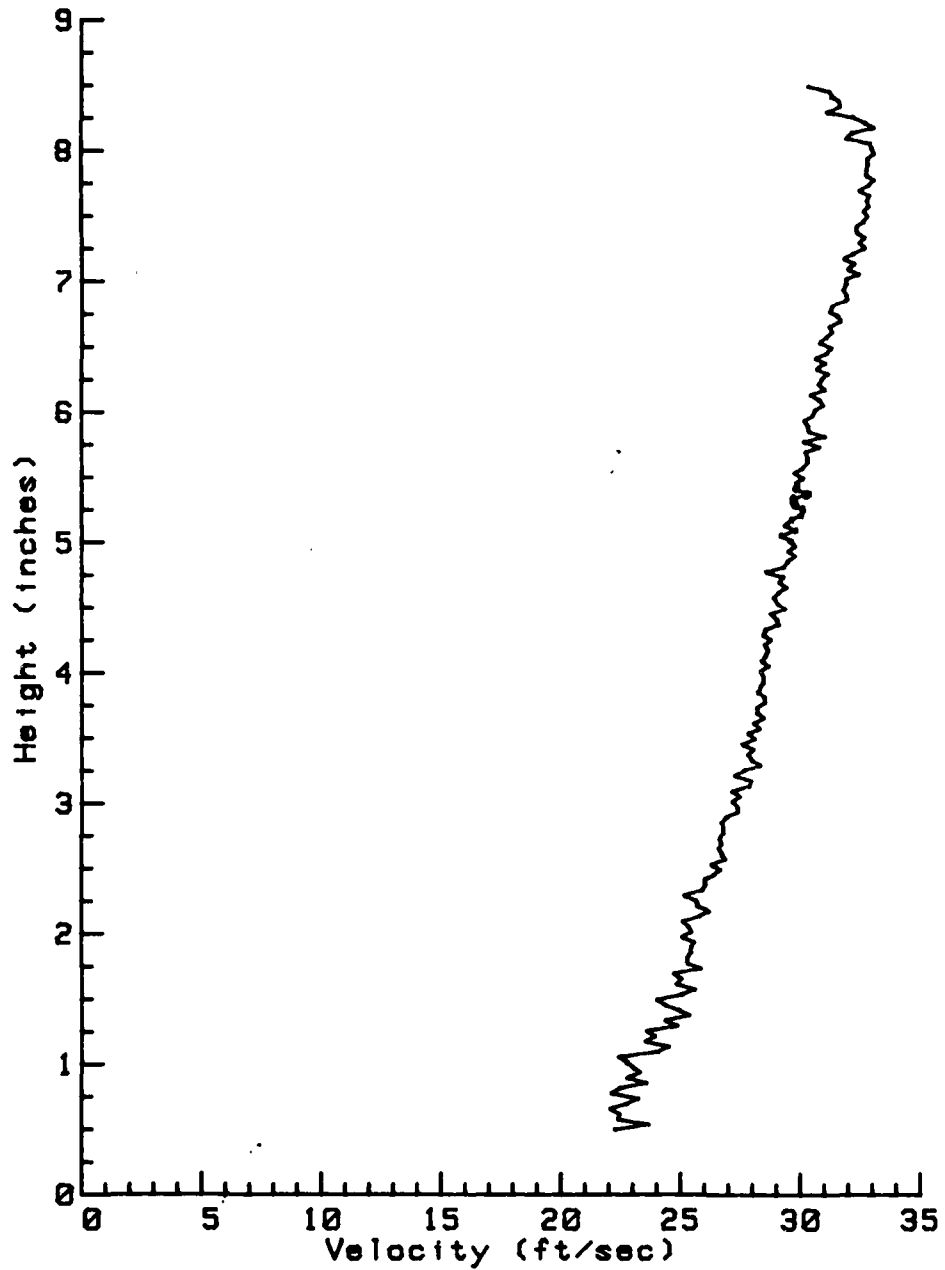


Figure 22. Velocity Profile, Grid A1, X = 14 inches

VELOCITY PROFILE

Grid A1

Sensor located 28.98 inches downstream from grid.

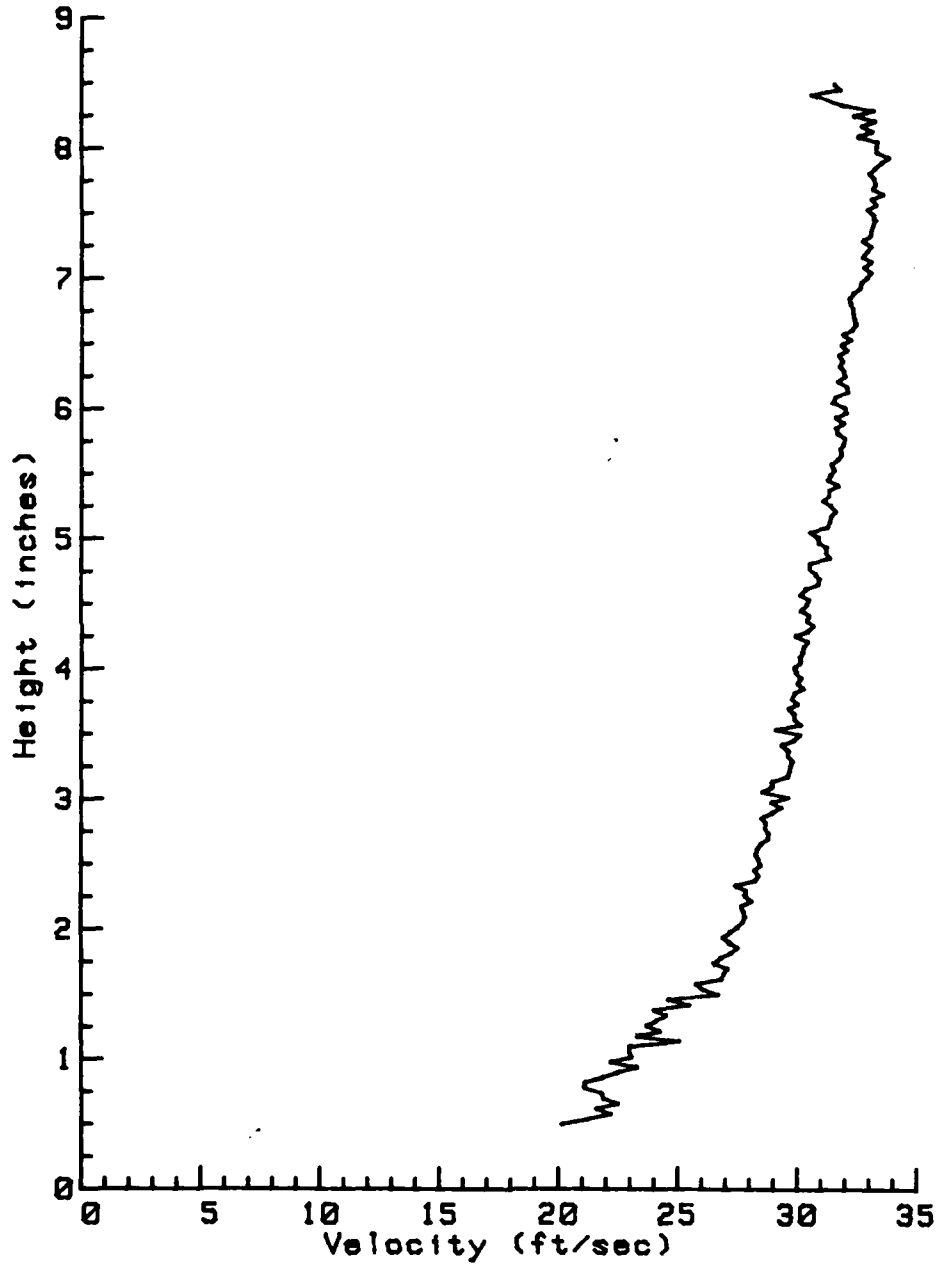


Figure 23. Velocity Profile, Grid A1, X = 29 inches

VELOCITY PROFILE

No Grid

Tunnel heights downstream from grid (X/H) = .44

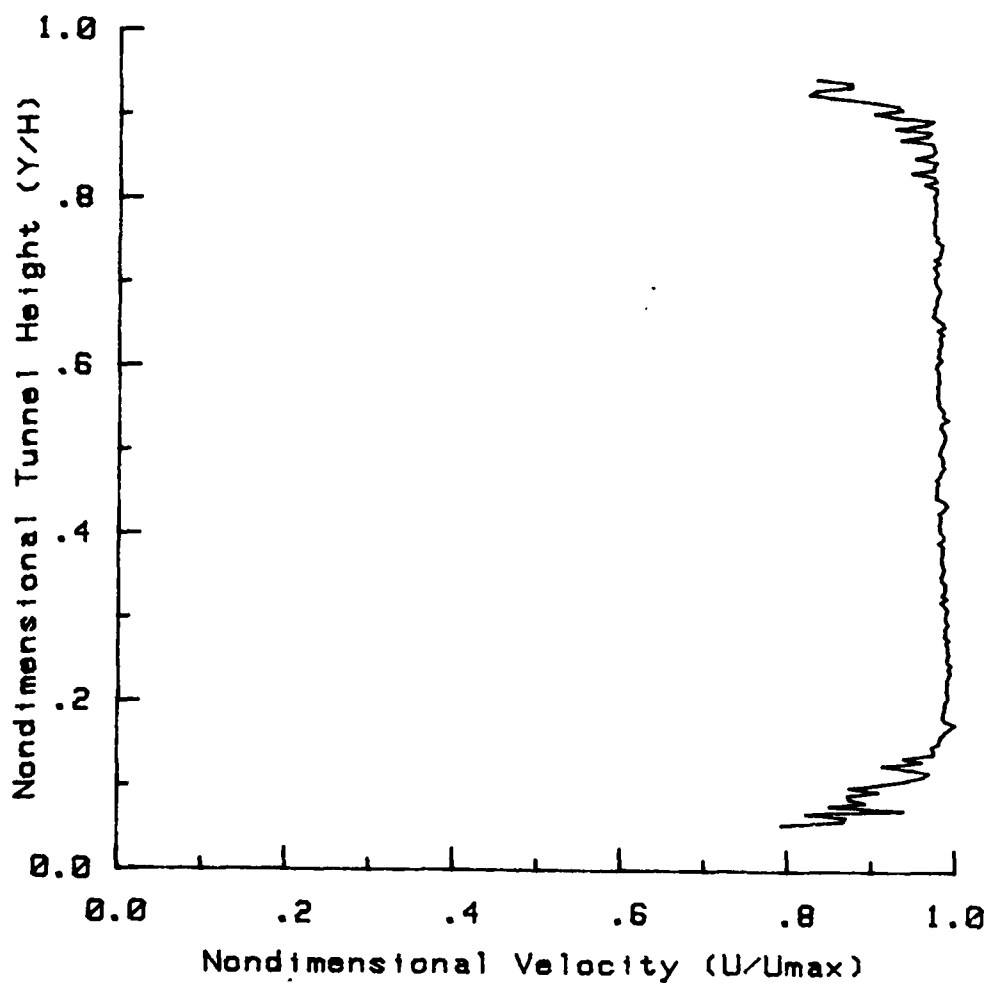


Figure 24. Nondimensional Velocity Profile, No Grid, X/H = .44

VELOCITY PROFILE

No Grid

Tunnel heights downstream from grid (X/H) = 1.56

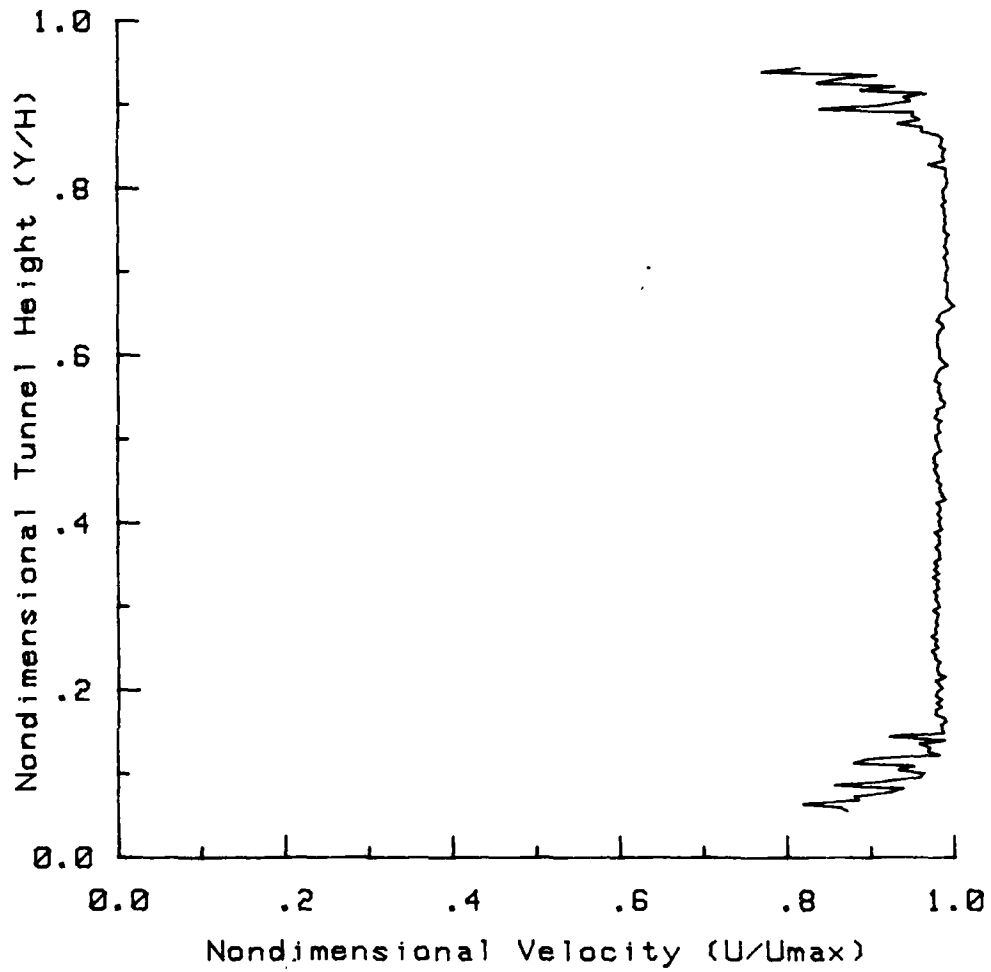


Figure 25. Nondimensional Velocity Profile, No Grid, $X/H = 1.56$

VELOCITY PROFILE

No Grid

Tunnel heights downstream from grid (X/H) = 3.22

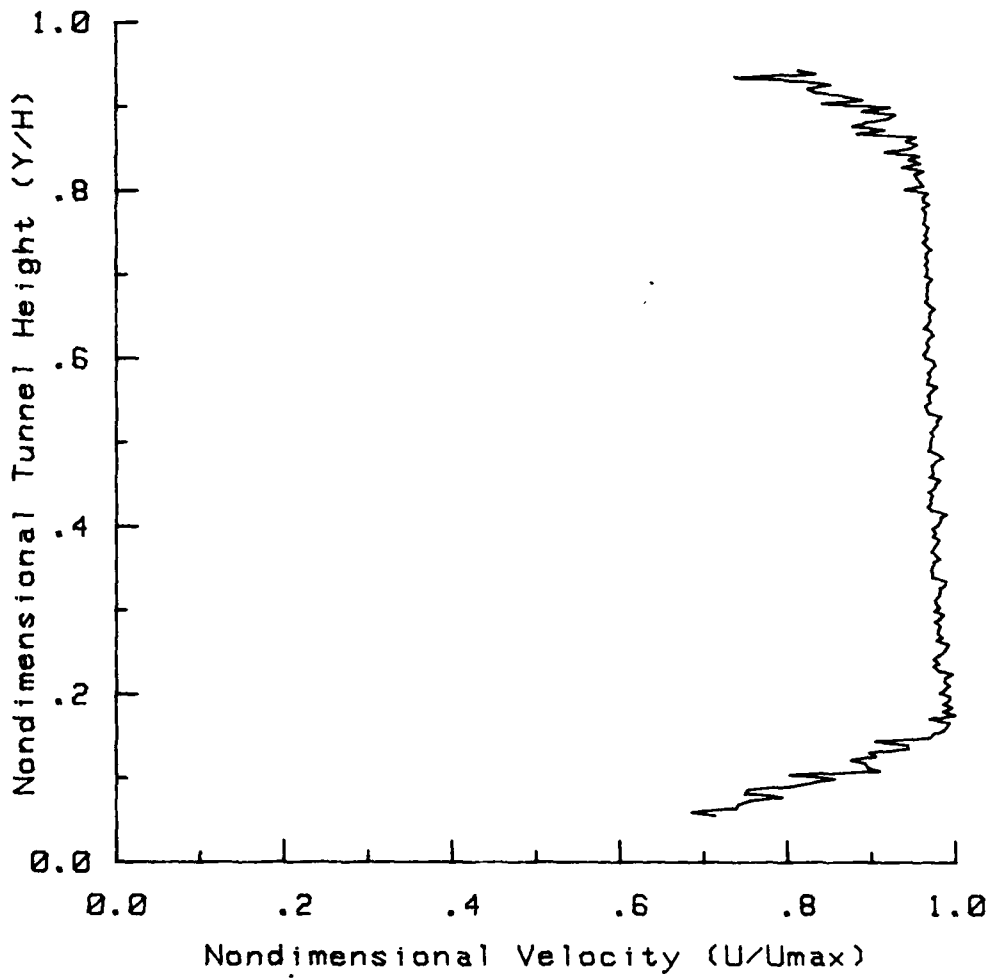


Figure 26. Nondimensional Velocity Profile, No Grid, $X/H = 3.22$

TURBULENCE PROFILE

No Grid

Tunnel heights downstream from grid (X/H) = .44

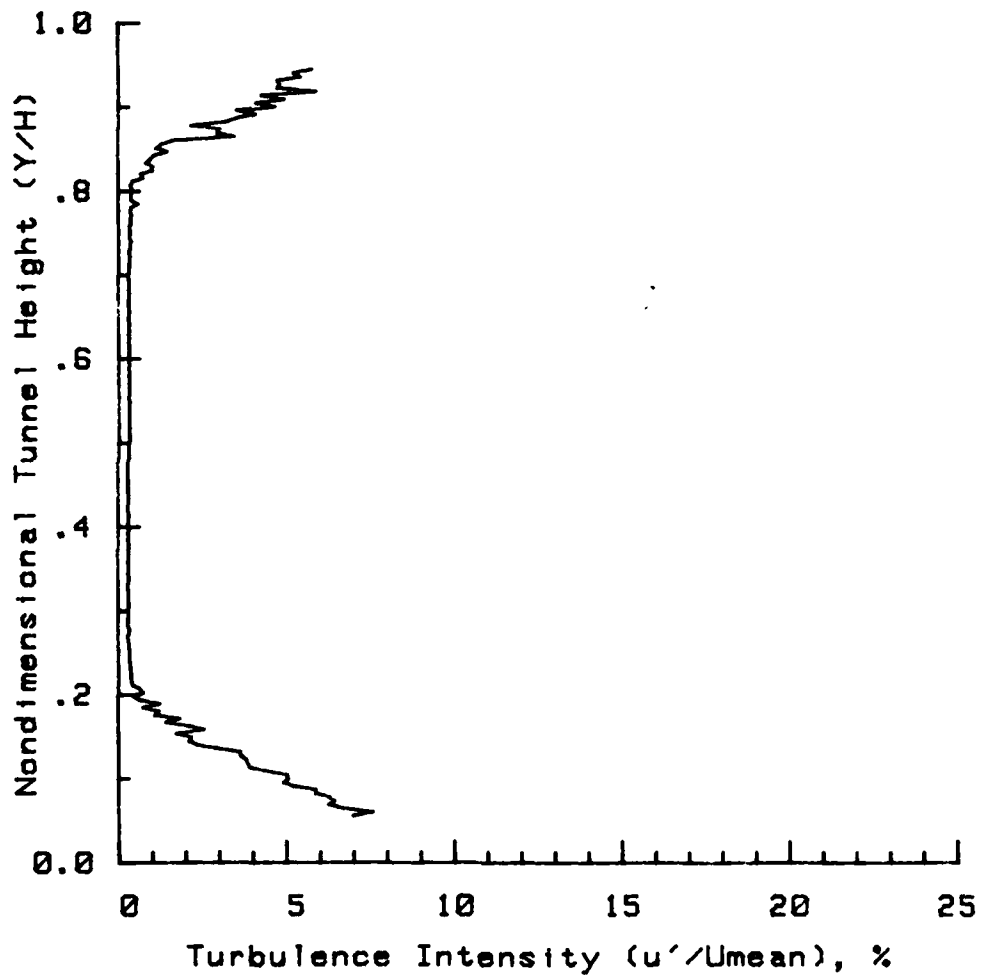


Figure 27. Turbulence Intensity Profile, No Grid, X/H = .44

TURBULENCE PROFILE

No Grid

Tunnel heights downstream from grid (X/H) = 1.56

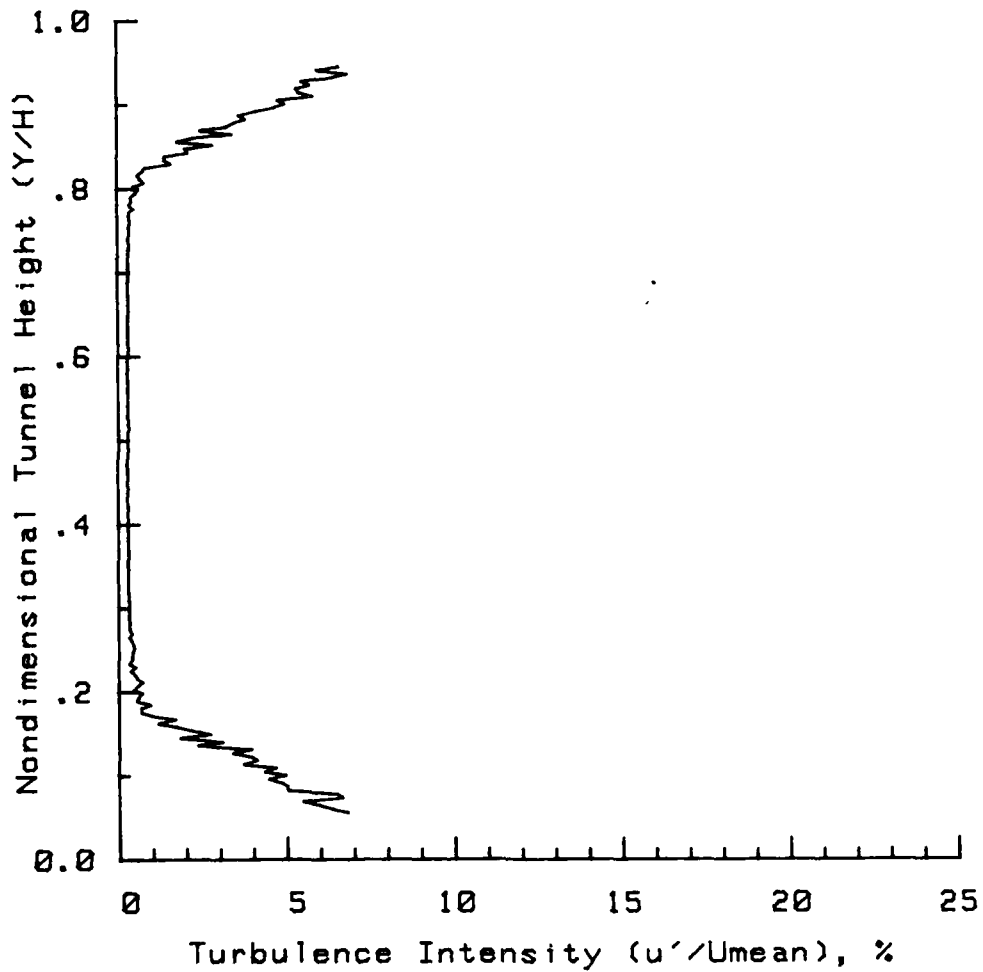


Figure 28. Turbulence Intensity Profile, No Grid, X/H = 1.56

TURBULENCE PROFILE

No Grid

Tunnel heights downstream from grid (X/H) = 3.22

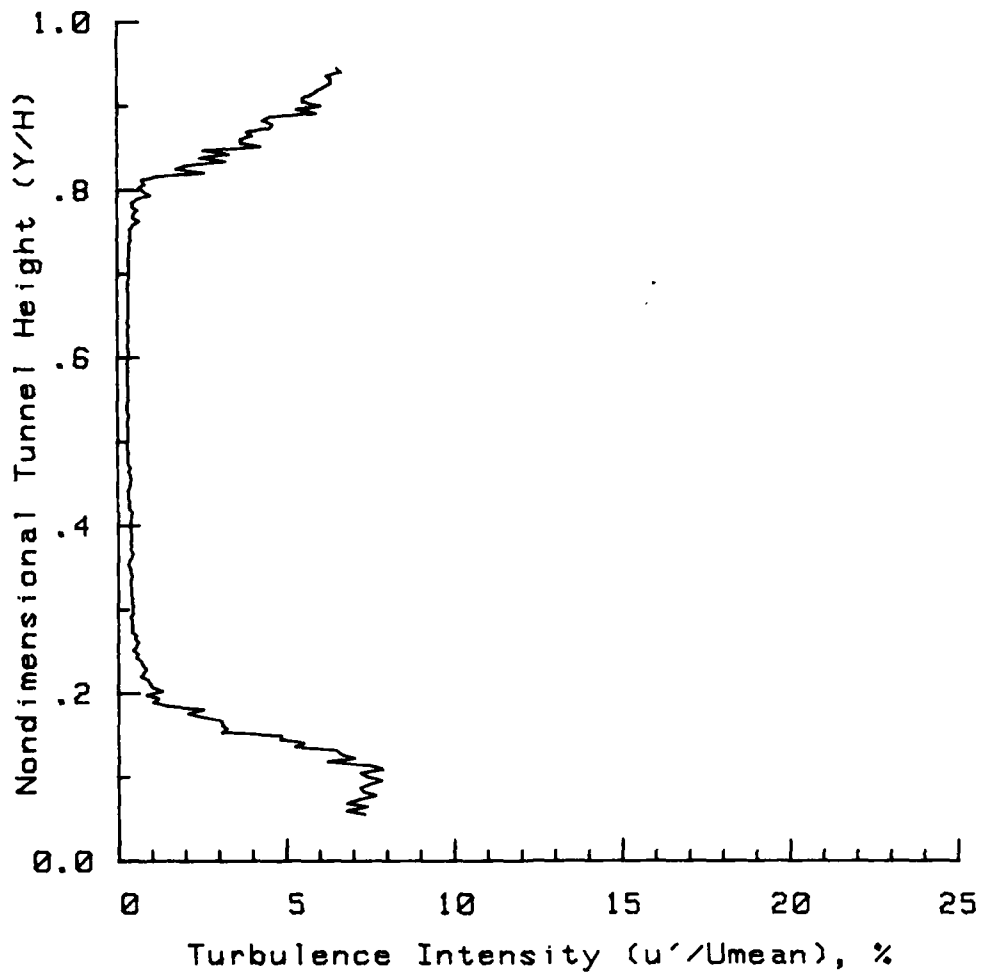


Figure 29. Turbulence Intensity Profile, No Grid, X/H = 3.22

These results agree with McKnight, although McKnight consistently obtained nearly twice the turbulence intensity: "intensity levels up to 16% near the walls." (This author attributes the difference between McKnight's results and the results herein to McKnight's somewhat difficult task in visually reading a fluctuating rms meter. The ADAS ensemble average approach used herein tends to lower rms readings versus a visual approach wherein the researcher tends to respond to the maximum deviation in visual cues. Consequently, differing methodologies in recording data unwittingly magnify slight variations in data.) Figure 29 illustrates the beginning of the growth of the turbulent core characteristic of two dimensional channel flow.

Grid A1.

Figures 30 through 32 present the velocity profile development for this case and Figures 33 through 35 present the corresponding turbulence intensity profile development. These velocity profiles also agree with McKnight and, in general, are smoother.

Grid A3.

Figures 36 through 38 and Figures 39 through 41 show, respectively, the velocity profile development and turbulence intensity profile development for Grid A3. Two of McKnight's results from this grid case apply here: "At $X/H = 1.56$ the velocity profile attains the smoothest and overall closest match with the power law profile. This was anticipated since Hinze (ref. 11) states that 25 to 30 mesh lengths, which

VELOCITY PROFILE

Grid A1

Tunnel heights downstream from grid (X/H) = .44

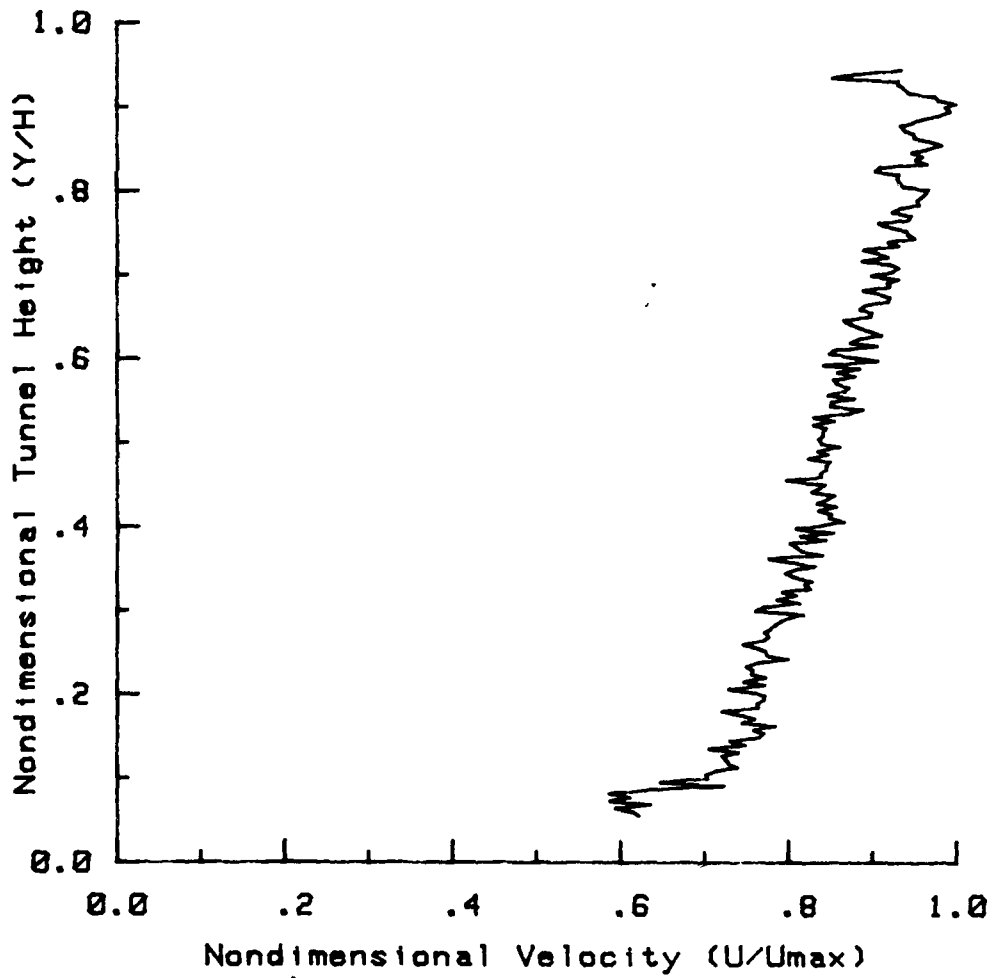


Figure 30. Nondimensional Velocity Profile, Grid A1. X/H = .44

VELOCITY PROFILE

Grid A1

Tunnel heights downstream from grid (X/H) = 1.56

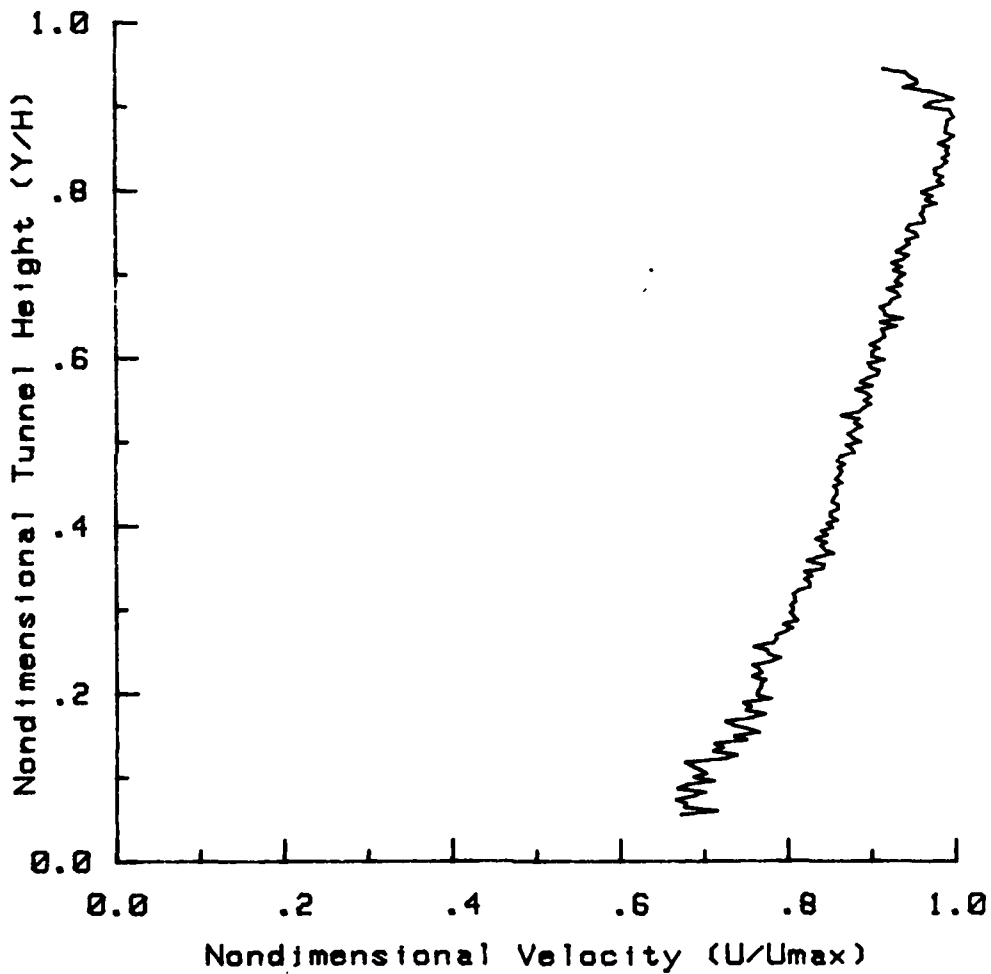


Figure 31. Nondimensional Velocity Profile, Grid A1, X/H = 1.56

VELOCITY PROFILE

Grid A1

Tunnel heights downstream from grid (X/H) = 3.22

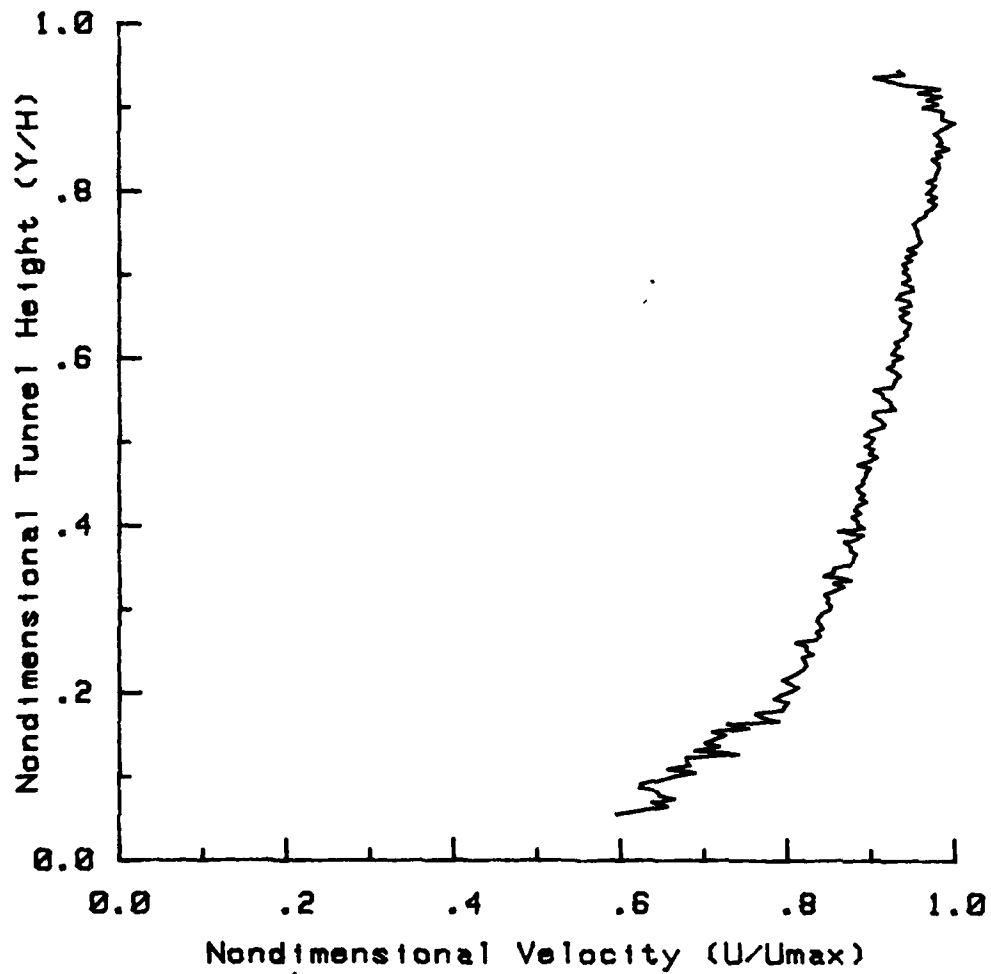


Figure 32. Nondimensional Velocity Profile, Grid A1, X/H = 3.22

TURBULENCE PROFILE

Grid A1

Tunnel heights downstream from grid (X/H) = .44

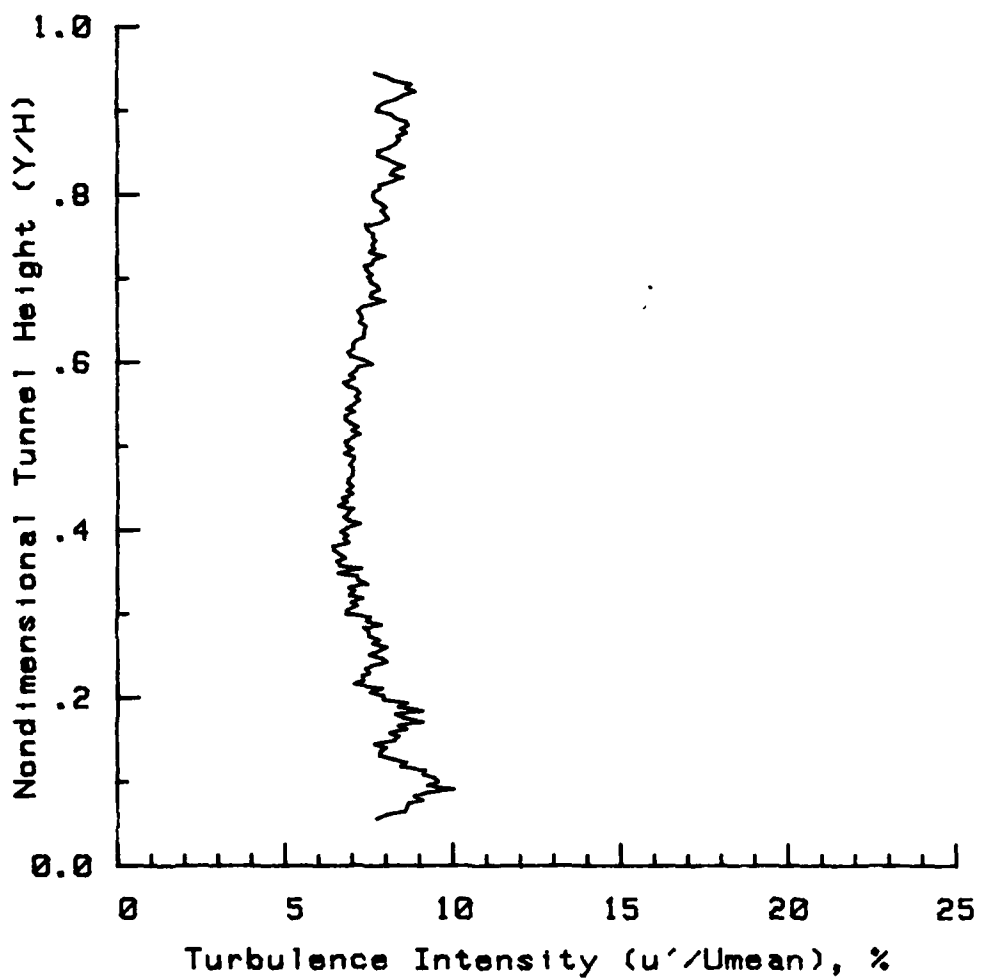


Figure 33. Turbulence Intensity Profile, Grid A1, X/H = .44

TURBULENCE PROFILE

Grid A1

Tunnel heights downstream from grid (X/H) = 1.56

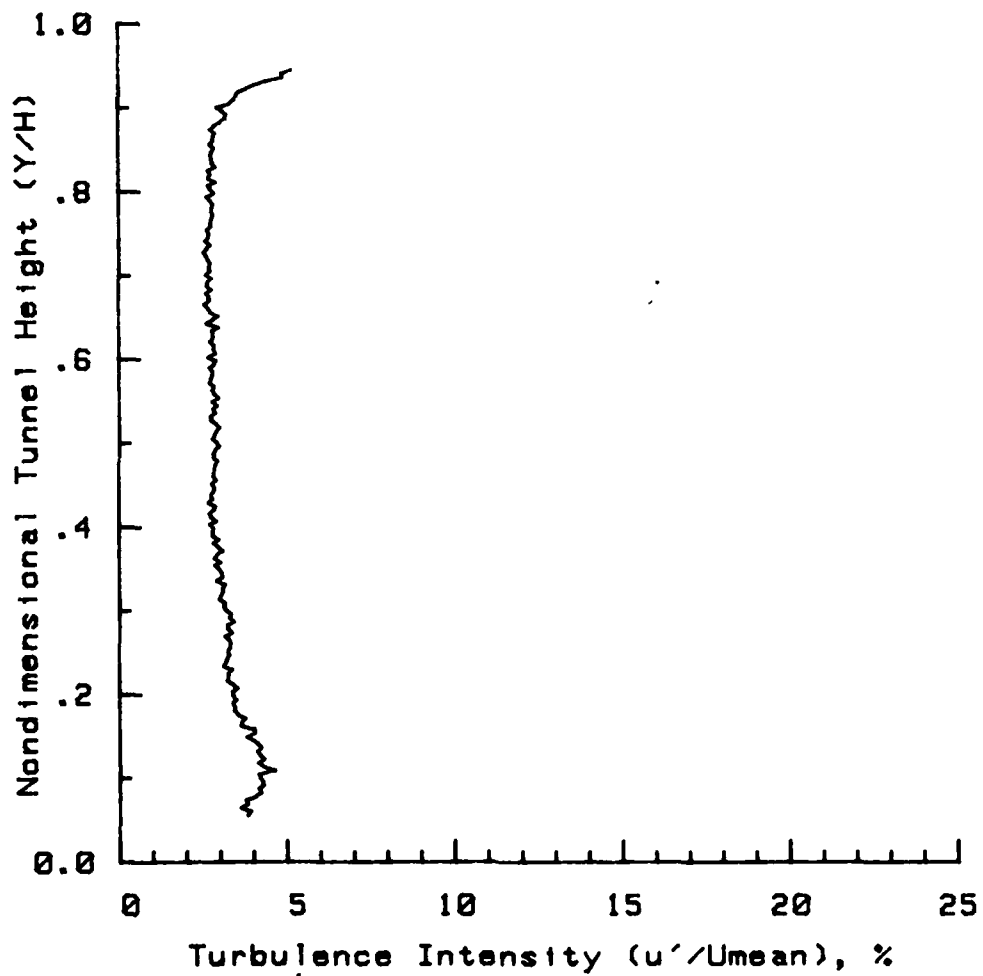


Figure 34. Turbulence Intensity Profile, Grid A1, X/H = 1.56

TURBULENCE PROFILE

Grid A1

Tunnel heights downstream from grid (X/H) = 3.22

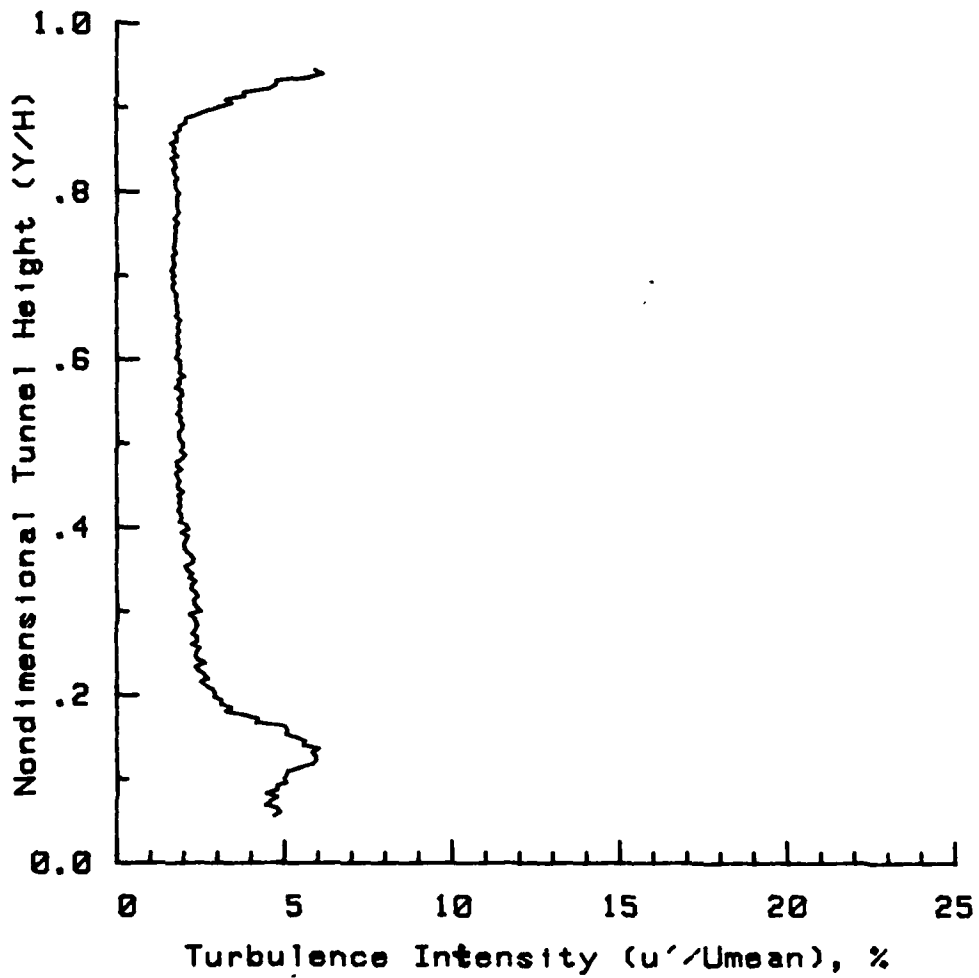


Figure 35. Turbulence Intensity Profile, Grid A1, X/H = 3.22

VELOCITY PROFILE

Grid A3

Tunnel heights downstream from grid (X/H) = .44

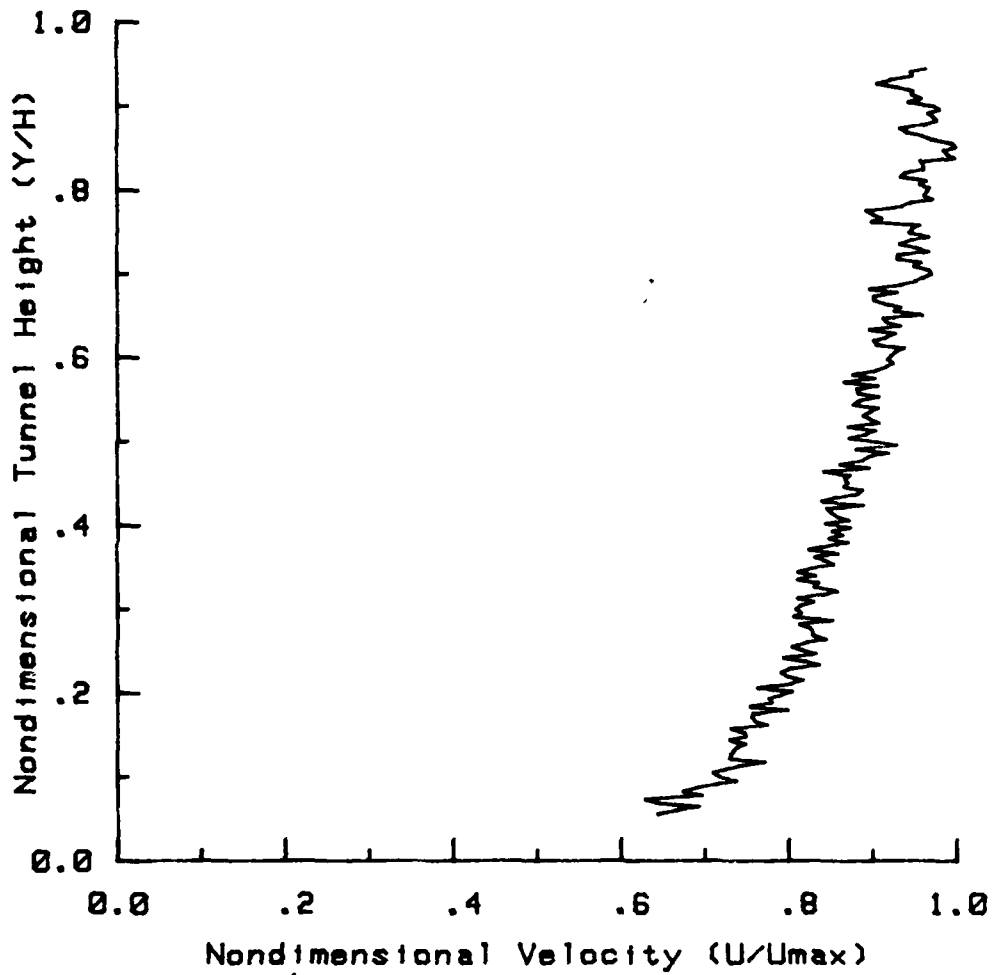


Figure 36. Nondimensional Velocity Profile, Grid A3, X/H = .44

VELOCITY PROFILE

Grid A3

Tunnel heights downstream from grid (X/H) = 1.56

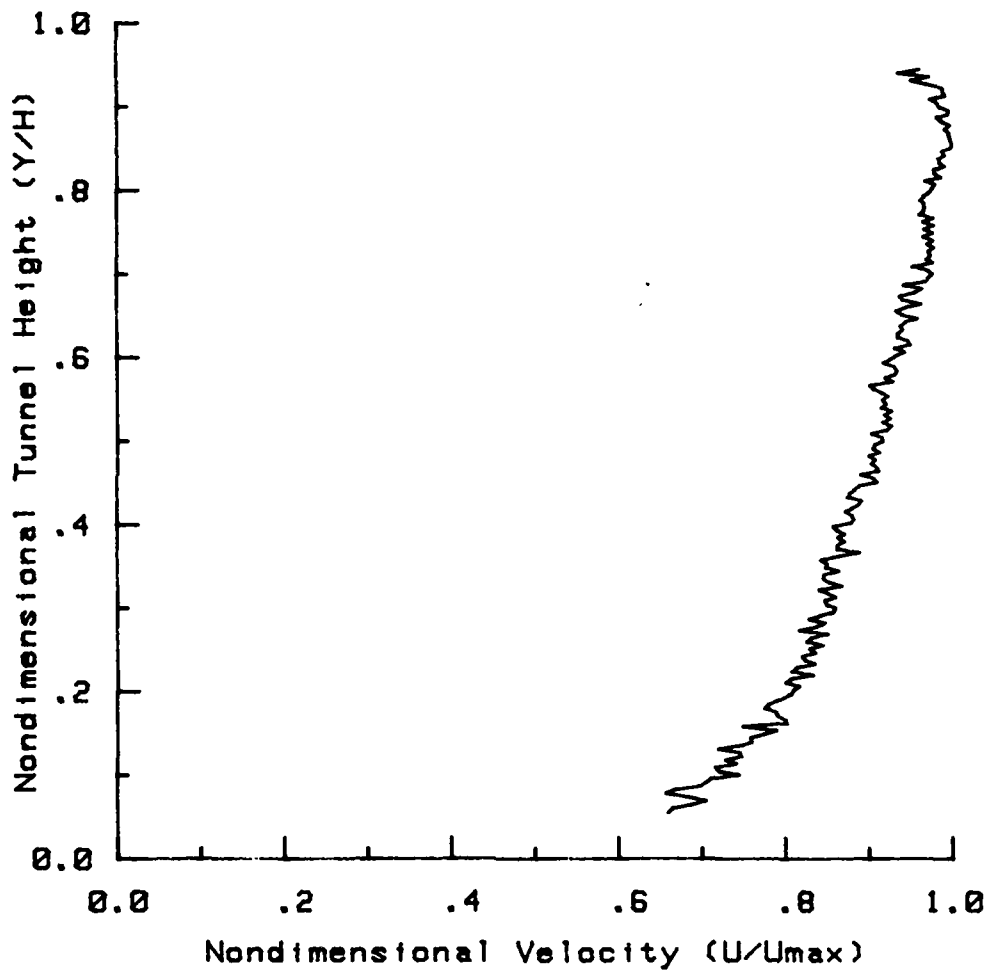


Figure 37. Nondimensional Velocity Profile, Grid A/3, $X/H = 1.56$

VELOCITY PROFILE

Grid A3

Tunnel heights downstream from grid (X/H) = 3.22

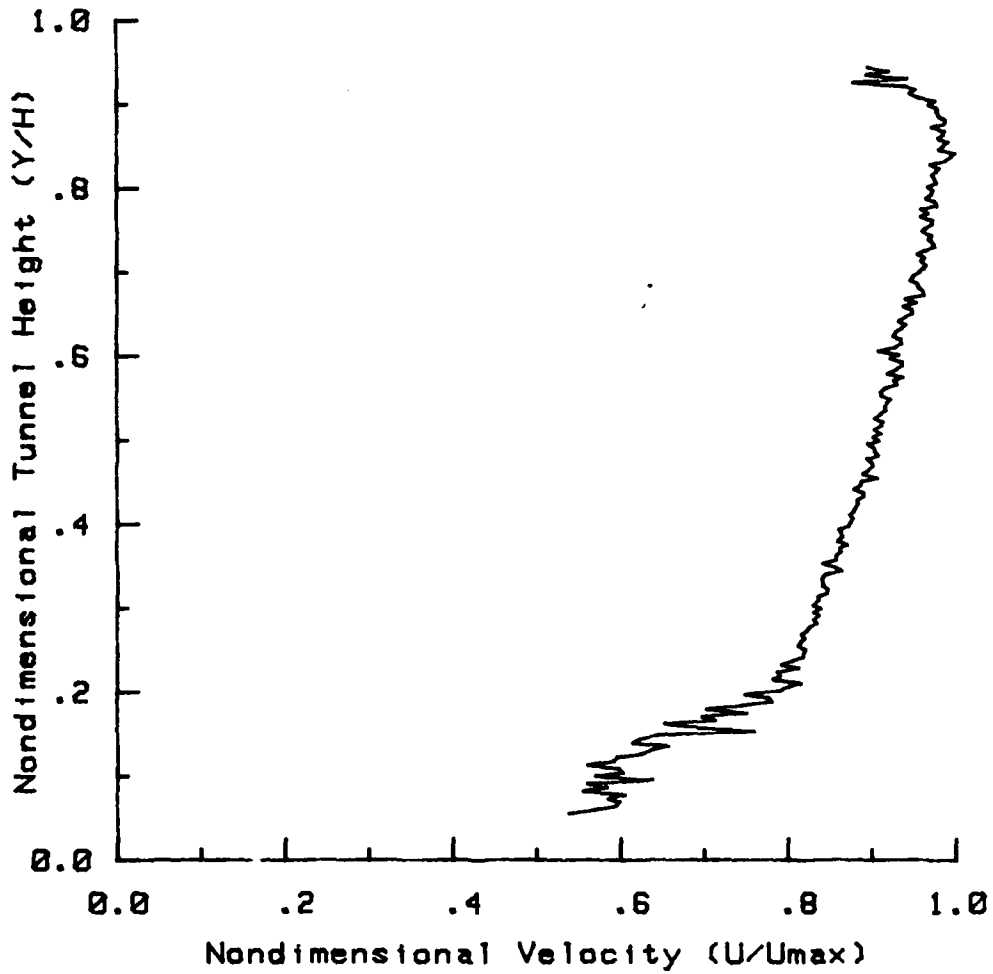


Figure 38. Nondimensional Velocity Profile, Grid A3, X/H = 3.22

TURBULENCE PROFILE

Grid A3

Tunnel heights downstream from grid (X/H) = .44

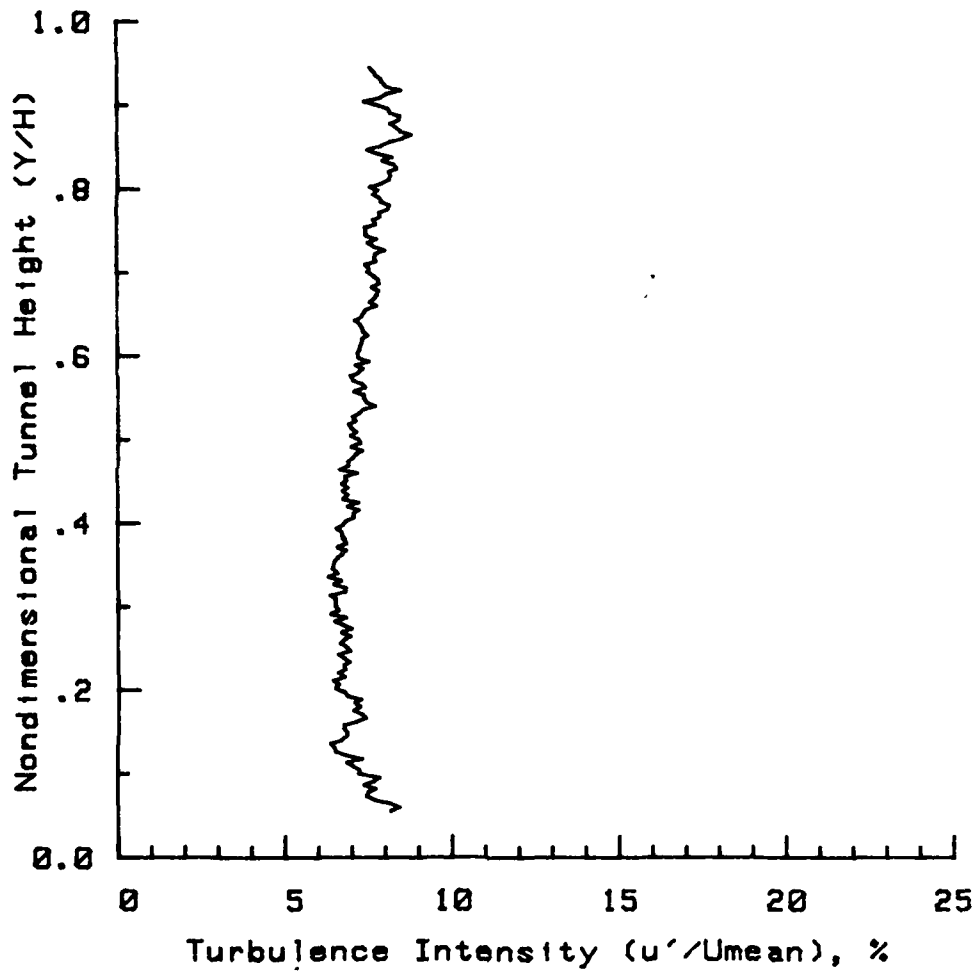


Figure 39. Turbulence Intensity Profile, Grid A3, X/H = .44

TURBULENCE PROFILE

Grid A3

Tunnel heights downstream from grid (X/H) = 1.56

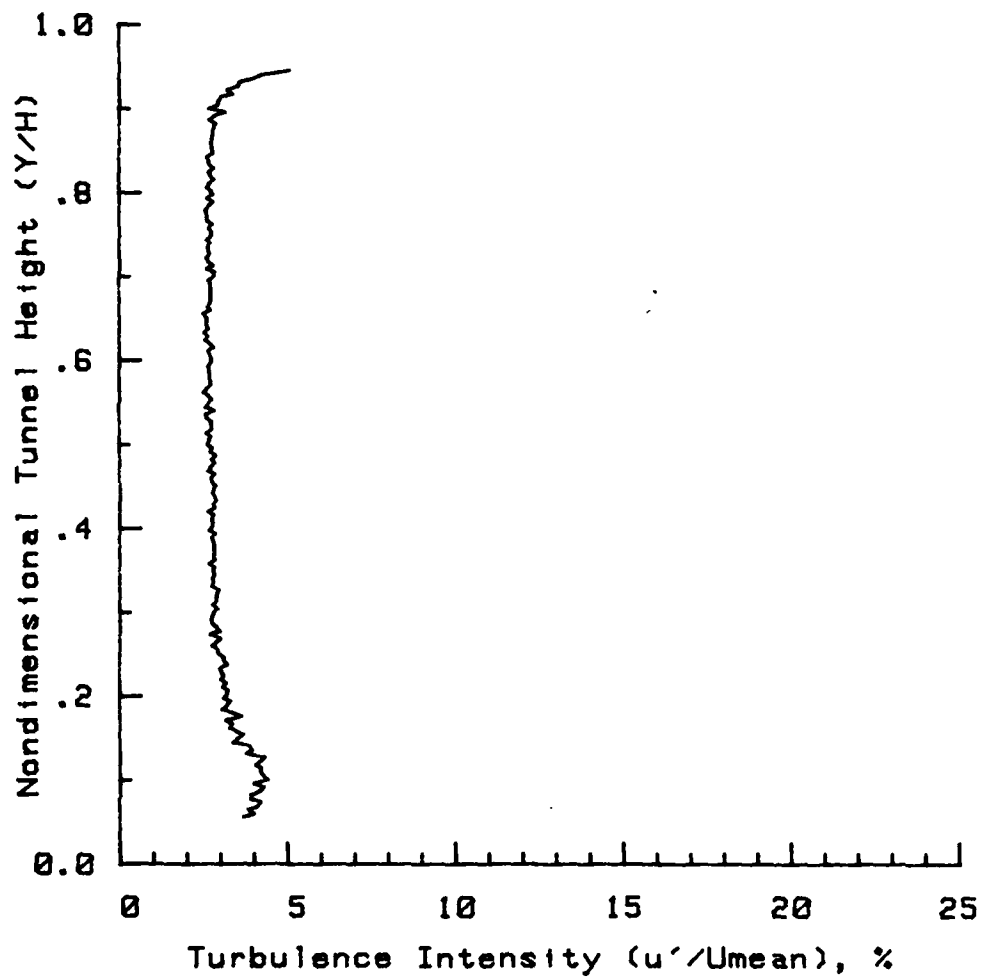


Figure 40. Turbulence Intensity Profile. Grid A3. X/H = 1.56

TURBULENCE PROFILE

Grid A3

Tunnel heights downstream from grid (X/H) = 3.22

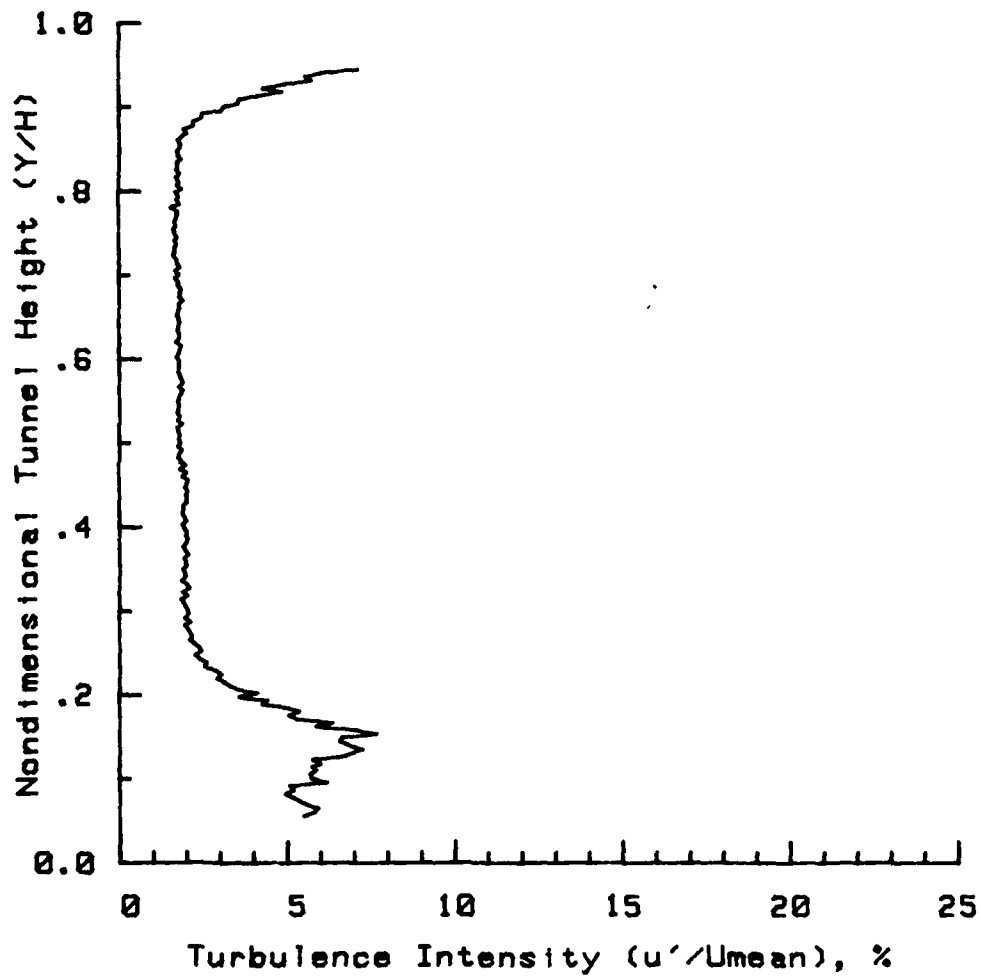


Figure 41. Turbulence Intensity Profile, Grid A3. X/H = 3.22

corresponds to $X/H = 1.56$, was necessary for constancy of the profiles. At $X/H = 3.22$ there is evidence of the velocity profile bulging out to return to the regular profile expected in a two dimensional channel." McKnight bases both of these conclusions on velocity profile data. The added capability here to simultaneously examine turbulence data bears out his results. The turbulence profile at $X/H = 1.56$ is quite smooth outside of the boundary layers. Similarly, the turbulence intensity profile at $X/H = 3.22$ shows little disturbance in most of the free stream where the gradient is slight. But close to the bottom, where the steeper gradient exists because of the grid generated velocity profile, there is a noticeable increase in turbulence level as the flow seeks to return that portion to the profile of regular two dimensional channel flow.

A turbulence decay rate of about $1/2$ here somewhat approximates what McKnight obtained (75%). There does not seem, however, to be a basis for his conclusion that decay rate varies as a function of the rod spacing. (That is, according to McKnight, the decay rate at $Y/H = .78$ should be higher than at $Y/H = .51$ or at $Y/H = .29$.) Consequently, his result: "it is apparent that the closer wake interaction due to the closer rods tends to enable the turbulence intensity to persist at higher levels . . . downstream from the grid," appears unwarranted. Otherwise, the turbulence intensity profile and results contained herein compare favorably with McKnight.

Finally, the results here, too, did not compare with the results of Klebanoff (referenced in McKnight), who artificially generated (by unknown means) a turbulent boundary layer 3.0 inches thick. Klebanoff's results resemble that of Figure 25

VELOCITY PROFILE

Grid B1

Tunnel heights downstream from grid (X/H) = .44

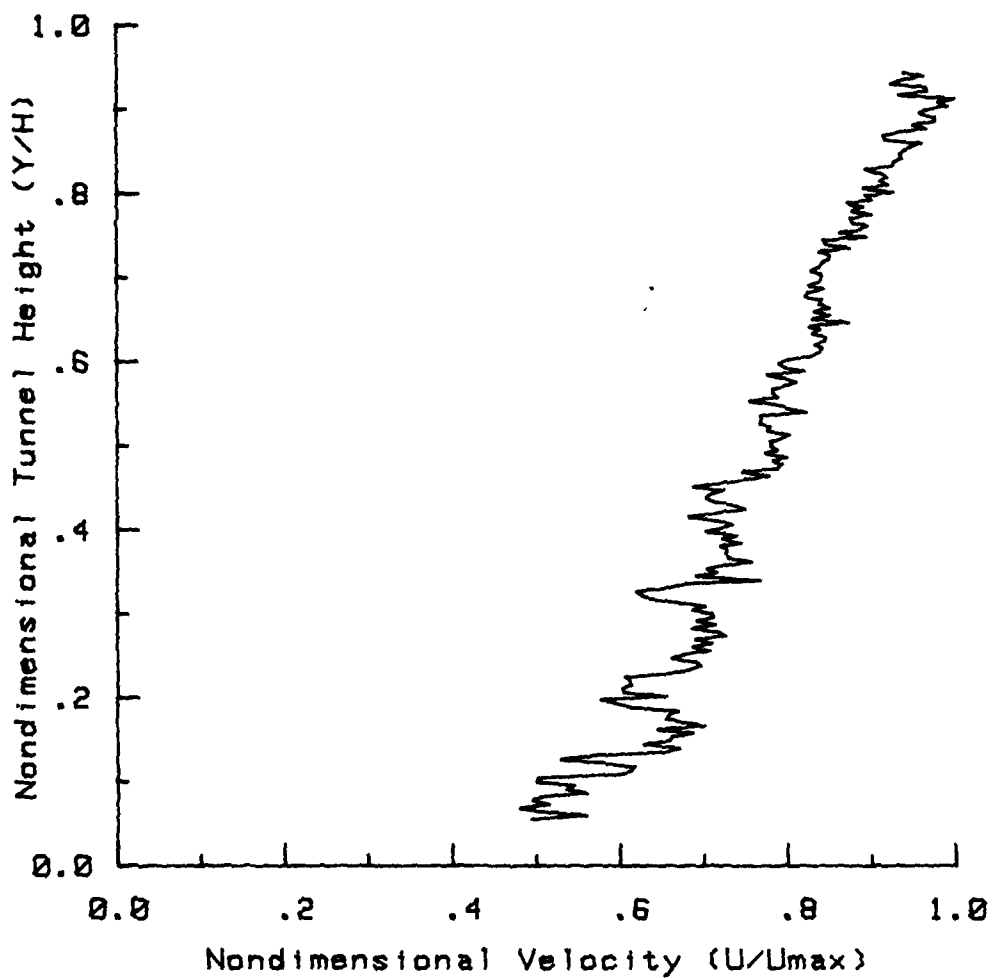


Figure 42. Nondimensional Velocity Profile, Grid B1, X/H = .44

VELOCITY PROFILE

Grid B1

Tunnel heights downstream from grid (X/H) = 1.56

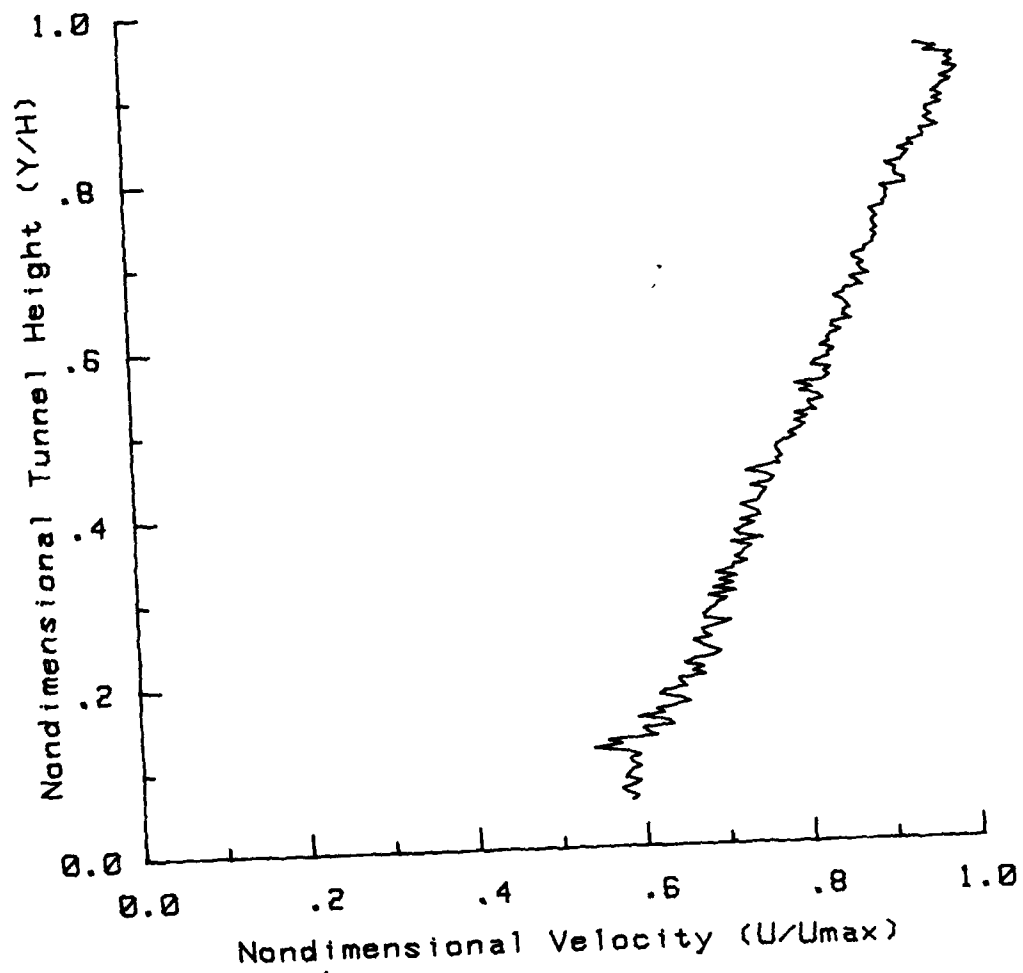


Figure 43. Nondimensional Velocity Profile, Grid B1, X/H = 1.56

VELOCITY PROFILE

Grid B1

Tunnel heights downstream from grid (X/H) = 3.22

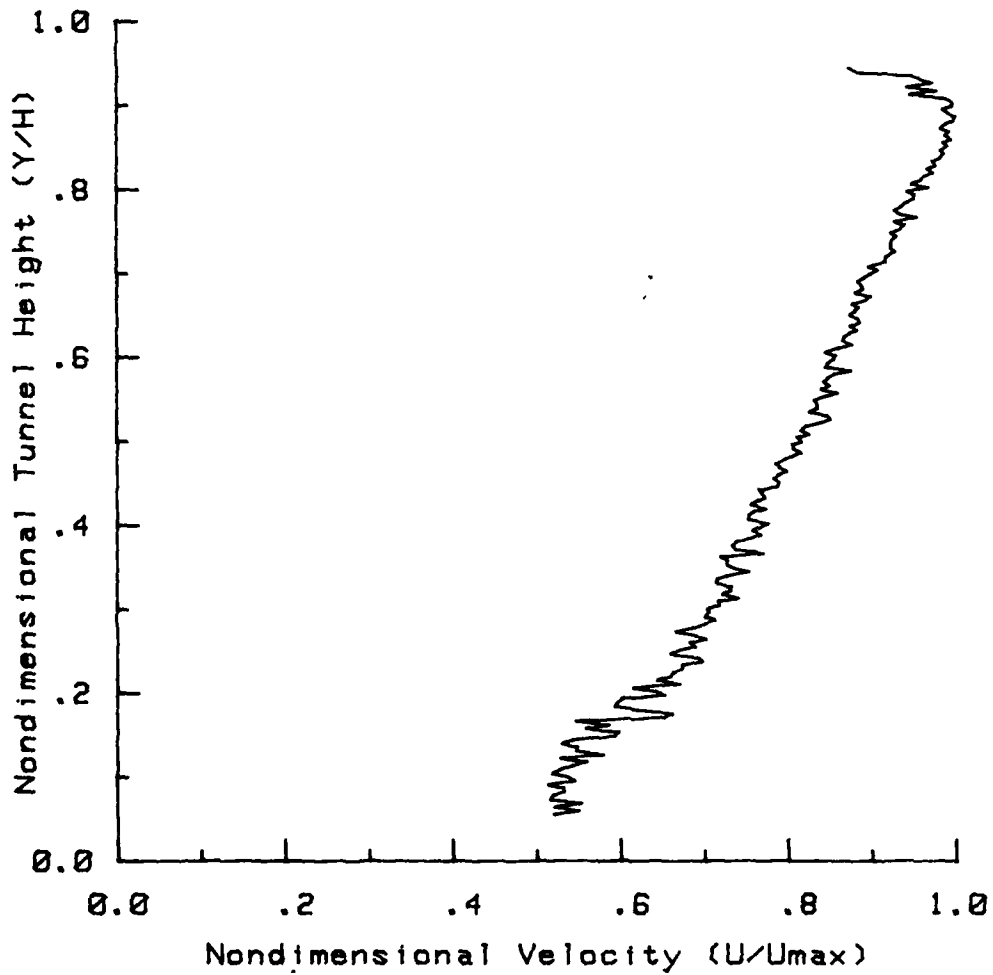


Figure 44. Nondimensional Velocity Profile, Grid B1, $X/H = 3.22$

TURBULENCE PROFILE

Grid B1

Tunnel heights downstream from grid (X/H) = .44

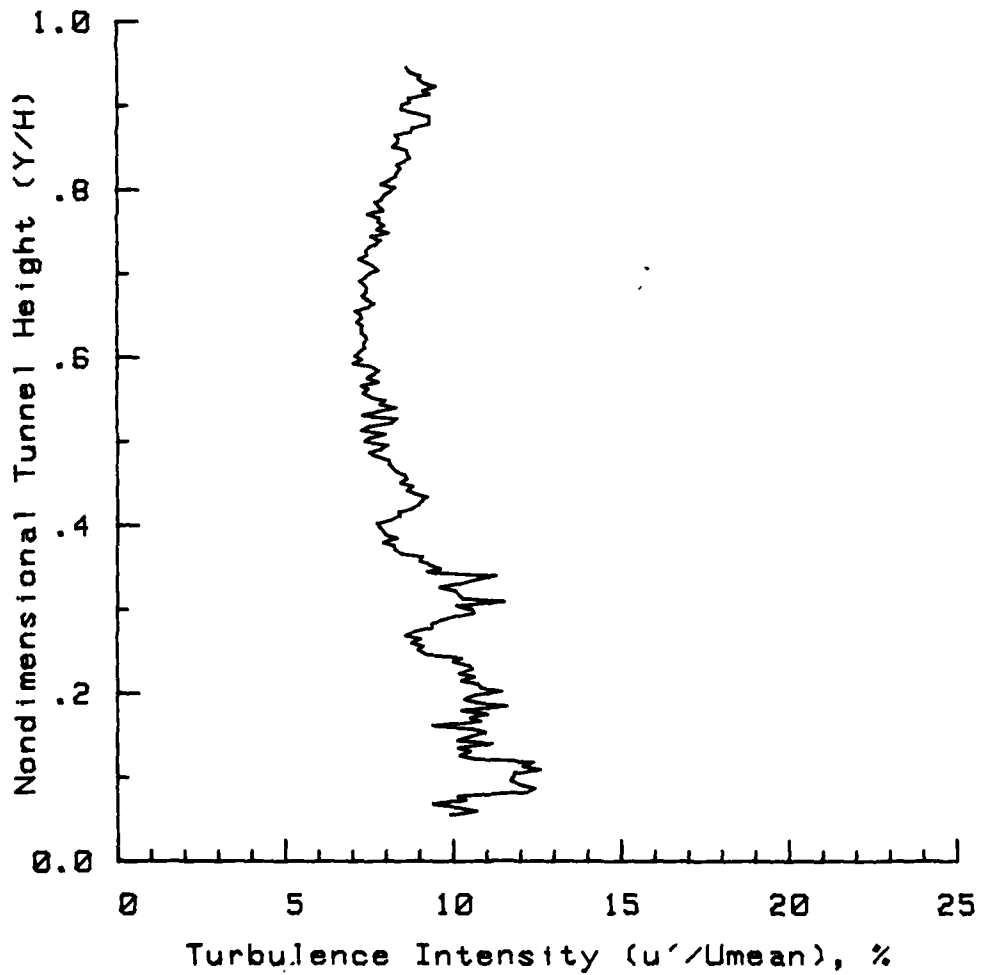


Figure 45. Turbulence Intensity Profile, Grid B1, X/H = .44

TURBULENCE PROFILE

Grid B1

Tunnel heights downstream from grid (X/H) = 1.56

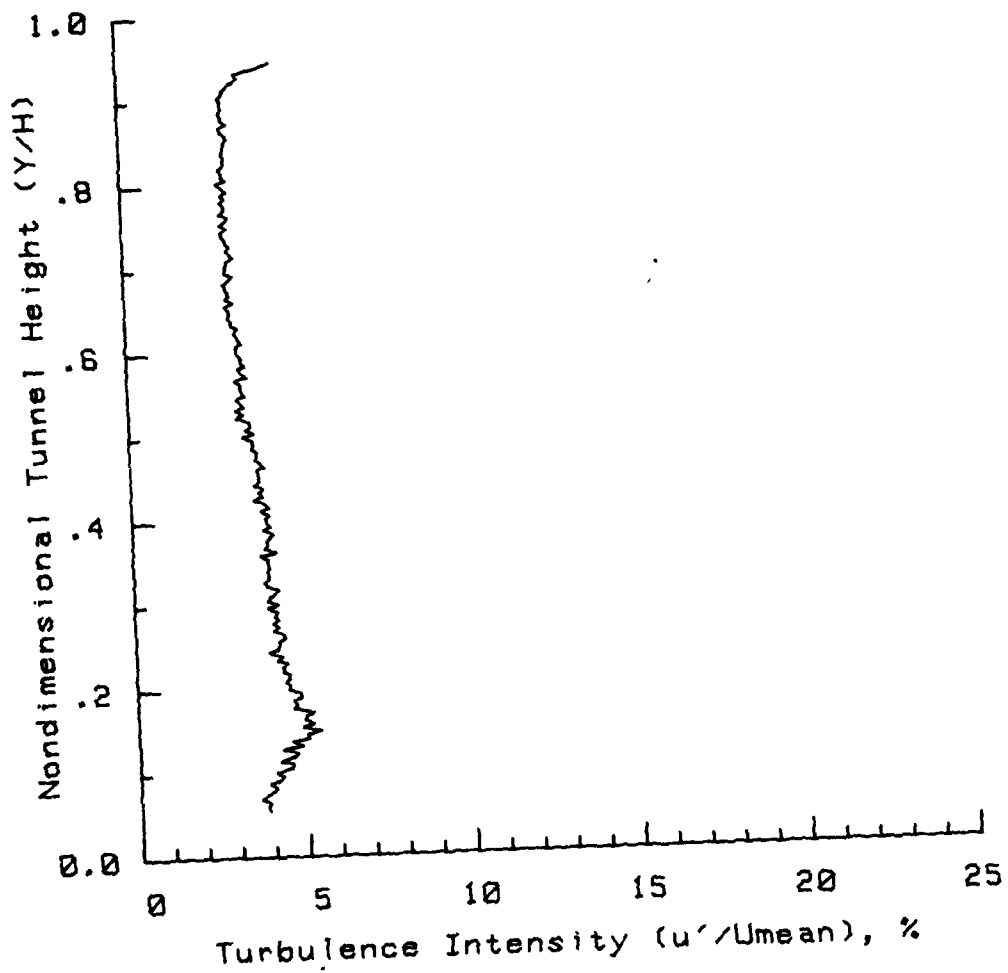


Figure 46. Turbulence Intensity Profile, Grid B1, X/H = 1.56

TURBULENCE PROFILE

Grid B1

Tunnel heights downstream from grid (X/H) = 3.22

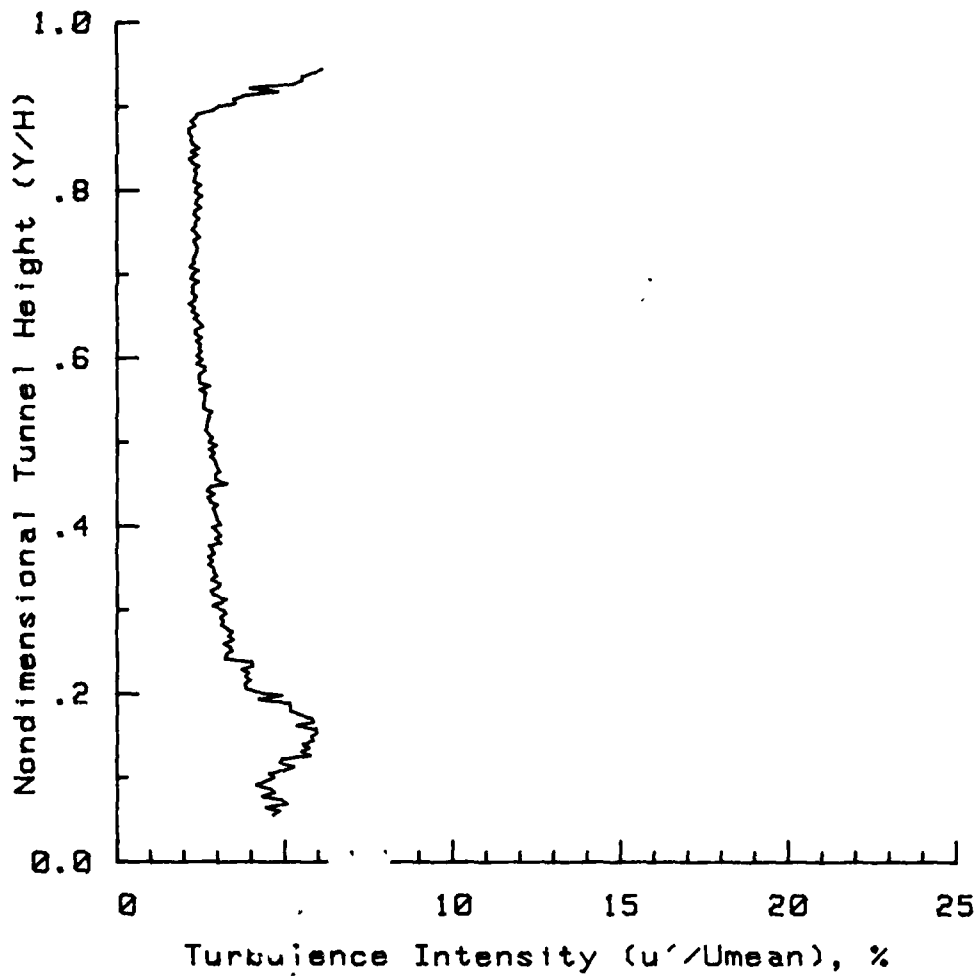


Figure 47. Turbulence Intensity Profile, Grid B1, X/H = 3.22

in the interval $0 < Y/H < .2$.

Grid B1.

Figures 42 through 44 present the velocity profile results of the test run on Grid B1; Figures 45 through 47 present the turbulence intensity profiles for the same case. Both sets of profiles match the results obtained by McKnight: the velocity profiles are nearly linear, with $X/H = 3.22$ coming closest to approximately a one-fourth power law. On the average, the turbulence profiles here are the largest numerically of the three tested grids -- probably due to the added rod packed in the lower portion of the grid. Also, the higher density rod packing in the lower portion of this grid results in significantly higher velocities in portions of the flowfield (Figure 42) by creating the effect of an orifice (U_{max} 's listed in Appendix C).

Cylinder

Figures 48 through 50 present the cylinder's velocity profiles, while Figures 51 through 53 present the corresponding turbulence intensity profiles. The Reynolds number based on cylinder diameter is about 8000 for this set of runs. From the velocity profiles, the velocity distribution in the wake has the gaussian shape. Also, by picking points from the figures, an increase in wake width (i.e. Y/H) is proportional to the root increase in distance ($(X/H)^{1/2}$). Both results agree with Schlichting.

Evaluation

The above results lead to discussion on several points. First, using an ADAS allows much more data to be collected in

VELOCITY PROFILE

Cylinder

Tunnel heights downstream from grid (X/H) = .44

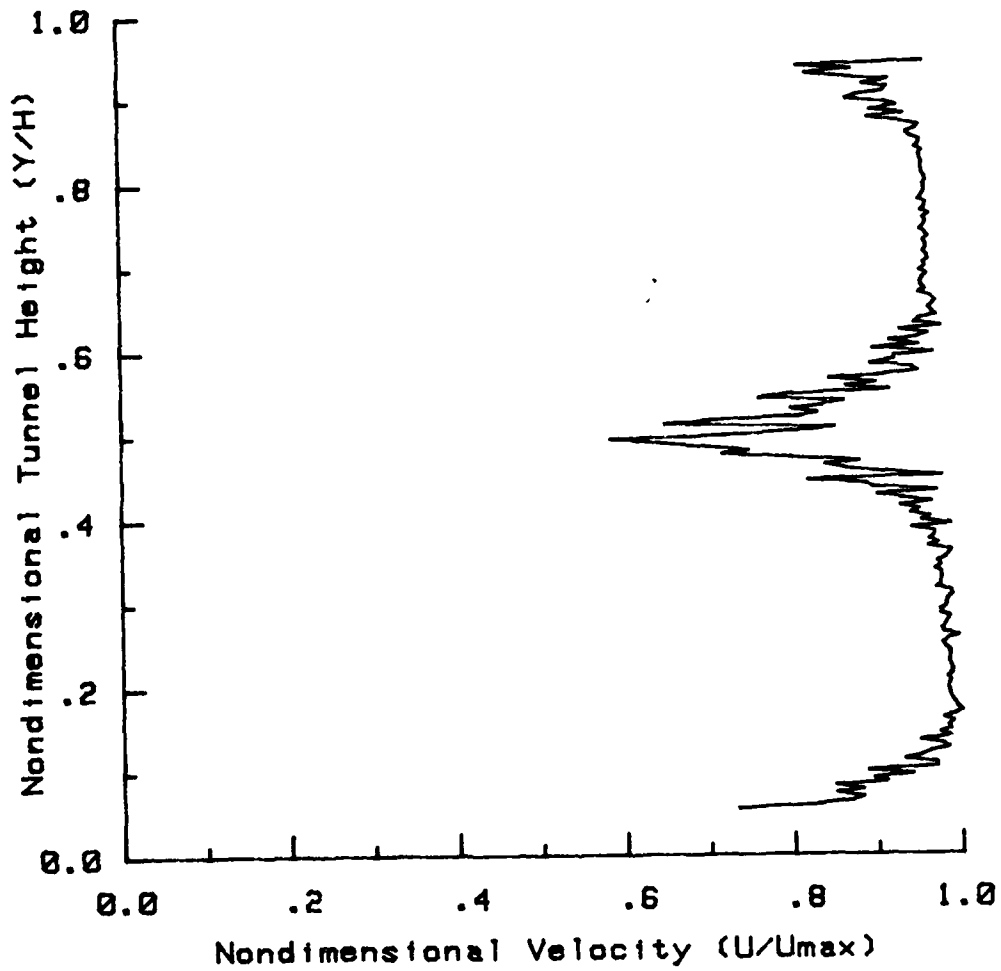


Figure 48. Nondimensional Velocity Profile, Cylinder, X/H = .44

VELOCITY PROFILE

Cylinder

Tunnel heights downstream from grid (X/H) = 1.56

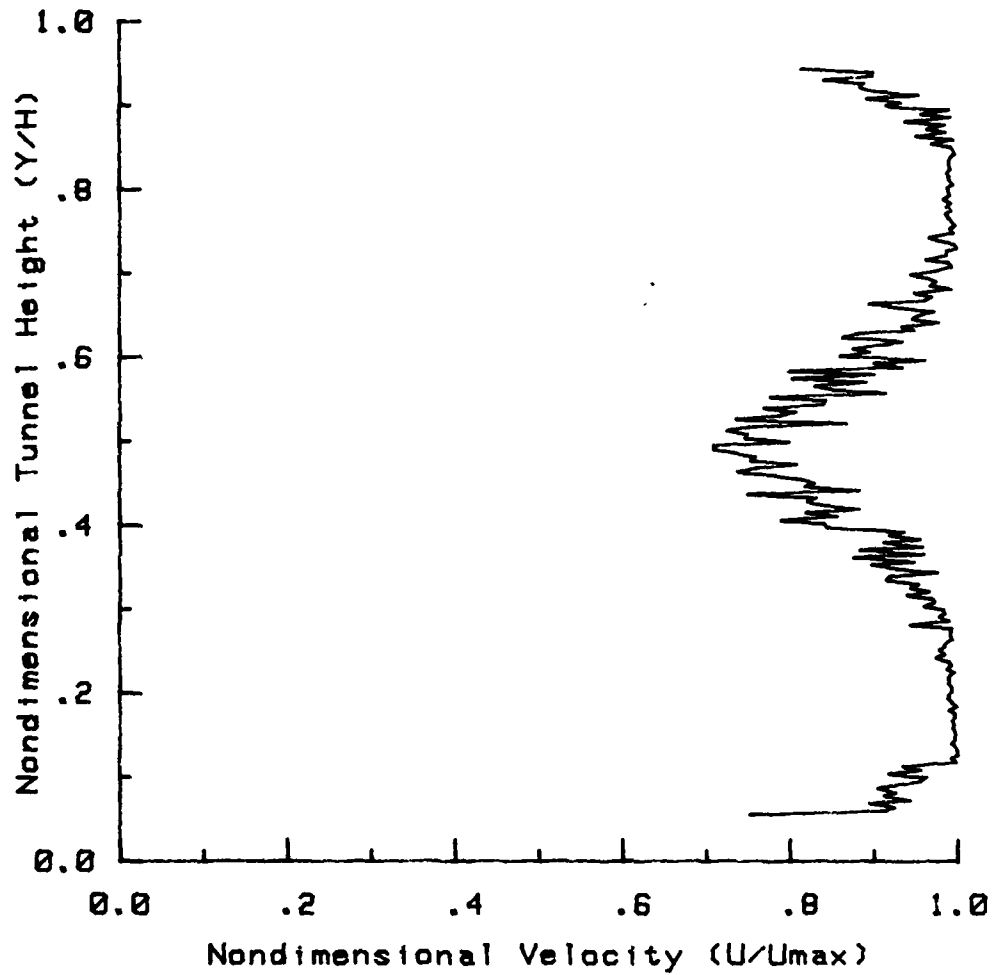


Figure 49. Nondimensional Velocity Profile, Cylinder, $X/H = 1.56$

VELOCITY PROFILE

Cylinder

Tunnel heights downstream from grid (X/H) = 3.22

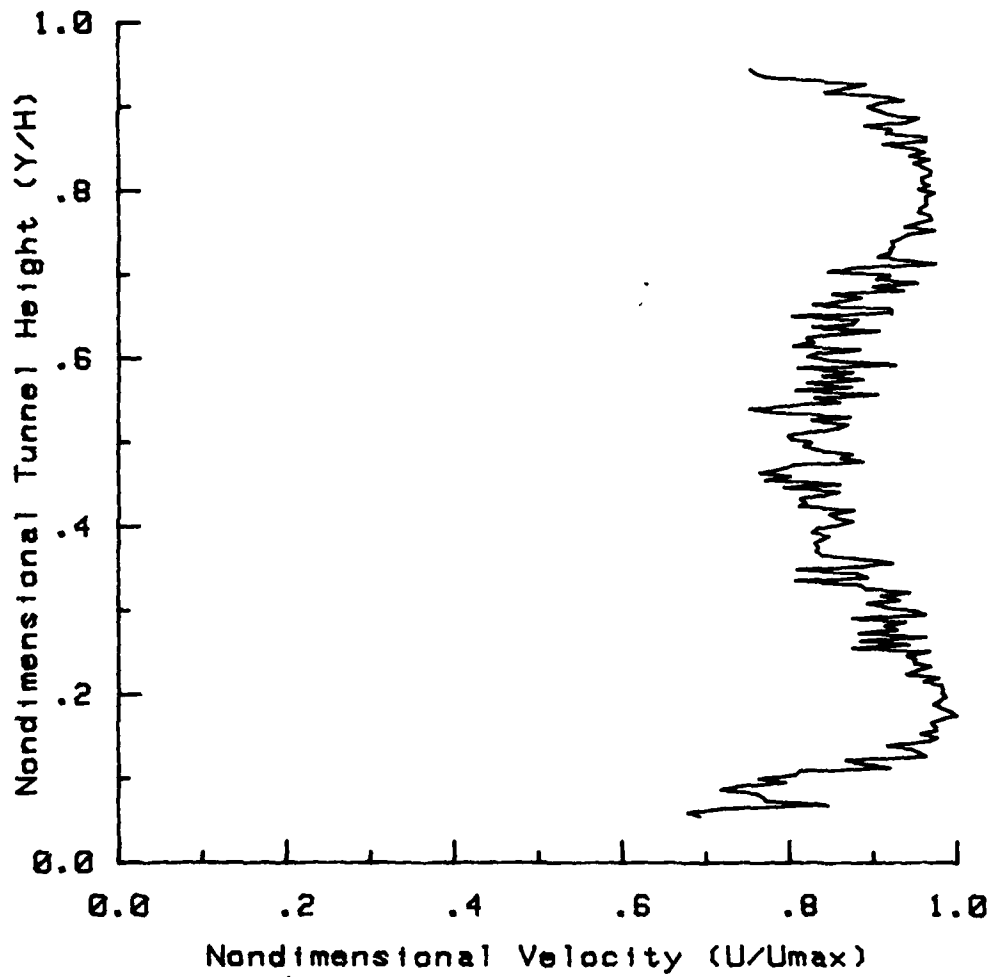


Figure 50. Nondimensional Velocity Profile, Cylinder, $X/H = 3.22$

TURBULENCE PROFILE

Cylinder

Tunnel heights downstream from grid (X/H) = .44

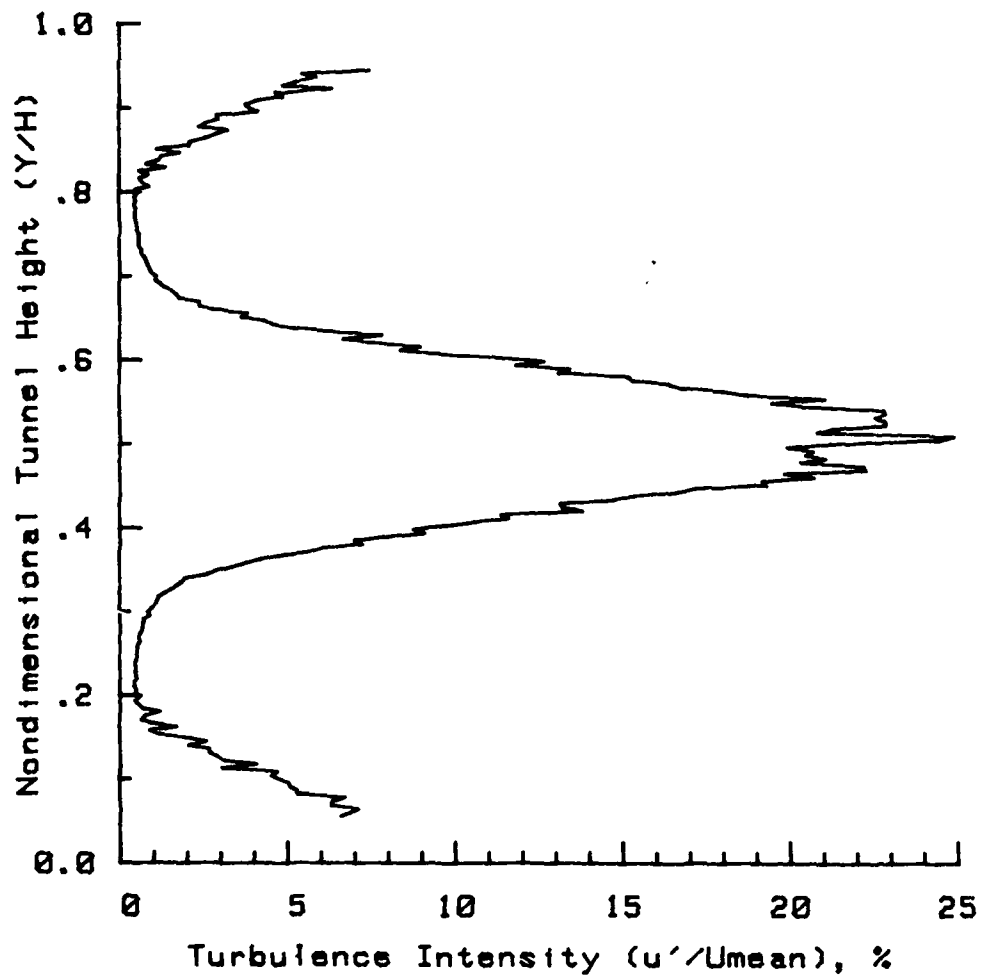


Figure 51. Turbulence Intensity Profile, Cylinder, X/H = .44

TURBULENCE PROFILE

Cylinder

Tunnel heights downstream from grid (X/H) = 1.56

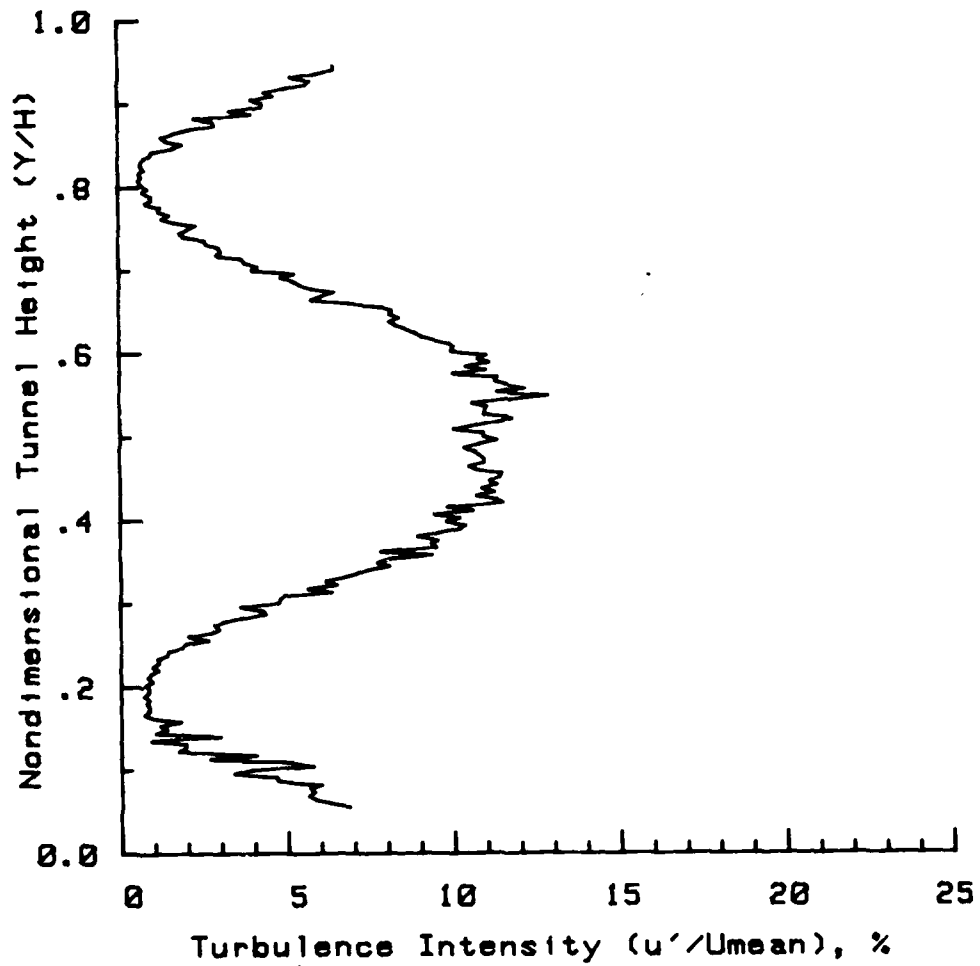


Figure 52. Turbulence Intensity Profile, Cylinder, X/H = 1.56

TURBULENCE PROFILE

Cylinder

Tunnel heights downstream from grid (X/H) = 3.22

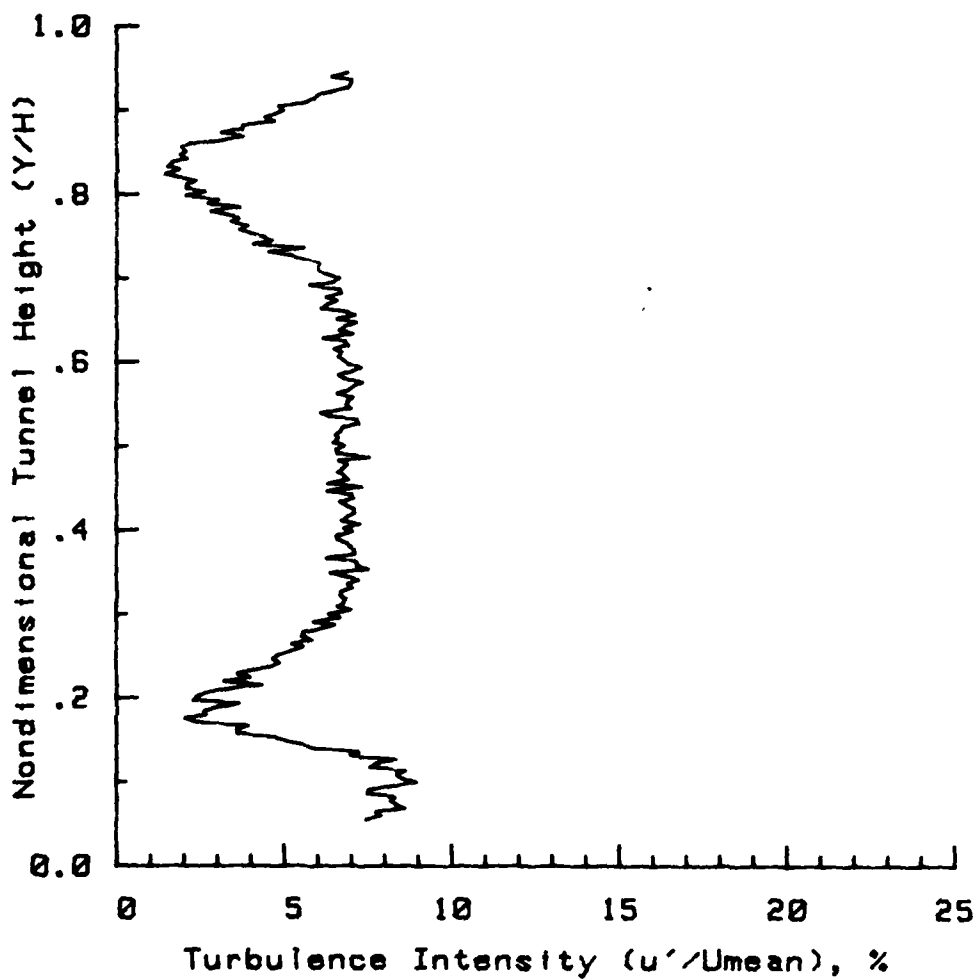


Figure 53. Turbulence Intensity Profile, Cylinder, X/H = 3.22

a given period of time than by using hand collection methods. That both methods yield the same profiles indicates the advantage to be gained by employing an automated system. Other than the small difference noted above in the turbulence intensities, all the data taken by either method show the same amount of scatter. For example in the hand collected data, variations from the average amount to no more than the fluctuating values recorded on the graphs by the ADAS.

The data here warrant McKnight's conclusion that "a stable power-law profile may be generated with negligible diffusion of the shear layer through the length of the test section" But by examining the turbulence intensity profiles, one sees that the larger shear layer near the bottom of the profile tends to increase (through the rear half of the test cabin) the rather smooth turbulence intensity levels immediately proceeding. So depending on the criteria, the velocity profiles may in fact not be stable.

The velocity and turbulence intensity profiles for the cylinder indicate quite a large local variation: are such profiles stable? Intuitively, the profiles appear gaussian and can lend themselves to numerical integration for answers to classical questions like the drag on the cylinder. However, in this case Schlichting notes that "extensive experiments . . . in the wake of a cylinder and which were concerned with turbulent fluctuations at Reynolds numbers near 8000, showed that at a distance equal to about 160 to 180 diameters the turbulent microstructure is not yet fully developed." 160 diameters corresponds to 80 inches -- well beyond the 30 inch

test cabin length. For comparison, results on the grids, where 160 diameters corresponds to 20 inches, show that the turbulence intensity at 14 inches (the closest to 20 inches of the three readings) yields a relatively smooth curve vis-à-vis the other two curves in each set.

The results indicate that while the low speed wind tunnel can illustrate well velocity profiles of a given nature, the low speed wind tunnel cannot adequately test for turbulence microstructure on models larger than about 0.2 inches in cross-section.

Also from a comparison of figures, one realizes that none of the turbulence intensity profiles of a particular grid match those of a boundary layer -- see, for example, the no grid results in the region $0 < Y/H < .2$. These profiles then should not be construed as turbulent boundary layer profiles, even though the profile is modeled to give the same velocity distribution.

VI. Conclusions and Recommendations

This study evaluated one method of automating the data acquisition and data processing for AFIT's low speed wind tunnel. To measure the data from the tunnel, the experimental equipment included a hot wire (film) anemometer system, an automatic data acquisition system, and a stepper motor driven traversing mechanism made for this project. On the basis of the results presented in Chapter V and obtained by the experimental equipment, the following conclusions are drawn:

1. Considering the large quantities of data to be processed, the use of on-line processing of data and of computer control of the anemometer provides increased flexibility in data collection and in data reduction. Also, the stepper motor fits quite well into the scheme of the sensitive measurement systems which require the service of a general purpose ADAS.

2. Data obtained with the automated data collection/reduction scheme confirms that stable velocity profiles and turbulence intensity profiles can be generated in the test cabin of the low speed wind tunnel. However, because of the length of the test cabin, scale problems will occur when trying to measure stable turbulent microstructure with models larger than approximately 0.2 inches in diameter. Also, this scheme confirms that such velocity profiles will exhibit negligible diffusion of the shear layer through the length of the test cabin. But these profiles have turbulence intensity profiles uncharacteristic of a boundary layer.

3. With an ADAS's capabilities, whether viewing the overall picture, comparing to other research work, or analyzing sets of runs, all the data collection and reduction tasks become much easier.

4. The calibration of the sensor for the range of velocities of interest was best accomplished by using the ADAS-based procedure discussed in Appendix B and in Kirchner (ref. 14).

Based upon the observations made during this investigation, the following recommendations are made:

1. In a paper on freestream turbulence influence on boundary layers, Meier and Kreplin (ref. 15) conclude that "different grid dimensions and positions generate turbulence of completely different spectra, even if the turbulence intensity is not changed. Thus in existing wind tunnels with the same turbulence intensity, different screens and/or honeycombs can imply different turbulence structures." With the capability existing now as a result of this project, this author recommends investigating these implications in the low speed wind tunnel.

2. To maintain a constant velocity through the test cabin, the induction fan motor must vary speeds as the pressure fluctuates in the room. This fluctuation will occur most often because the hallway pressure changes -- although slow variations in the motor speed, in the barometer, or in the room temperature can all also influence velocity. Therefore, to maintain constant test conditions, work is needed on an automatic monitoring/feedback control system tied to the ADAS for the test cabin. Pressure transducers and thermocouples are available to monitor the system. To control the motor, recommend the following package for augmentation to the system: 1) an SCR controller for

use with series wound DC motors (as exists here), ii) two DPST (double pole single throw) enclosed contactors to switch the motor on and off, iii) a digital to analog converter with transistor amplification to convert the ADAS's pulses to a form useable by the controller.

3. To measure the tunnel flow's Reynolds stress without changing probes, this author recommends modifying the traversing mechanism to measure Reynolds stress by using a single rotated inclined hot wire anemometer. Fujita and Kovasznay (ref. 7) note that "when only the second moments of the turbulent velocity fluctuations ($\overline{u'^2}$, $\overline{v'^2}$, $\overline{u'v'}$) need be measured, a single wire suffices." They indicate that this method provides good agreement and a convenient approach.

4. Recommend that this traversing mechanism, in conjunction with another fixed (from below) probe, be used in a flow field study of large period vibrations/oscillations movement superimposed on the grid generated fluid flow field.

5. Recommend that Neyland's work (ref. 20) on ADAS graphical representation of airfoil data be used in conjunction with a wind tunnel study of selected airfoil shapes. His work allows the ADAS (through the plotter) to present the data by drawing the test cabin and airfoil and then locating the data points accordingly.

Bibliography

1. Bendat, J. S. and A. G. Piersol. Engineering Applications of Correlation and Spectral Analysis. New York, New York: John Wiley & Sons, Inc., 1980.
2. Bendat, J. S. and A. G. Piersol. Random Data: Analysis and Measurement Procedures. New York, New York: John Wiley & Sons, Inc., 1971.
3. Bradshaw, P. An Introduction to Turbulence and Its Measurement. Oxford, England: Pergamon Press, Ltd., 1971.
4. Bradshaw, P. Experimental Fluid Mechanics. Oxford, England: Pergamon Press, Ltd., 1964.
5. Cockrell, D. J. and B. E. Lee, "Production of Shear Profiles in a Wind Tunnel by Cylindrical Rods Placed Normal to the Stream," Journal of the Royal Aeronautical Society, 70: 724-725 (1966).
6. Dickens, K. J. and D. C. DeRusha. "Using a Microcomputer to Control and Log Data from a Spectrometer," Proceedings of the Sixth Annual Symposium on Incremental Motion Control Systems and Devices, ed., B.C. Kuo.; 389-397. Urbana, Illinois: Department of Electrical Engineering, University of Illinois at Urbana-Champaign, May, 1977.
7. Fujita, H. and L. S. G. Kouaszny. "Measurement of Reynolds Stress by a Single Rotated Hot Wire Anemometer," The Review of Scientific Instruments, 39 (9): 1351-1355 (September, 1968).
8. Gravin, Meisner and Todd. The Robot Users Manual. Project work under the direction of Dr. Hartrum, Department of Electrical Engineering, School of Engineering, Air Force Institute of Technology, Wright-Patterson Air Force Base, Ohio, March, 1980.
9. Department of Aeronautics and Astronautics, Air Force Institute of Technology, Wright-Patterson Air Force Base, Ohio; Curricula Catalog, 1981.
10. Hewlett Packard Model 3052A (9845B) Automatic Data Acquisition System Package Library. Loveland, Colorado: Hewlett Packard Company, 1978.
11. Hinze, J. O. Turbulence, An Introduction to Its Mechanism and Theory. New York: McGraw-Hill Book Company, Inc.,

12. Hot Film and Hot Wire Anemometry, Theory and Application, Bulletin TB5. Saint Paul, Minnesota: Thermo-Systems, Inc. Instrumentation Systems, Inc. (Vendor), Dayton, Ohio, undated.
13. Kareem, A. and J. E. Cermak. "Wind Tunnel Simulation of Wind-Structure Interactions," Proceedings of the Twenty-Fourth International Instrumentation Symposium (jointly subtitled: Instrumentation in the Aerospace Industry - Volume 24 and Advances in Test Measurement - Volume 15), ed., K. E. Kissell. 343-362. Pittsburgh, Pennsylvania: Instrument Society of America, May, 1978.
14. Kirchner, M. J. Computer Assisted Velocity and Turbulence Measurements in a Plane Free Jet at High Subsonic Speeds. M.S. thesis. Wright-Patterson Air Force Base, Ohio: School of Engineering, Air Force Institute of Technology, December, 1981.
15. McKnight, T. N. Turbulent Shear Flow Velocity Profiles Behind a Grid of Parallel Rods of Variable Spacing. M.S. thesis, Wright-Patterson Air Force Base, Ohio: School of Engineering, Air Force Institute of Technology, December, 1980.
16. Meier, H. U. and H.-P. Kreplin. "Influence of Freestream Turbulence on Boundary Layer Development," AIAA Journal, 18 (1): 11-15 (January, 1980).
17. Mechanical Components, Product Catalog. Quincy, Massachusetts. Boston Gear Division, Incom International, Inc. Transmission, Inc. (vendor), Dayton, Ohio, 1979.
18. Motiwalla, S. "Continuous Patch Control of Stepper Motors," Robotics Age, 3 (4): 28-36 (July/August, 1981).
19. Motiwalla, S. and R. Tseng. "Continuous Path Control with Stepping Motors," Robotics Age, 3 (5): 16-21 (September/October, 1981).
20. Neyland, D. C. Hardware and Software Integration for Concurrent Data Acquisition and Reduction of Photon Correlated Laser Doppler Velocimetry. M.S. thesis, Wright-Patterson Air Force Base, Ohio: School of Engineering, Air Force Institute of Technology, December, 1981.
21. Peterson, C. W. "A Survey of the Utilitarian Aspects of Advanced Flowfield Diagnostic Techniques," American Institute of Aeronautics and Astronautics, Journal, 17 (12): 1352-1360 (December, 1979).
22. Schlichting, H. Boundary Layer Theory. New York, New York: McGraw-Hill Book Company, Inc., 1979.

23. Stepper Motor Handbook. Product Catalog. Cheshire, Connecticut: North American Philips Controls Corporation. C. A. Robinson Company, Inc. (vendor), Dayton, Ohio, undated.
24. Tal, J. and E. K. Persson. "Microprocessor-Controlled Incremental Motion Servo Systems," Proceedings of the Sixth Annual Symposium on Incremental Motion Control Systems and Devices, ed., B. C. Kuo.; 153-161. Urbana, Illinois: Department of Electrical Engineering, University of Illinois at Urbana-Champaign, May, 1977.
25. Thermo-Systems, Inc. Operating and Service Manual for 1050 Series Constant Temperature Anemometers and Related Accessories. St. Paul, Minnesota: Thermo-Systems, Inc., undated.
26. Vonada, J. A. Wake Mixing Investigation of Crenelated Vane Trailing Edges. Ph.D dissertation proposal, Wright-Patterson Air Force Base, Ohio: School of Engineering, Air Force Institute of Technology, April, 1981.
27. Zakanycz, S. Turbulence and the Mixing of Binary Gases. Ph.D dissertation. Columbus, Ohio: Ohio State University, 1971.

Appendix A: Stepper Motor Manufacturer's Data

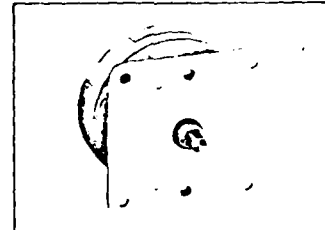
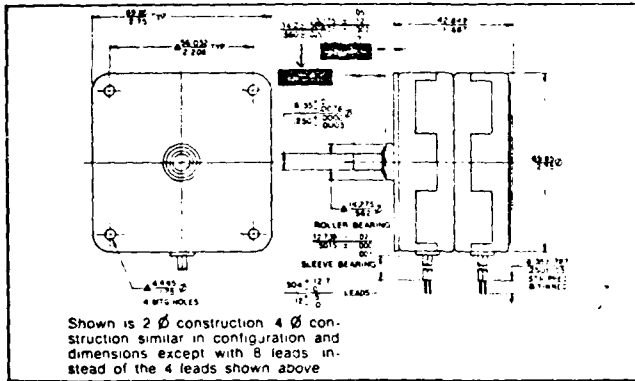
North American Philips Controls Corporation, Cheshire, Conn.

Step Angle*	Pull-out Rate*	Power Consumption*
7.5°	360 s/s	12W
15°	200 s/s	12W

*For 2-phase construction See Specification Chart for 4-phase construction

Stepper Motors Series 82900

OUTLINE AND MOUNTING DIMENSIONS: MM/INCHES
Symbol $\Delta \pm .27/\pm .005$ Unspecified $\pm .78/\pm .031$



The 82900 stepper is a 12W bi-directional motor which combines high torque and low cost with a small, compact motor package. Its small size and excellent performance characteristics allow it to be used as a money-saving replacement for larger, more expensive steppers in a wide range of applications.

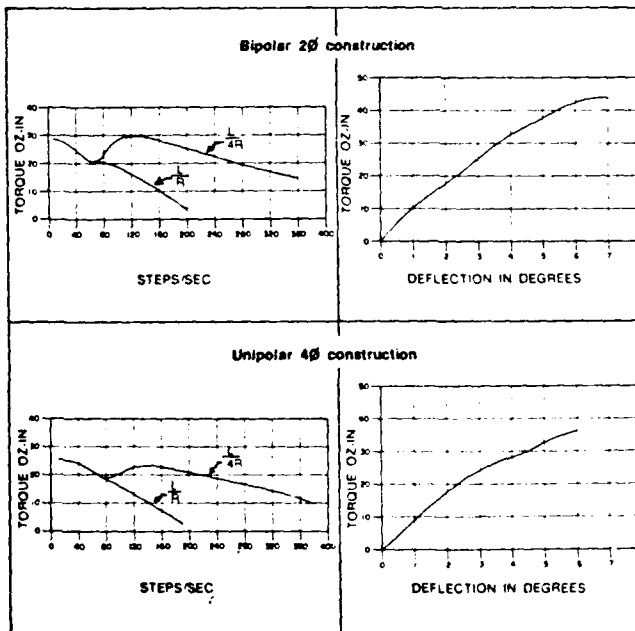
This is an extremely reliable and efficient motor. Improved heat dissipation results in lower operating temperatures, longer life and better utilization of power.

Standard construction provides for 2-phase or 4-phase operation at a 7.5° or 15° step angle and sleeve or roller bearings.

Applications include chart drives, X-Y plotters and paper feed drives. Also medical instrumentation pump and valve drives.

Pull-out Torque vs. Stepping Rate

Applied Torque vs. Deflection



NOTE: Charts above illustrate torque characteristics when driven by a L/R and a L/4R drive. The improved performance of the L/4R drive is a direct result of lowering the effective time constant by increasing R_s (see wiring hook-up on reverse page). Increasing both the resistance and power supply voltage while maintaining sufficient current results in the improved performance. All calculations above were obtained from a motor with a 7.30° step angle.

SPECIFICATIONS

	2 β (4 leads)	4 β (8 leads)
Operating voltage	5V ± 10%	
Holding torque (oz-in)	40	30
Step Angle	7.5°	15°
No. Steps per rev	48	
7.30° step angle		
No. Steps per rev	24	
15° step angle		
Step angle tolerance	± 3%	
Non cumulative - 7.30° step angle		
Step angle tolerance	± 3%	
Non cumulative - 15° step angle		
Direction of Rotation	Either	
Moment of Inertia of rotor (g-cm ²)	15	
Bearing	Roller or Sleeve	
Weight (ozs)	45	
Ambient Temp Range Operating	-20°C to +70°C	
Ambient Temp Range Storage	-40°C to +85°C	
Max. Permissible motor temp	105°C	
Dielectric Test (for 2-6 sec)	1000V - 5 V RMS 60 Hz	
Power Consumption - Total	12W	
Insulating Resistance - 500 Vdc	100 M Ω	

Figure 54. Stepper Motor Description

Stepper Motors Series 82900

82900 SERIES ORDERING INFORMATION

OPERATING COIL CHARACTERISTICS PART NUMBER IDENTIFICATION

Catalog Part Number	Coil Resistance & Inductance/Phase	Max. DC Voltage/12 Watts Power		Motor Design
		1 ϕ Drive	2 ϕ Drive	
K82952	23 Ω 110mH	18	13	2 ϕ Construction (4 leads)
K82942	13 Ω 68mH	14	10	
K82932	6 Ω 31mH	9	6.5	
K82912	1.8 Ω 7.6mH	5	3.7	
K82964	45 Ω 115mH	25	18	4 ϕ Construction (8 leads)
K82954	27 Ω 72mH	20	14	
K82944	12 Ω 33mH	13	9	
K82924	3.6 Ω 7.7mH	7	5	

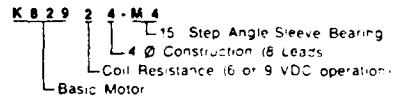
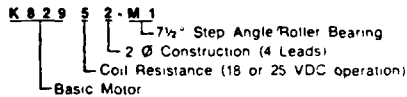
STEP ANGLE AND BEARING SPECIFICATION SUFFIX IDENTIFICATION

Suffix	Step Angle	Bearing
M1	7 1/2	Roller
M2	15	Roller
M3	7 1/2	Sleeve
M4	15	Sleeve

HOW TO ORDER

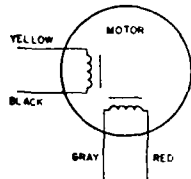
From the tables shown select:
 1 Part number for operating coil characteristics
 2 Suffix for step angle
 Examples of completed part numbers are shown below.

*Inductance ratings nominal — measurements made using a GR1650A impedance bridge

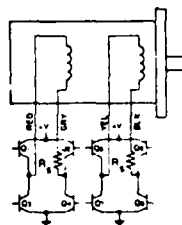
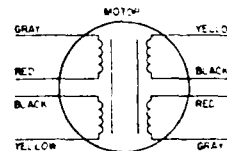


WIRING DIAGRAMS

Bipolar drive — 2 ϕ construction — 4 leads

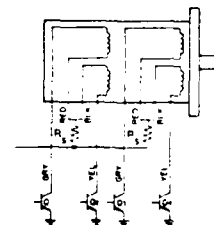


Unipolar drive — 4 ϕ construction — 8 leads



CM	Q-Q	Q-Q	Q-Q	Q-Q
ON	OFF	ON	OFF	
OFF	ON	OFF	ON	
OFF	ON	OFF	ON	
OFF	ON	ON	OFF	

See notes on page 2 for details.
 For CM, ON or OFF, see wiring diagram.
 For Q-Q, ON or OFF, see wiring diagram.
 For Q-Q, ON or OFF, see wiring diagram.



CM	Q-Q	Q-Q	Q-Q	Q-Q
ON	OFF	ON	OFF	
ON	OFF	OFF	ON	
OFF	ON	OFF	ON	
OFF	ON	ON	OFF	

See notes on page 2 for details.
 For CM, ON or OFF, see wiring diagram.
 For Q-Q, ON or OFF, see wiring diagram.
 For Q-Q, ON or OFF, see wiring diagram.

A W HAYDON CO PRODUCTS

NORTH AMERICAN PHILIPS CONTROLS CORPORATION

Cheshire, Conn. 06410 • (203) 272-0301

THIS INFORMATION SUBJECT TO CHANGE WITHOUT NOTICE • COPYRIGHT: 1976 • PRINTED IN U.S.A. • FORM 1 MAY

Figure 55. Stepper Motor Description

Drive Phases	Voltage	Output Current
4	12 V dc	Up to 350 mA per phase

Stepper Motor IC Driver Series SAA1027

OUTLINE AND MOUNTING DIMENSIONS: MM/inches

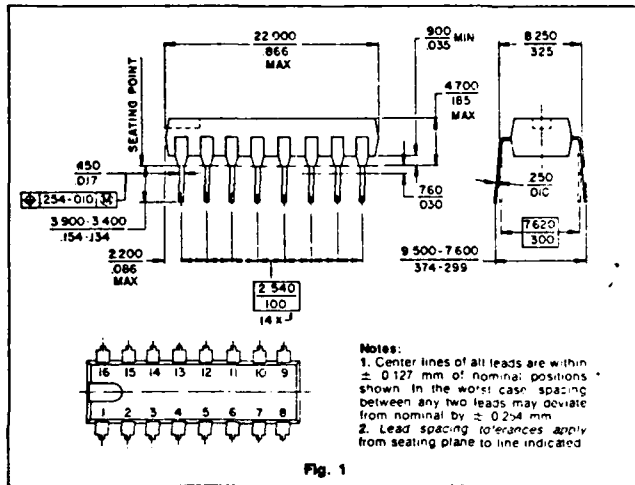
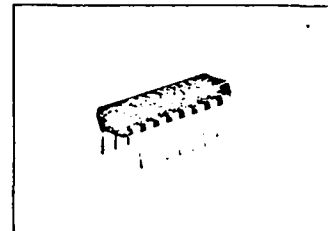


Fig. 1



The SAA1027 integrated circuit driver is designed to drive 4-phase stepper motors without the need for discrete power stages. The chip will drive stepper motors using less than 350 mA max per phase. 4-phase drive, 2 phases on. Both the IC and the motors can operate from a single 12 V dc power supply.

The circuit is contained in a single compact 16-pin dual-in-line plastic package. It comprises three input stages, a logic section and an output stage for each of the four stator windings of the motor.

The high noise immunity design of the IC makes the system particularly suitable for use in electrically noisy environments.

The simplicity and the reliability of the system is of great benefit in reducing both space and cost as well as the complexity of stepper systems. It thus opens up many new areas of application for digital motor control systems.

PINNING

Pin	Pin
1 not connected	9 output Q ₃
2 set input S	10 not connected
3 direction input R	11 output Q ₄
4 bias supply V _B	12 Ground
5 Ground	13 internal diodes
6 output Q ₁	14 control circuit supply V _p
7 not connected	15 trigger input T
8 output Q ₂	16 not connected

BLOCK DIAGRAM — SAA1027

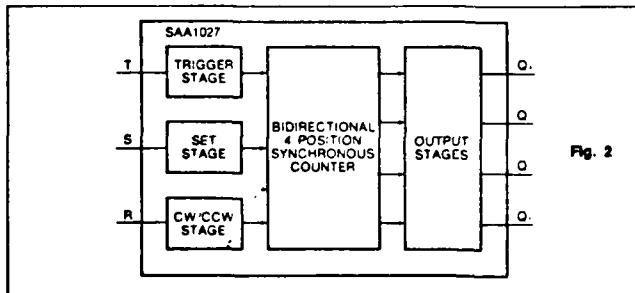


Fig. 2

SPECIFICATIONS

Operating voltage	12 V dc typ ca
Load Current (per phase)	350 mA max
High logic input level	7.5 V dc to 12 V dc typ ca
Low logic input level	0 V dc to 4.5 V dc max

Figure 56. Stepper Motor Driver Description

Stepper Motor IC Driver Series SAA1027

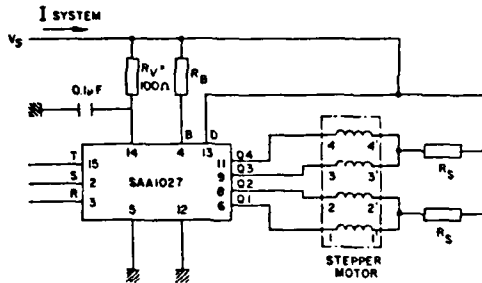


Fig. 3 Drive System Diagram

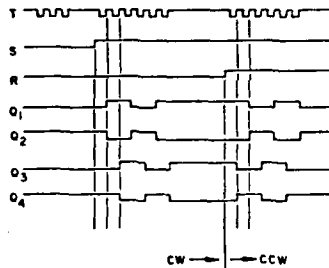


Fig. 4 Timing Diagram

BIAS RESISTOR (R_B) Fig. 3

Selection of resistor R_B (See Fig. 5 pg. 3)

Motor Series	R_B Value Ω	* R_B Value Ω	I System (mA)-Nominal
K82102-P2	470 ½W	0	300
K82201-P1	330 ½W	35 2W	400
K82201-P2	470 ½W	0	200
K82401-P1	150 1W	22 3W	700
K82401-P2	470 ½W	0	300
K82601-P2	180 1W	0	550
K82701-P2	150 1W	0	750
K82801-P2	180 1W	0	550

* R_B used to operate motors rated at 5 Volts

TRIGGER INPUT T

The repetition rate and the number of pulses applied to pin 15 of the IC determine the stepping rate and the ultimate angular position of the motor drive shaft. The steps are initiated by the positive-going edges of the pulses in the table below.

OUTPUT SWITCHING SEQUENCE

S = H (HIGH LEVEL)									
R = L (LOW LEVEL)					R = H (HIGH LEVEL)				
T	Q ₁	Q ₂	Q ₃	Q ₄	T	Q ₁	Q ₂	Q ₃	Q ₄
0	L	H	L	H	0	L	H	L	H
1	H	L	L	H	1	L	H	H	L
2	H	L	H	L	2	H	L	H	L
3	L	H	H	L	3	H	L	L	H
0	L	H	L	H	0	L	H	L	H

SET INPUT S

The output switching sequence can be set to a predetermined logic state ($Q_1=L, Q_2=H, Q_3=L, Q_4=H$) by applying a LOW voltage level to pin 2. This input is only effective if the voltage level at the trigger input is HIGH. To achieve maximum noise immunity, this input should be connected permanently to the HIGH voltage level if it is not required.

DIRECTION OF ROTATION INPUT R

The output switching sequence of the IC, and therefore the direction of rotation of the motor drive shaft, is determined by the level of the voltage applied to pin 3 of the IC. If the voltage level is HIGH, the drive shaft will rotate counterclockwise; if the level is LOW, the drive shaft will rotate clockwise. The level of the voltage applied to pin 3 can be changed at any time regardless of the logic state of the other two inputs. To achieve maximum noise immunity, this input must not be left floating if not used, but should be connected to the voltage level appropriate to the required direction of rotation (to pin 14 for counter-clockwise, to pin 5 for clockwise).

Stepper Motor IC Driver Series SAA1027

ELECTRICAL REQUIREMENTS OF THE DRIVE SYSTEM

Supply Characteristics

control circuit supply voltage	V_p	9.5—18 V (12 V typ.)
control circuit supply current	I_p	4.5 mA typ.
at $V_p = 12$ V	I_B	see Fig. 5
output circuit current		
output circuit bias voltage	V_B	see Fig. 6
at pin 4		
motor supply voltage	V_m	1.5—18 V (12 V typ.)
total motor current	I_m	700 mA max.
motor current in one stator	I_Q	350 mA max.
saturation voltage of output transistors at $I_Q = 350$ mA (pins 6, 8, 9 and 11)	V_{sat}	<1 V

Input Levels R, S and T

HIGH	V_{RH}	V_{SH}	V_{TH}	7.5 V to V_p
	I_{RH}	I_{SH}	I_{TH}	1 μ A typ.
LOW	V_{RL}	V_{SL}	V_{TL}	0—4.5 V max.
	I_{RL}	I_{SL}	I_{TL}	—30 μ A typ.

Temperatures:

Storage temperature —40°C to +125°C
 Operating ambient temperature —20°C to +70°C

NOTE: Q_1 , Q_2 , Q_3 , Q_4 breakdown voltages are 18 V dc.
 DO NOT EXCEED.

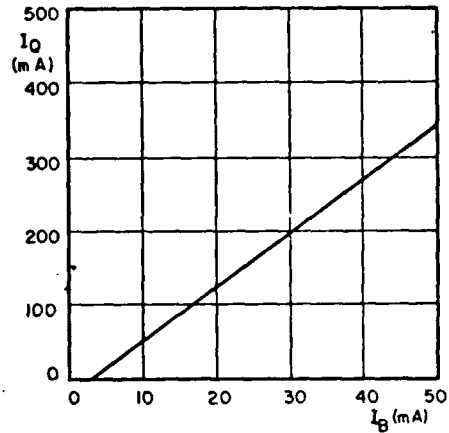


Fig. 5 Relationship between output current and bias current.

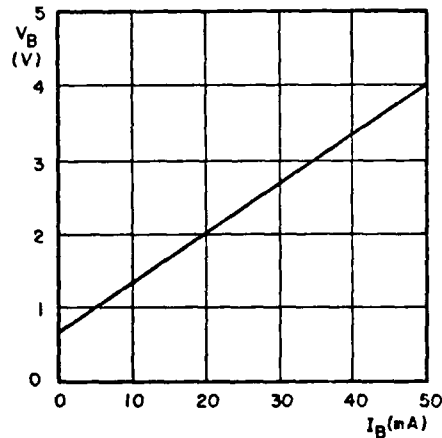


Fig. 6 Relationship between bias voltage at pin and bias current.

Stepper Motor IC Driver Series SAA1027

PRECAUTIONS TO MINIMIZE EFFECTS OF SWITCHING TRANSIENTS

If the IC and the motor are connected to the same supply source, a simple RC-network must be connected in the supply line to the logic part of the IC to prevent the switching sequence from being disturbed by transient spikes caused by switching of the motor windings. This network consists of a resistor of 100Ω and a capacitor of 0.1μF, as shown in Fig. 3. The capacitor must be located as close as possible to pins 14 and either 5 or 12 of the IC. The connection between the common line of the four integrated clamping diodes (pin 13) and the common line of the four motor windings must be as short as possible.

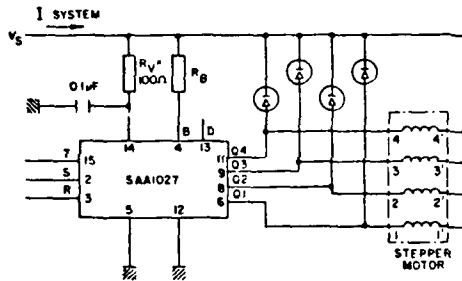


Fig. 7 System with alternate diode suppression

MINIMIZING THE DISSIPATION OF THE IC

The four integrated clamping diodes dissipate the energy which is stored in the motor windings when outputs Q are switched off. This dissipation (PD) is different for each of the motors and adds to the normal dissipation of the IC. If it is necessary to reduce (PD) to prevent overheating of the IC, the integrated clamping diodes must be disconnected, by removing the connection from pin 13, and four discrete clamping diodes must be connected to the motor windings as shown in Fig. 7.

USE OF IC DRIVER WITH STEPPER MOTORS

The SAA1027 integrated circuit is capable of driving a number of different 4-phase stepper motors without the need for discrete power stages.

Of particular interest in this regard are the NAPCC stepper motors listed below. The IC driver has been especially developed for use with these types of motors. Essential operating characteristics of each motor are summarized in the table below.

For more detailed information regarding specific motor types ask for the bulletin referenced in the last column or contact North American Philips Controls Corporation direct

STEPPER MOTORS RECOMMENDED FOR USE WITH IC DRIVER SAA1027

Series	Description	Step Angle	Voltage	Max. Pull-in Rate (Steps/sec)	Max. Working Torque (oz-in)	Bulletin Reference
K82102-P2		15°	12Vdc	700	.16	CM818
K82201-P1	Low-cost,	7°30'	5Vdc	540	.67	CM814
K82201-P2	light duty	7°30'	12Vdc	350	.78	CM814
K82401-P1		7°30'	5Vdc	400	2.7	CM814
K82401-P2		7°30'	12Vdc	200	2.5	CM814
K82601-P2	Low-cost,	15°	12Vdc	150	5.3	CM814
K82801-P2	medium duty	7°30'	12Vdc	180	8.2	CM814
K827C1-P2	Industrial type	7°30'	12Vdc	200	6.0	CM819

NORTH AMERICAN PHILIPS CONTROLS CORPORATION

Cheshire Conn 06410 • (203) 272-0301

THIS INFORMATION SUBJECT TO CHANGE WITHOUT NOTICE • COPYRIGHT 1977 • PRINTED IN U.S.A. • FORM CM822

Figure 59. Stepper Motor Driver Description (continued)

Appendix B: Probe Calibration

Probe Calibration

This appendix outlines the calibration procedure used in obtaining the sensor data. In AFIT calibrating anemometer sensors follows the steps detailed in reference 25 for use on a Thermo-Systems, Incorporated, Model 1125 calibrator (pictured in the rear of Figure 7).

According to reference 25, "the basic variable measured by a hot film or hot wire sensor is the rate of heat transfer from the wire to the fluid. Since this is not generally the variable of interest, a calibration must be made of bridge voltage vs. velocity or mass flow . . . Thermo-Systems manufactures a small (wind tunnel like) calibrating device that has a small nozzle fed by two quieting chambers in series."

Kirchner (ref. 14) interfaced this calibrator, together with auxiliary equipment such as voltmeters, manometers, and pressure transducers, to the ADAS. Calibration of the sensor used in this study followed Kirchner's procedure, wherein the isentropic, compressible flow equation determined velocity. The equation was:

$$U = \left((2gRT_0(k/(k-1)) (1 - (P_a/P_0)^{(k-1)/k}) \right)^{1/2}$$

in which U = velocity

g = gravitational constant

R = gas constant

T₀ = total temperature

k = specific heat ratio

P_a = atmospheric pressure

P₀ = total pressure

Varying the stilling chamber pressure (measured by a micromanometer) caused the velocity to change according to the above equation. Calibrating the anemometer consisted of recording the voltage at various velocities.

On measuring the voltage, reference 25 states, "the transducer used with the 1050 series anemometer is a small resistance element which is heated and controlled at an elevated temperature. The amount of electrical energy dissipated in the sensor is a measure of the cooling effect of the fluid flowing past the heated sensor . . . The cooling effect of the fluid passing over the sensor depends on both the mass flow and temperature difference between the sensor and the fluid. The relationship between bridge voltage and mass flow or mass flux is as follows:

$$\frac{E^2 R}{(R+R_3)^2} = (A + B(rV)^{1/n})(t_s - t_e)$$

where A, B = constants depending on fluid and type of sensor.

Variables include thermal conductivity, viscosity, and Prandtl number.

r = density

V = velocity

n = exponent (close to 2)

t_s = sensor operating temperature

t_e = fluid or environment temperature

R, R₃ = bridge resistances

Reference 12 states that this equation -- King's Law -- "illustrates the non-linearity of the anemometer output as well as the relationship with density, velocity, and temperature. Although the basic variable is mass flow, velocity is indicated

whenever density is constant." (See, for example, Figure 62.) Further, reference 25 says, "if a calibration curve is plotted for velocity vs. bridge voltage, a very non-linear relationship results (approximately a $\frac{1}{4}$ power relation). The calibration curve will have a shape like Figure 60. Sensitivity is greatest at very low flow rates." To this Bradshaw (4) adds that "hot wire anemometers can be used for mean velocity measurement down to the speed at which the heat lost by free convection is much larger than the heat lost by forced convection . . . corresponding to the dynamic pressure of an airstream of 3 feet/second."

Table I records anemometer voltage output and calibrated velocity values. Plotting anemometer voltage verses velocity as in Figure 60 results in a classic fourth order fit (ref. 3). But this form is not convenient when used in the computer, which during an experimental run, reads a voltage first and then converts to velocity. So Figure 61 presents a replotting of the data. This is the curve used to calculate all mean velocities and to evaluate the constant $1/a_1$ (the slope of this curve) in the fluctuating velocity computations. Figure 62 shows a "best fit" King's law plot (ref. 12) -- "best fit" determined through the regression analysis utility package in the ADAS.

CALIBRATION CURVE

Sensor #K480 (1 Oct 81)

The equation is:

$$E=A+BU+CU^2+DU^3+FU^4$$

where E=volts, U=velocity, and

$$A=3.946980015$$

$$B=.085626883$$

$$C=-.0023143882$$

$$D=.00004832403$$

$$F=-4.499467E-07$$

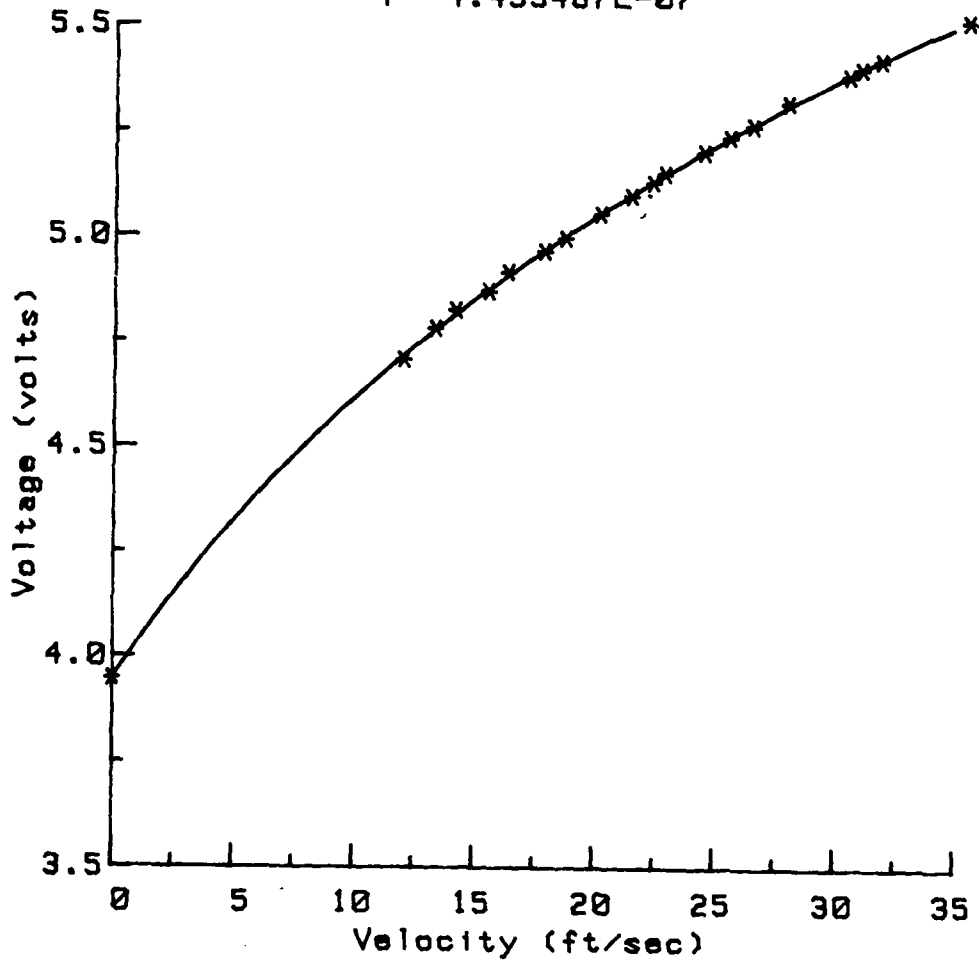


Figure 60. Fourth Order Calibration Curve

CALIBRATION CURVE

Sensor #K480 (1 Oct 81)

The equation is:

$$U = A + BE + CE^2 + DE^3$$

where U=velocity, E=volts, and

A=-155.55

B=105.1905

C=-26.402

D=2.466646

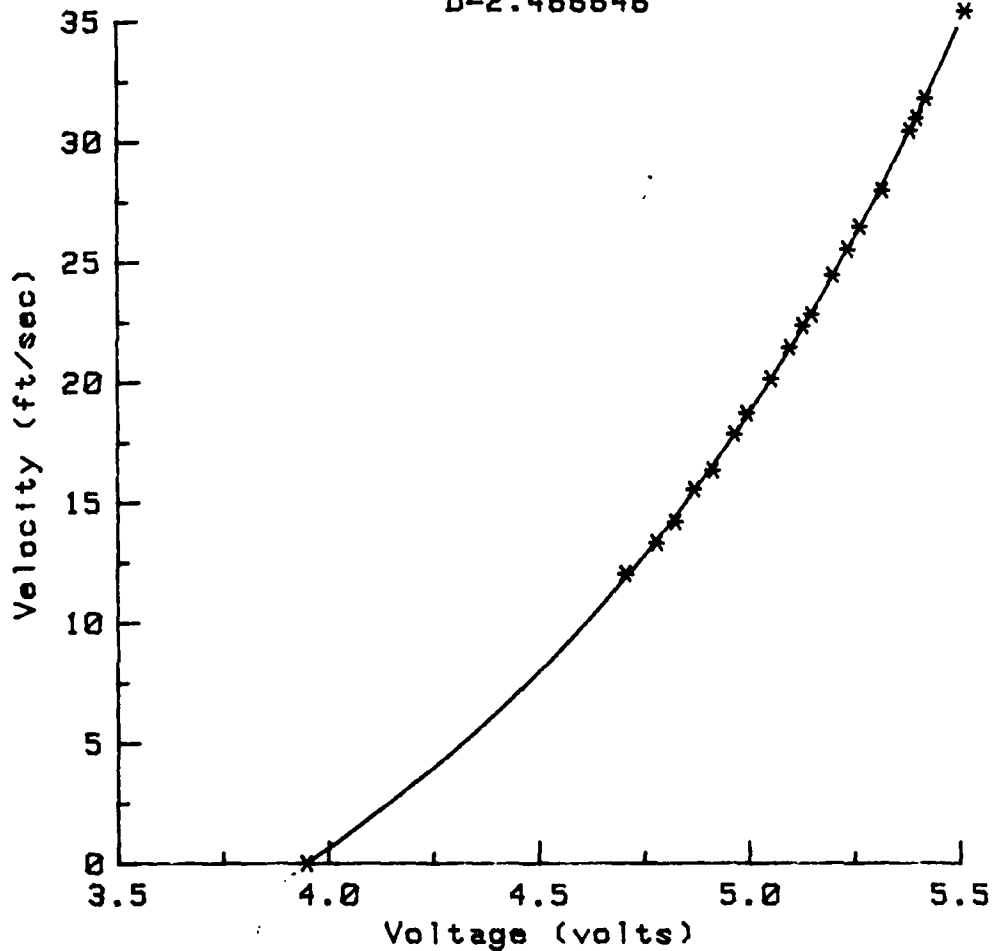


Figure 61. Third Order Calibration Curve

CALIBRATION CURVE (KING'S LAW)

Sensor #K480 (1 Oct 81)

The equation is:

$$E^2 = A + BU^n$$

where E=volts, U=velocity, and

$$A=15.5397464378$$

$$B=1.11209577372$$

$$n=.73$$

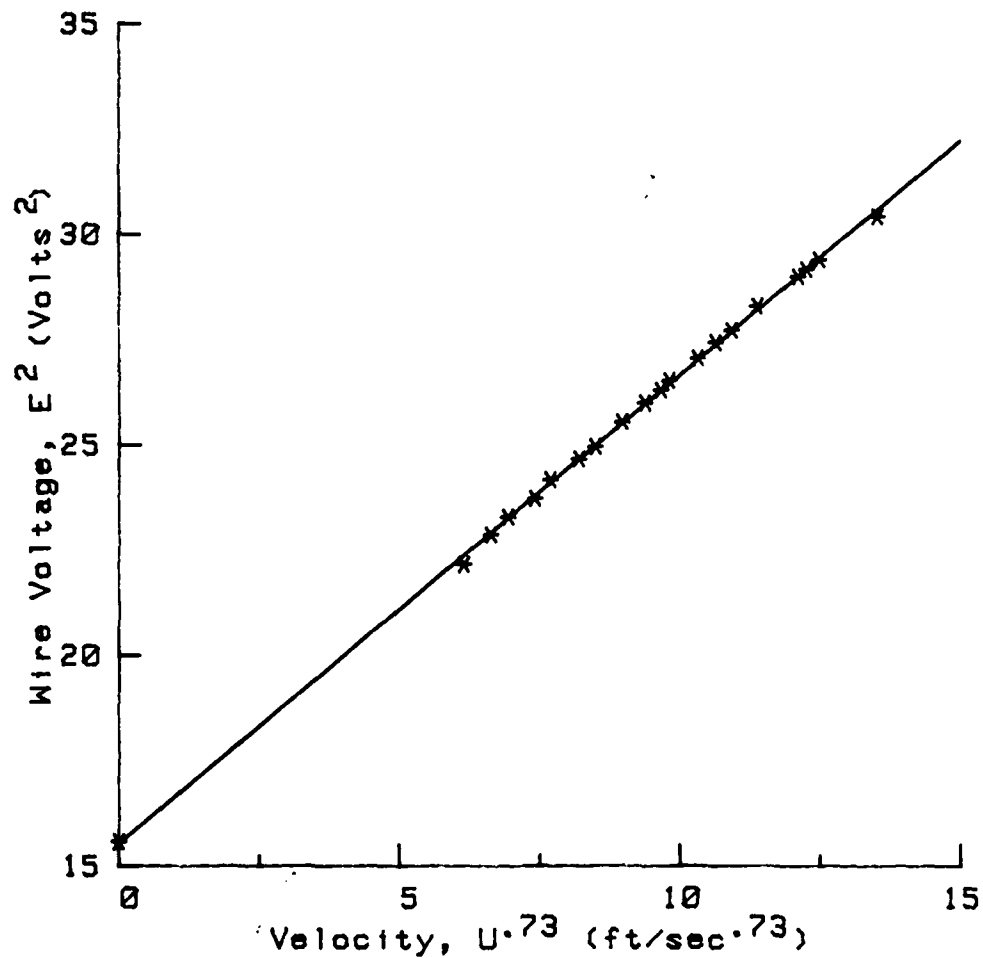


Figure 62. "Best Fit" King's Law Calibration Curve

Table I

HOT WIRE CALIBRATION DATA

Sensor #K480 (1 October 1981)

Voltage
(Volts)

Velocity
(Ft/Sec)

3.9472
4.707
4.7812
4.825
4.8705
4.9159
4.9661
4.9964
5.054
5.0987
5.129
5.1509
5.202
5.2379
5.266
5.32
5.386
5.4017
5.4224
5.5164

0
12.0325602886
13.3294450199
14.1942681938
15.5547424125
16.3476304044
17.8567733664
18.7288169332
20.1684964878
21.4579490361
22.3629950064
22.8313844372
24.4711001861
25.5302228262
26.4883536196
27.9869933901
30.4800399143
31.0004848555
31.8124568686
35.4615477899

Appendix C: Raw Data

VELOCITY PROFILE

No Grid

Sensor located 3.96 inches downstream from grid.

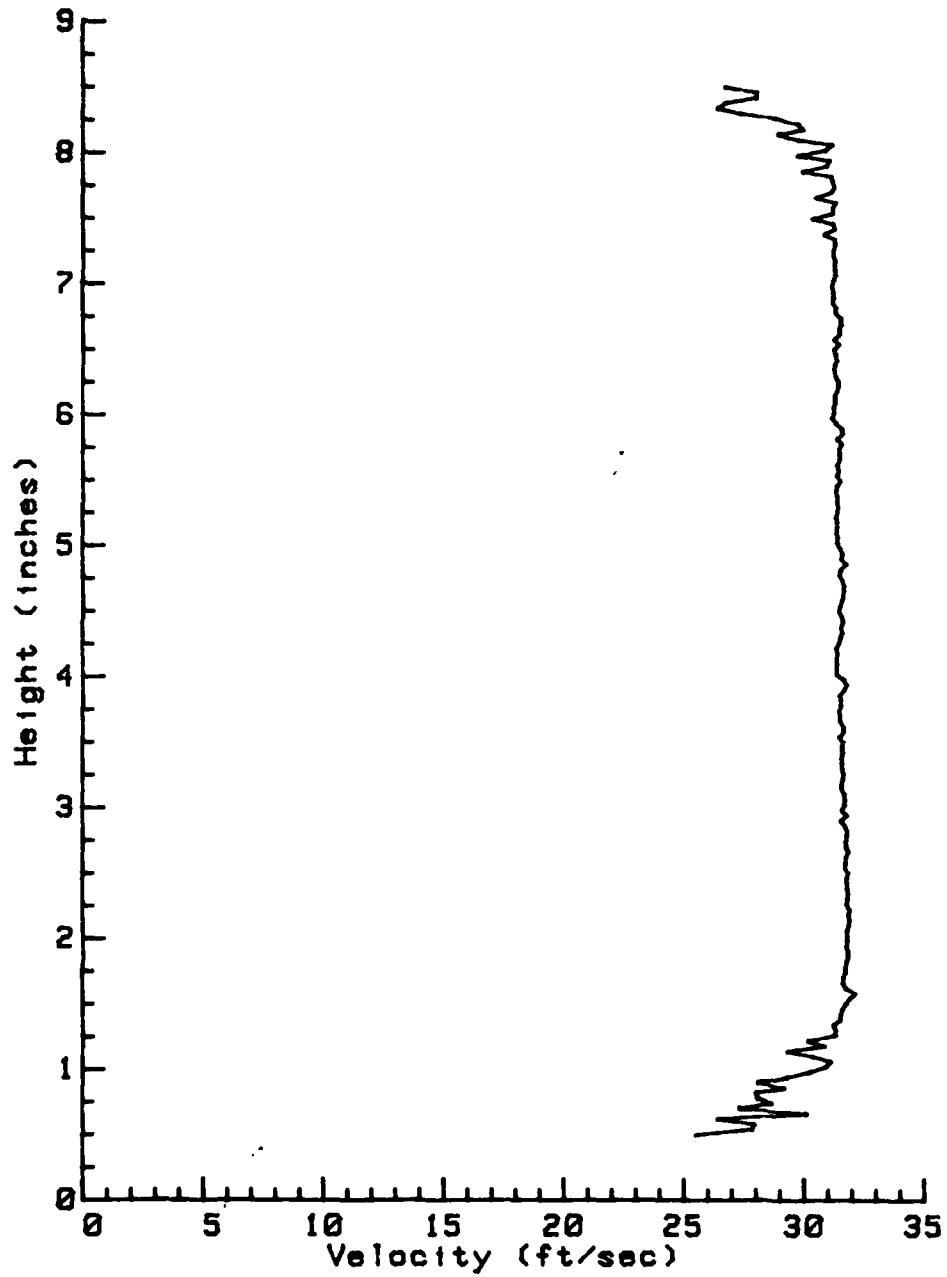


Figure 63. Velocity Profile, No Grid, X = 4 inches

VELOCITY PROFILE

No Grid

Sensor located 14.04 inches downstream from grid.

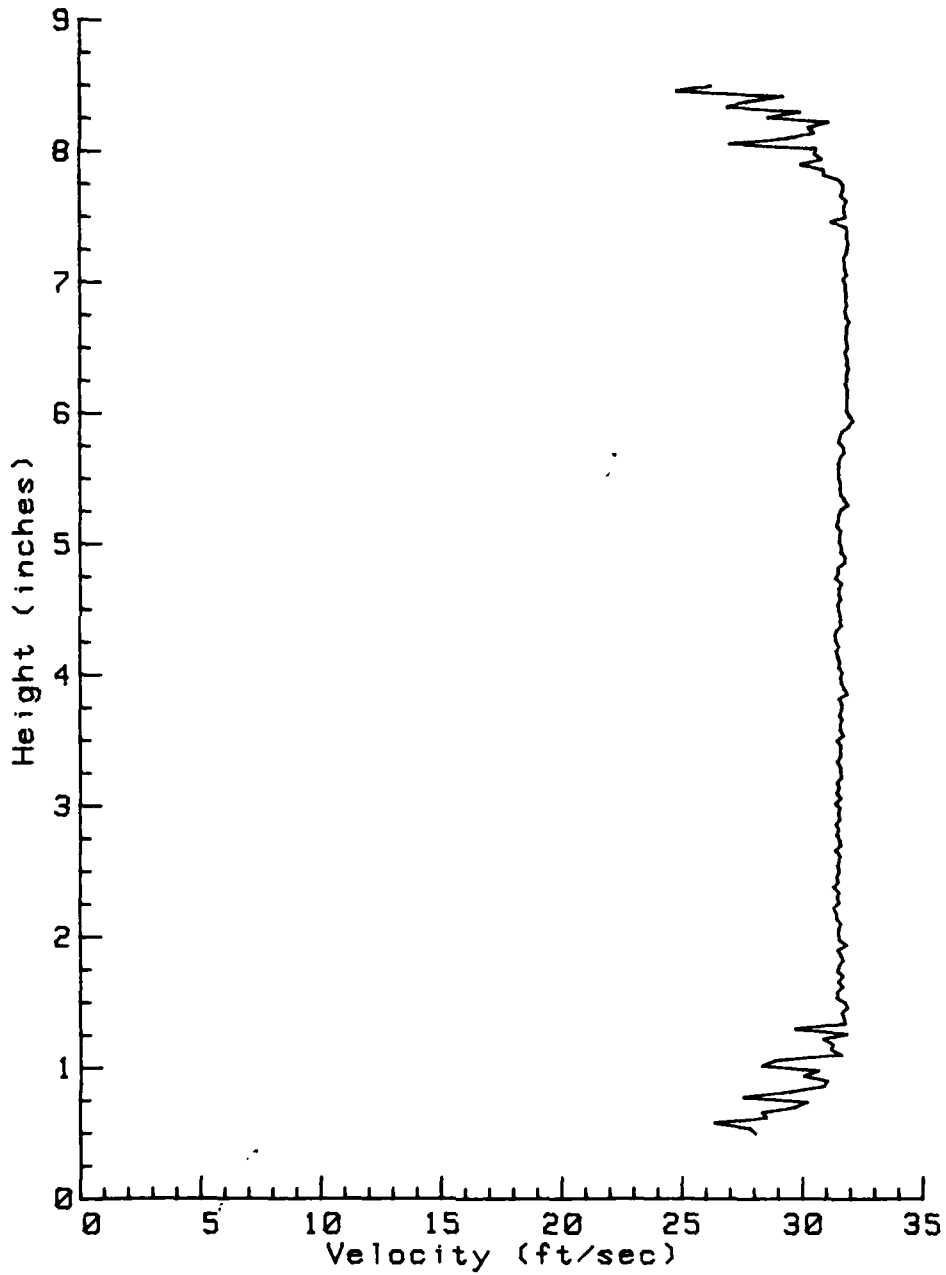


Figure 64. Velocity Profile, No Grid, X = 14 inches

VELOCITY PROFILE

No Grid

Sensor located 28.98 inches downstream from grid.

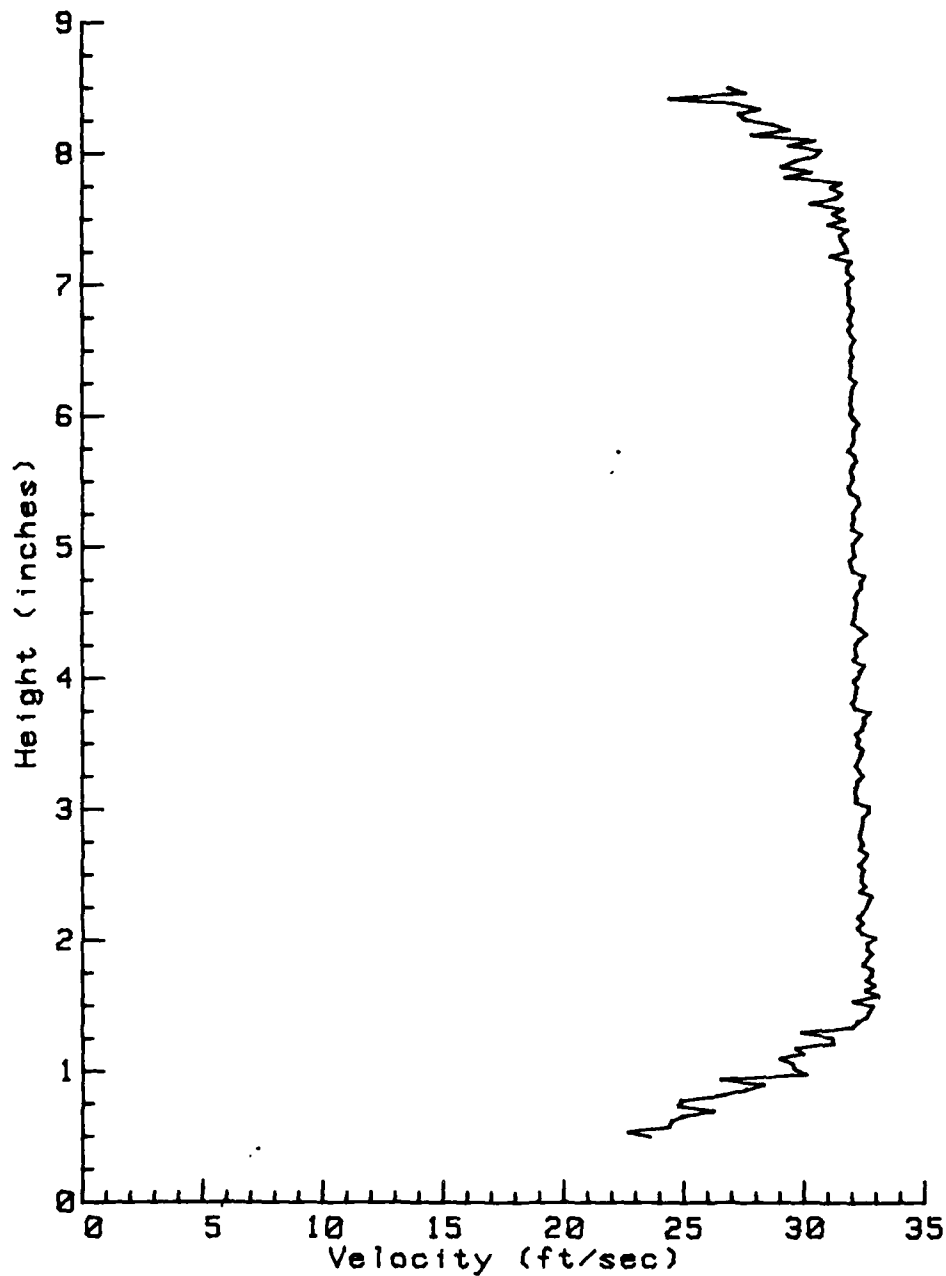


Figure 65. Velocity Profile, No Grid, X = 29 inches

VELOCITY PROFILE

Grid A3

Sensor located 3.96 inches downstream from grid.

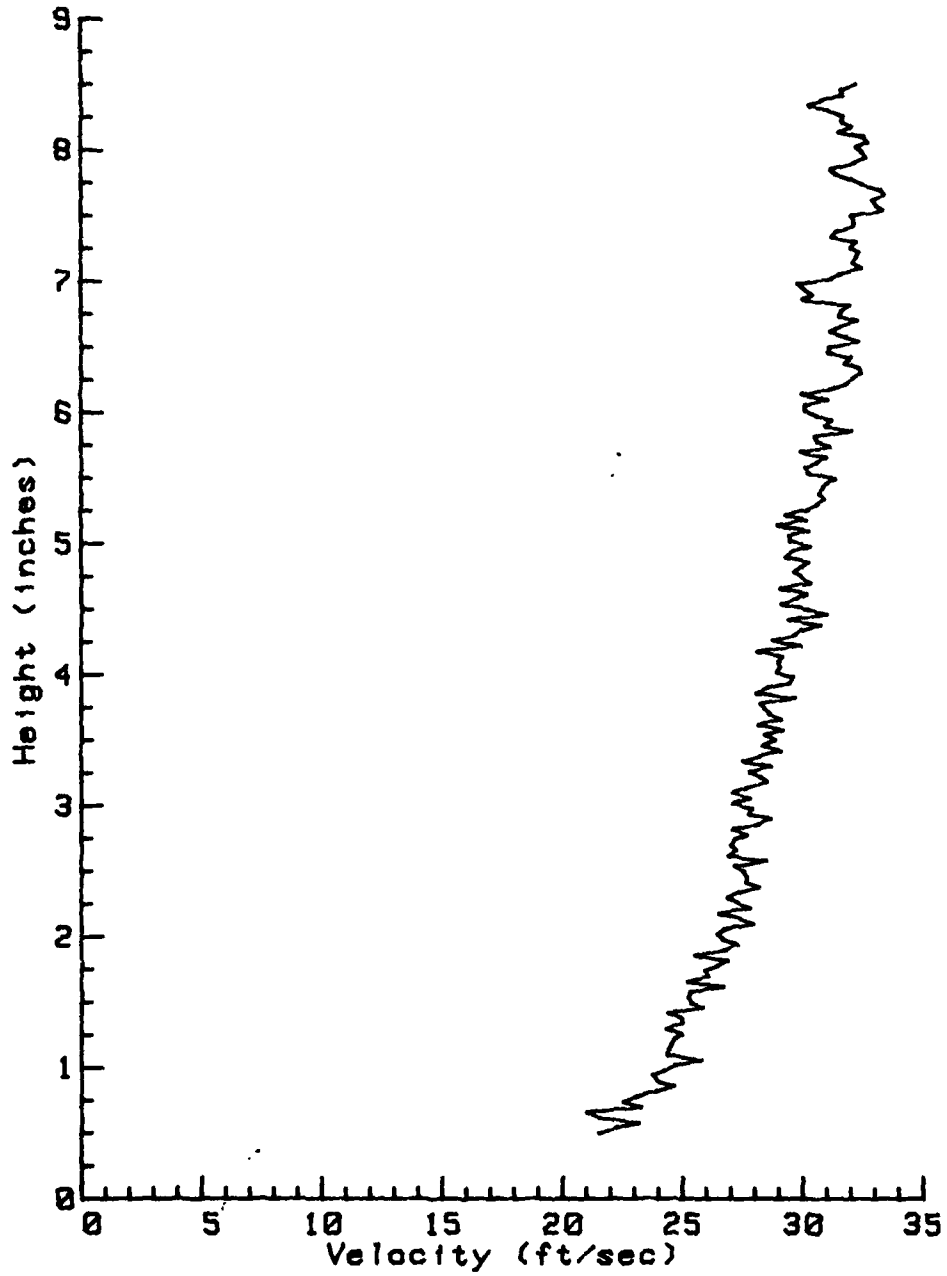


Figure 66. Velocity Profile, Grid A3, X = 4 inches

VELOCITY PROFILE

Grid R3

Sensor located 14.04 inches downstream from grid.

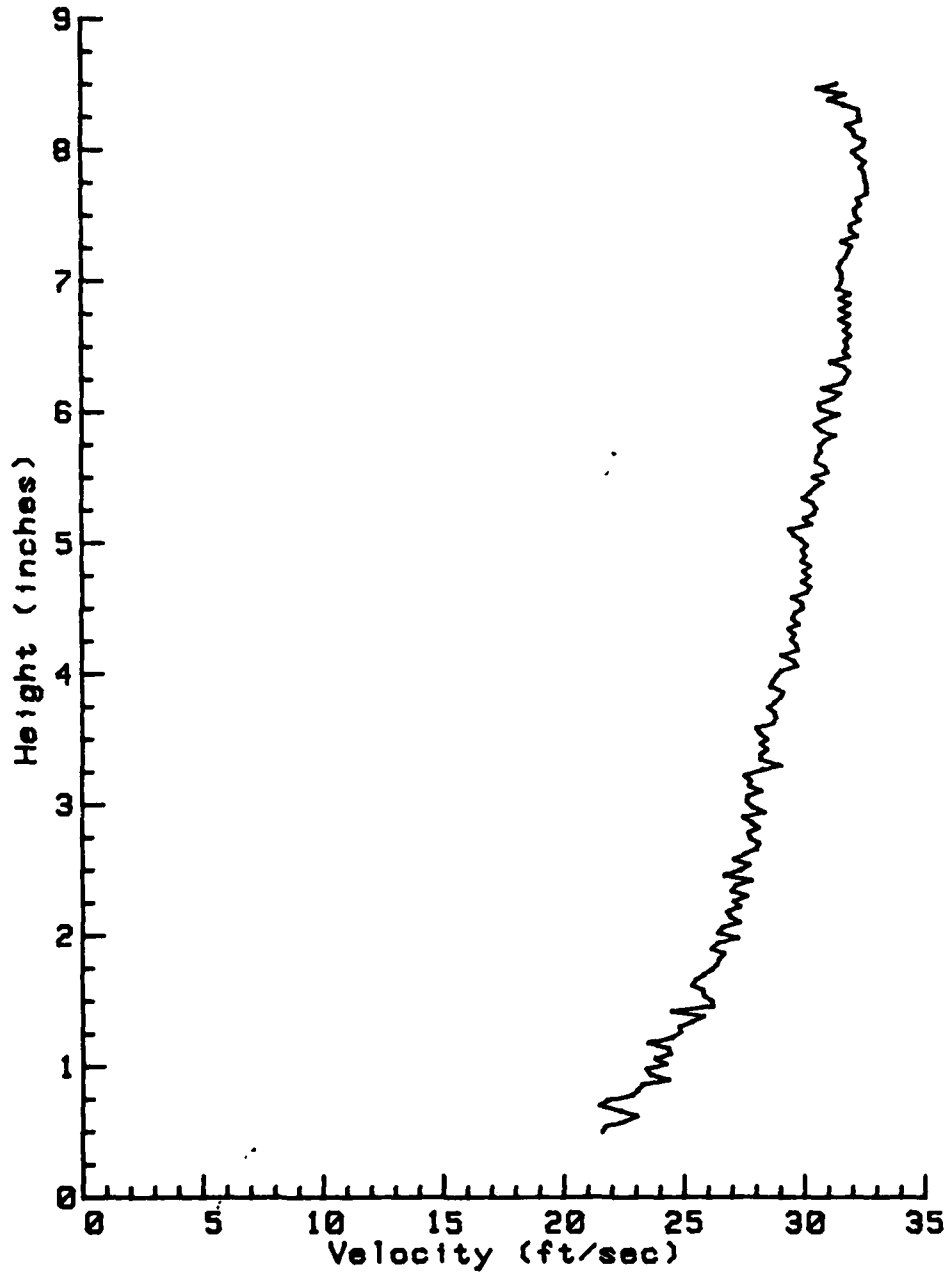


Figure 67. Velocity Profile, Grid A3, X = 14 inches

VELOCITY PROFILE

Grid A3

Sensor located 28.98 inches downstream from grid.

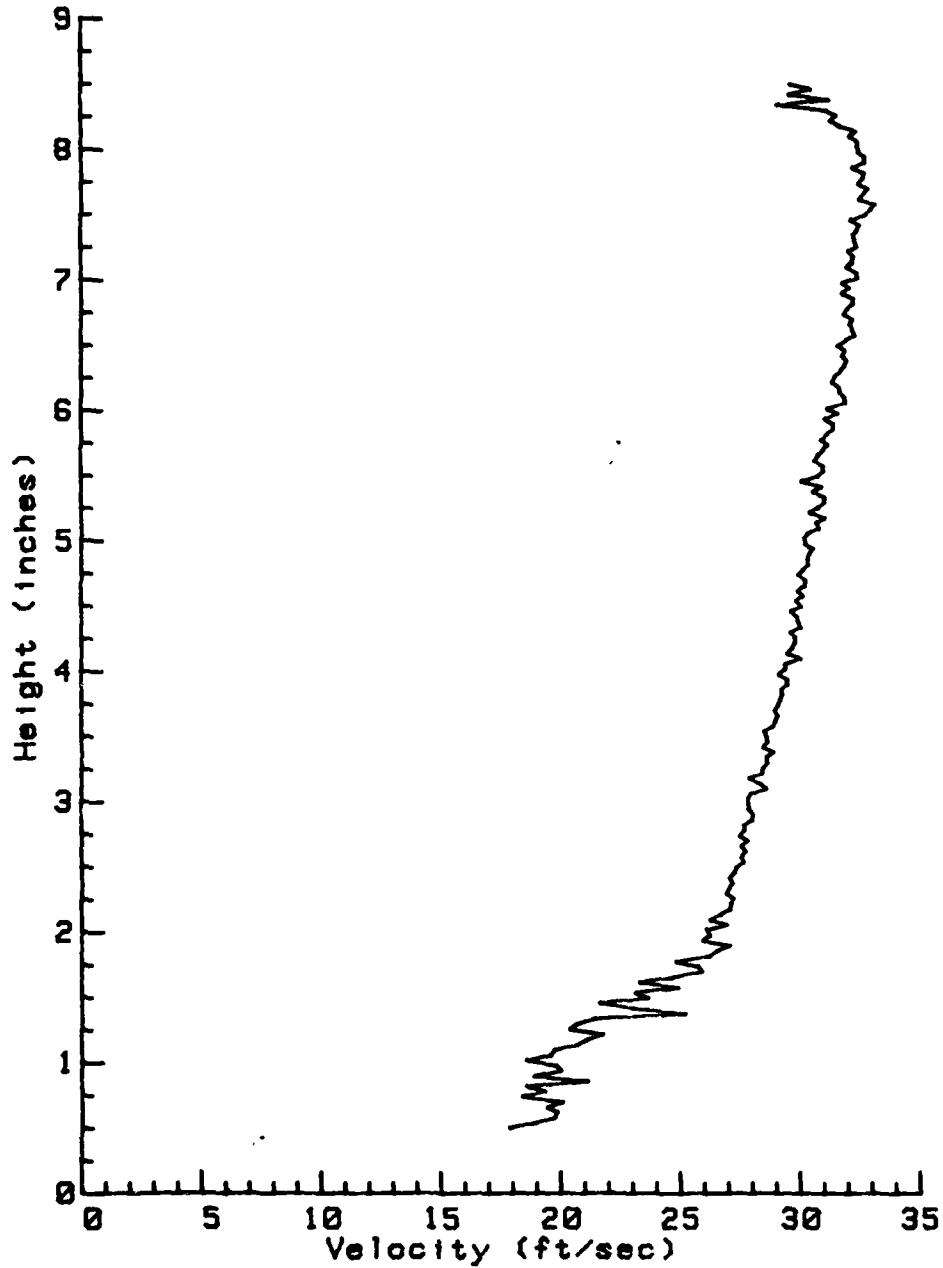


Figure 68. Velocity Profile, Grid A3, X = 29 inches

VELOCITY PROFILE

Grid B1

Sensor located 3.96 inches downstream from grid.

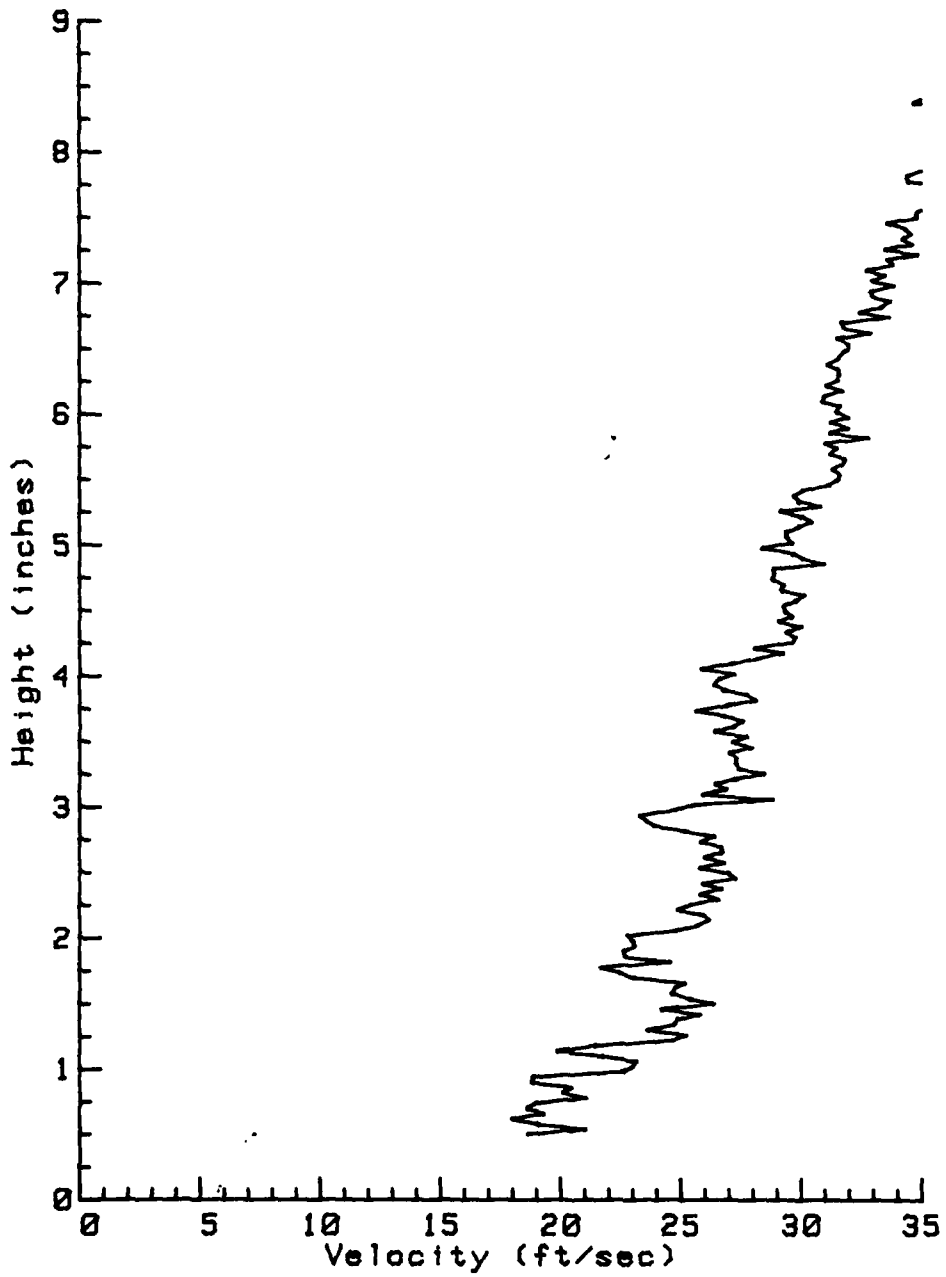


Figure 69. Velocity Profile, Grid B1. X = 4 inches

VELOCITY PROFILE

Grid B1

Sensor located 14.04 inches downstream from grid.

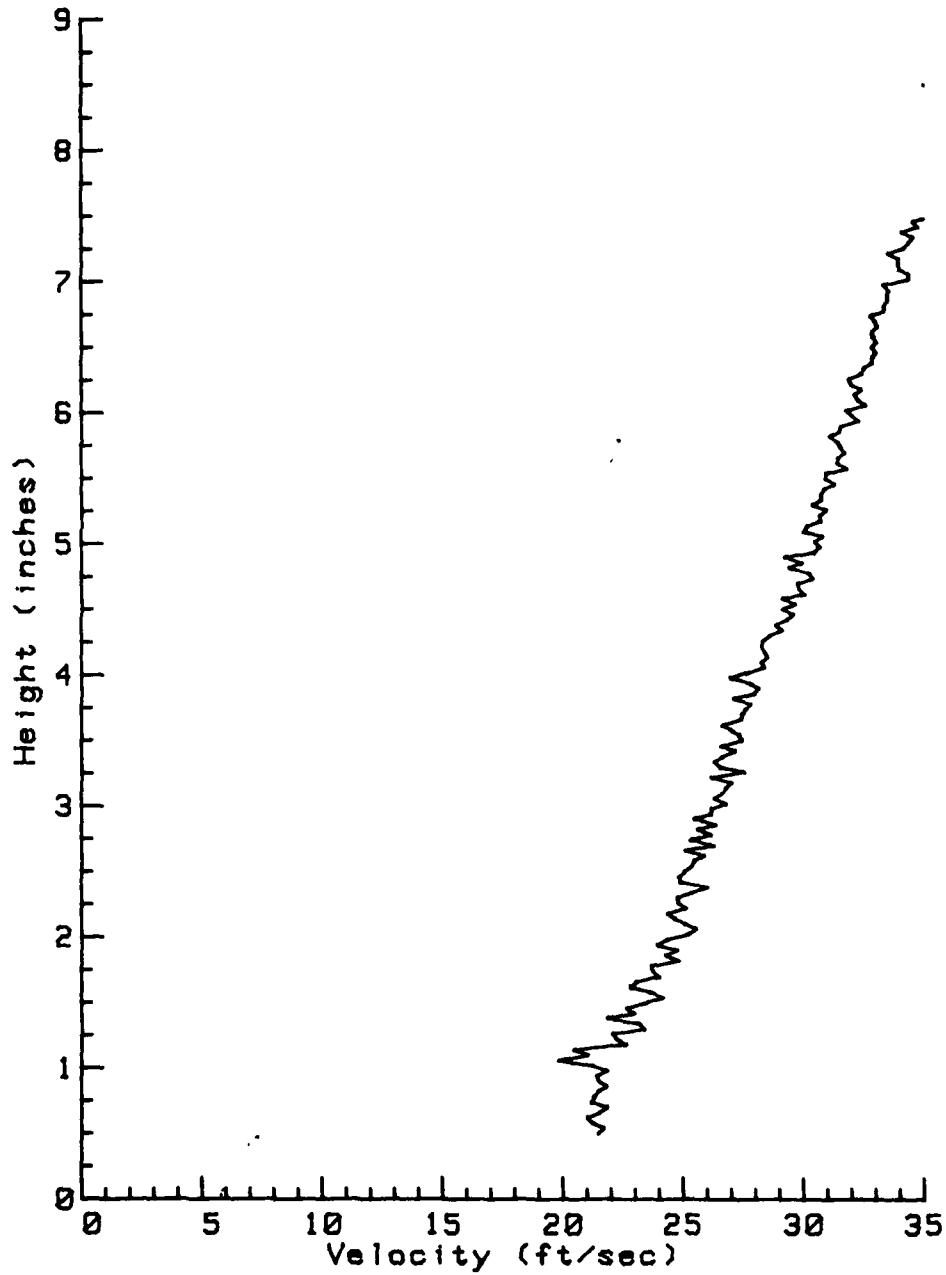


Figure 70. Velocity Profile, Grid B1, X = 14 inches

VELOCITY PROFILE

Grid B1

Sensor located 28.98 inches downstream from grid.

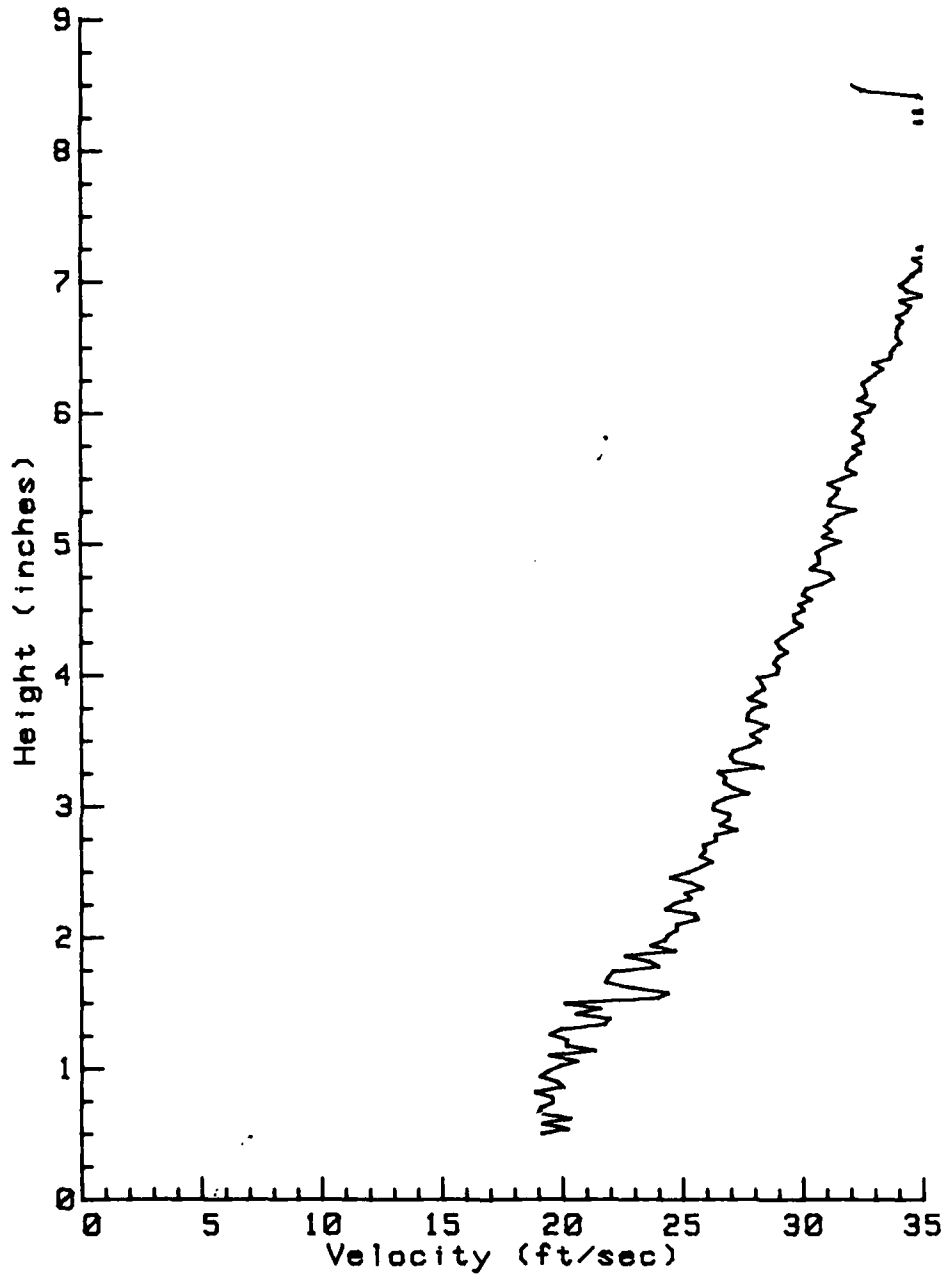


Figure 71. Velocity Profile, Grid B1, X = 29 inches

VELOCITY PROFILE

Cylinder

Sensor located 3.96 inches downstream from grid.

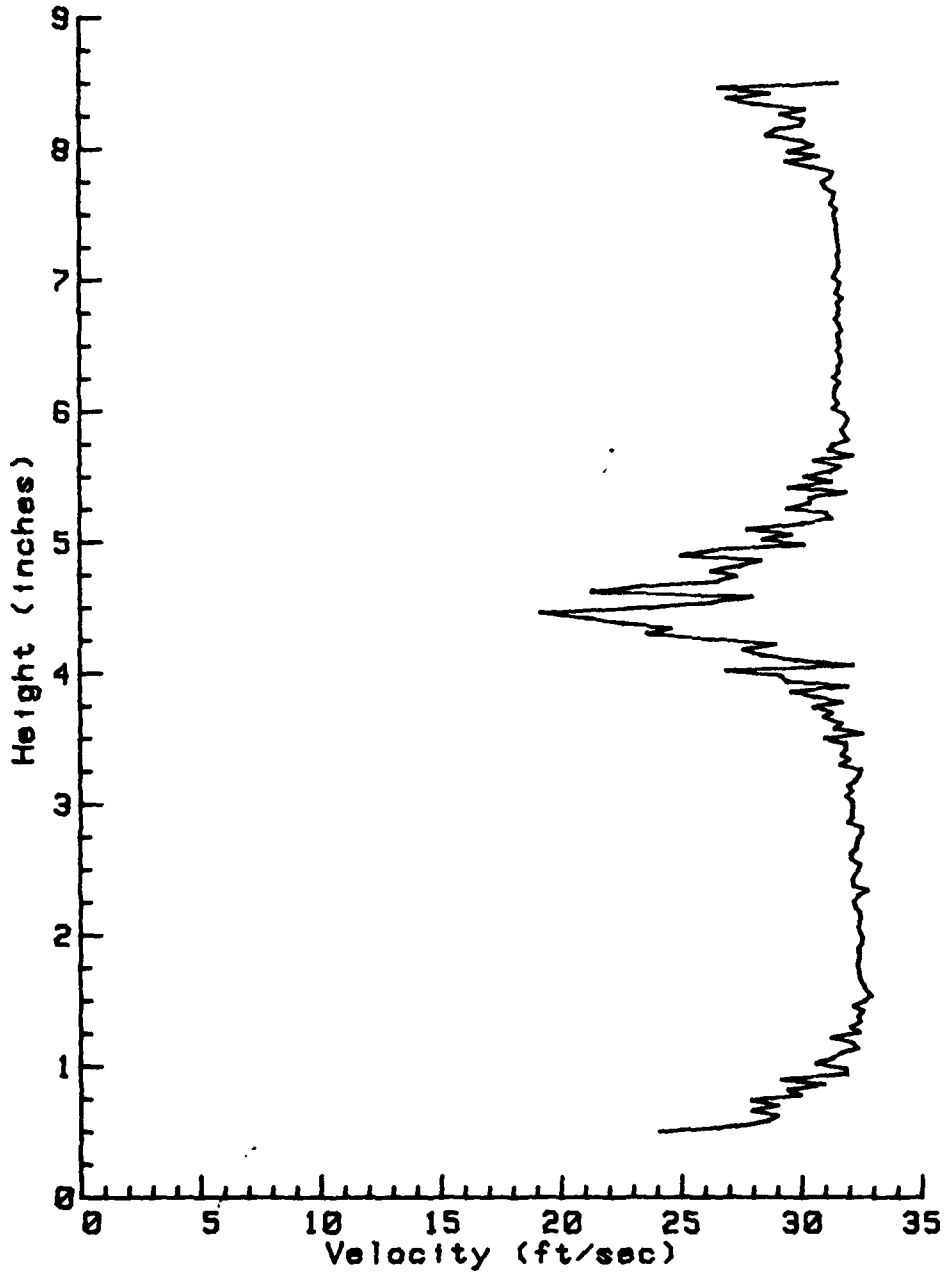


Figure 72. Velocity Profile, Cylinder, X = 4 inches

VELOCITY PROFILE

Cylinder

Sensor located 14.04 inches downstream from grid.

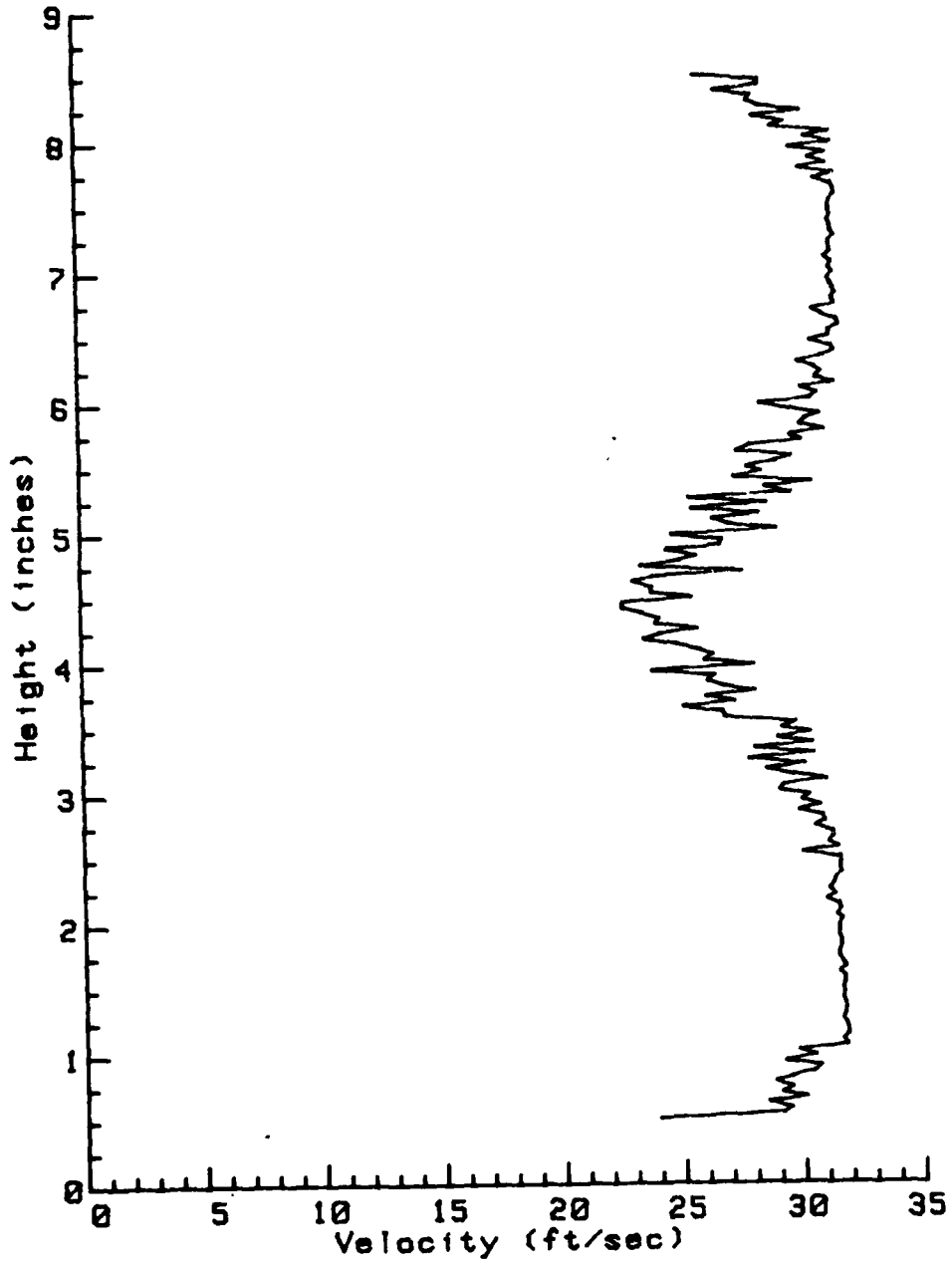


Figure 73. Velocity Profile, Cylinder, X = 14 inches

VELOCITY PROFILE

Cylinder

Sensor located 28.98 inches downstream from grid.

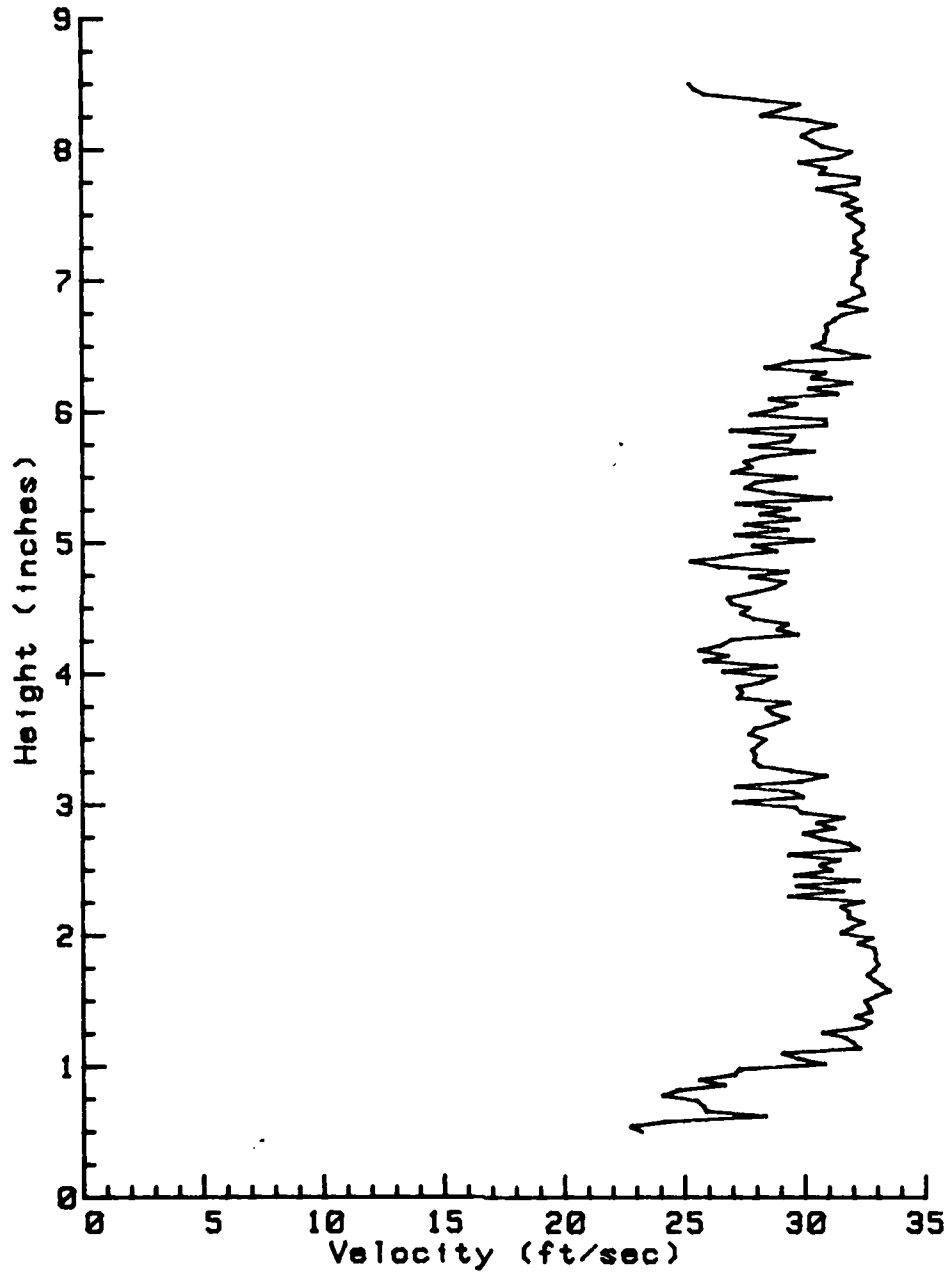


Figure 74. Velocity Profile, Cylinder, X = 29 inches

Table II

MAXIMUM RUN VELOCITIES

<u>Grid</u>	<u>Location</u>	<u>U_{max}</u> (ft/sec)	<u>Traverse</u>
No Grid	.44	32.1	down
	1.56	32.2	up
	3.22	33.1	down
A1	.44	34.1	up
	1.56	33.1	up
	3.22	33.8	down
A3	.44	33.4	up
	1.56	32.7	down
	3.22	33.1	up
B1	.44	37.6	up
	1.56	36.8	down
	3.22	36.8	up
Cylinder	.44	32.9	down
	1.56	31.8	up
	3.22	33.5	down

During these runs, the barometer varied from 29.10 in Hg to 29.22 in Hg; the temperature varied from 73.5° to 79.5°F.

Vita

Samuel A. Robinson Jr. of Holmdel, New Jersey, graduated from Red Bank High School, Red Bank, New Jersey (1970); from Stevens Institute of Technology, Hoboken, New Jersey, with a Bachelor of Engineering degree (1974); and from the University of Missouri, Columbia, Missouri, with a Master of Business Administration degree (1978). Prior to entering the service, he was a research assistant to Professor James H. Potter of Stevens Institute and was responsible for much of the graphics in Professor Potter's book Steam Charts. From 1975 to 1978, Captain Robinson served as a missile combat crew commander at Whiteman Air Force Base, Missouri. Subsequently, he served as a tactical C³I (Command, Control, Communications, and Intelligence) systems engineer at Hanscom Air Force Base, Massachusetts. Assigned to the Air Force Institute of Technology in June, 1980, Captain Robinson's new assignment in January 1982, is to Air Force Systems Command's Space Division in Los Angeles, California.

Permanent Address: 17 Knollwood Road
Holmdel, New Jersey 07733

UNCLASSIFIED

SECURITY CLASSIFICATION OF THIS PAGE (When Data Entered)

REPORT DOCUMENTATION PAGE		READ INSTRUCTIONS BEFORE COMPLETING FORM
1. REPORT NUMBER AFIT/GAE/AA/81D-25	2. GOVT ACCESSION NO.	3. RECIPIENT'S CATALOG NUMBER
4. TITLE (and Subtitle) A COMPUTERIZED DATA ACQUISITION INTERFACE TO MEASURE TURBULENT SHEAR FLOW VELOCITY PROFILES BEHIND A GRID OF PARALLEL RODS		5. TYPE OF REPORT & PERIOD COVERED MS Thesis
		6. PERFORMING ORG. REPORT NUMBER
7. AUTHOR(s) Samuel A. Robinson Jr. Capt USAF		8. CONTRACT OR GRANT NUMBER(s)
9. PERFORMING ORGANIZATION NAME AND ADDRESS Air Force Institute of Technology (AFIT-EN) Wright-Patterson AFB, Ohio 45433		10. PROGRAM ELEMENT, PROJECT, TASK AREA & WORK UNIT NUMBERS
11. CONTROLLING OFFICE NAME AND ADDRESS		12. REPORT DATE December, 1981
		13. NUMBER OF PAGES 124
14. MONITORING AGENCY NAME & ADDRESS (if different from Controlling Office)		15. SECURITY CLASS. (of this report) Unclassified
		15a. DECLASSIFICATION DOWNGRADING SCHEDULE
16. DISTRIBUTION STATEMENT (of this Report) Approved for public release; distribution unlimited.		
17. DISTRIBUTION STATEMENT (of the abstract entered in Block 20, if different from Report)		
28 JAN 1982		
18. SUPPLEMENTARY NOTES Approved for public release; IAW 190-17 Frederic C. Lynch, Major, USAF Director of Public Affairs <i>Frederic C. Lynch</i>		
19. KEY WORDS (Continue on reverse side if necessary and identify by block number) Turbulence Shear Flow Generation Flow Behind Grids Hot Wire Anemometer Data Acquisition		Frederic C. LYNCH, Major, USAF Director of Public Affairs Wright-Patterson AFB, OH 45433
20. ABSTRACT (Continue on reverse side if necessary and identify by block number) A design study was conducted to develop a computerized, electro-mechanical data acquisition system interface to instrumentation/apparatus measuring turbulent shear flow velocity profiles behind a grid of parallel rods. Data on profiles generated behind two such grids was acquired via a digital controller and a user-built interface to the data acquisition system. Conclusions were drawn that the digital controller did provide a superior means in		

DD FORM 1 JAN 73 1473

EDITION OF 1 NOV 65 IS OBSOLETE

UNCLASSIFIED

SECURITY CLASSIFICATION OF THIS PAGE (When Data Entered)

UNCLASSIFIED

SECURITY CLASSIFICATION OF THIS PAGE(When Data Entered)

collecting/reducing data than existed before, that the interface did provide an enhanced capability in documenting fluid flow phenomena under such test conditions and that the experience did indicate future work in automating instrumentation/apparatus electromechanical components.

UNCLASSIFIED

SECURITY CLASSIFICATION OF THIS PAGE(When Data Entered)

FILMED
S-8